Volume 7, Number 2, Spring 2021

ACERP
Advanced Ceramics Progress

ISSN 2423-7477
e-ISSN 2423-7485

Advanced Ceramics Progress

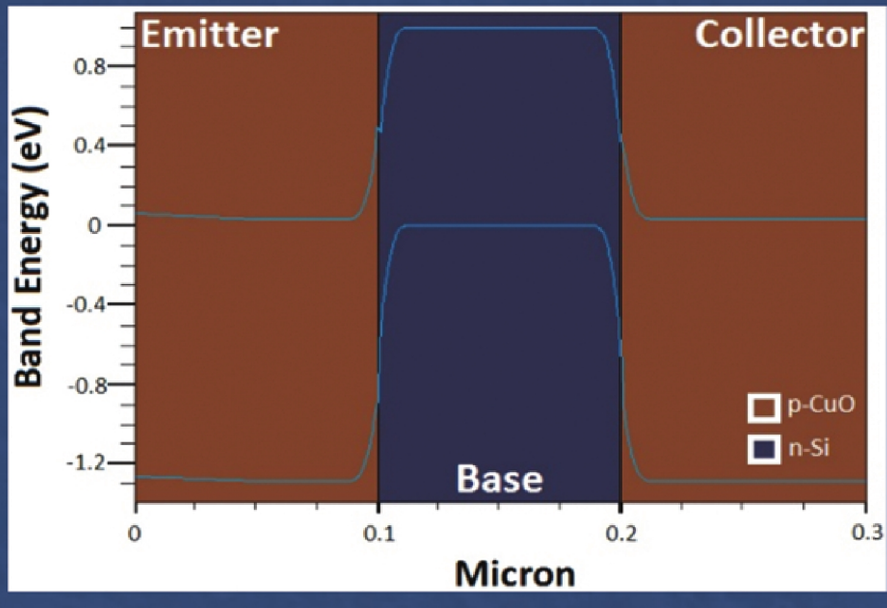

Materials and Energy
Research Center

Iranian Ceramic Society

In The name of God

Advanced Ceramics Progress

DISCLAIMER

The publication of articles in Advanced Ceramics Progress does not imply that the editorial board, editorial advisory board, reviewers or the publisher accept, approve or endorse the data and conclusions of authors.

Advanced **Cer**amics **P**rogress (ISSN 2423-7477) (e-ISSN 2423-7485)
Web Site: www.acerp.ir, E-mail: office@acerp.ir
Tel: +98 (0) 26 36280040-7 ext.: 382, Fax: +98 (0) 26 36201888
Tel:+98 (0)21 88771626-7 ext.: 8931, Fax: +98 (0)21 88773352
Materials and Energy Research Center (MERC); Iranian Ceramic Society (ICERS)

ISSN: 2423-7477; e-ISSN: 2423-7485

Advanced Ceramics Progress: Vol. 7, No. 2, (Spring 2021) 1-43

CONTENTS

Advanced Ceramics Progress: Vol. 7, No. 2, (Spring 2021) 1-9

Materials and Energy Research Center
MERC

Contents lists available at ACERP

Advanced Ceramics Progress

Journal Homepage: www.acerp.ir

Original Research Article

Pseudocapacitive Behavior of Nb_2O_5-TNTs Nanocomposite for Lithium-ion Micro-batteries

M. Mohammadifar [a], A. Massoudi [b,*], N. Naderi [c], M. J. Eshraghi [c]

[a] *MS, Department of Semiconductors, Materials and Energy Research Center (MERC), Meshkindasht, Alborz, Iran*
[b] *Assistant Professor, Department of Semiconductors, Materials and Energy Research Center (MERC), Meshkindasht, Alborz, Iran*
[c] *Associate Professor, Department of Semiconductors, Materials and Energy Research Center (MERC), Meshkindasht, Alborz, Iran*

ARTICLE INFO

Article History:

Received 4 June 2021
Received in revised form 20 June 2021
Accepted 20 June 2021

Keywords:

Niobium Pentoxide
Titanium Nanotube
Pseudocapacitance
Lithium-Ion Battery
Micro-Battery

ABSTRACT

The present study aims to introduce Niobium pentoxide-Titanium nanotube (Nb_2O_5-TNTs) composite as a novel anode material synthesized through hydrothermal method. In this respect, Nb_2O_5 nanoparticles and TNTs are separately synthesized through sonochemical and anodizing processes, respectively. According to FESEM images, the well-oriented TNTs with inner and outer diameters of 70 and 88 nm, respectively, are well decorated by Nb_2O_5 nanoparticles. The Nb_2O_5-TNTs anode shows the areal charge and discharge capacities of 0.167 mAh/cm^2 and 0.146 mAh/cm^2, respectively, at 0.113 mA/cm^2 as well as 60% capacitive storage in 20 mV/s. High power Nb_2O_5-TNT anode reveals 86% reversible capacity in the 16th cycle with a columbic efficiency of 84% for the 16th cycle. In addition, the charge transfer resistance in TNTs declines from 750 Ω to 680 Ω after decorating by Nb_2O_5. The superior performance of Nb_2O_5-TNT composites is taken into account to derive higher charge storage from a capacitive charge storage which is dominant in the diffusion-controlled process. Therefore, Nb_2O_5-TNT composite can be applied to the next-generation pseudocapacitive anode in lithium-ion batteries.

https://doi.org/10.30501/ACP.2021.289093.1064

1. INTRODUCTION

Ultrafast rechargeable lithium-ion batteries with a high charging rate, high energy density, and long life cycle are vastly used in portable electronics and microdevices. Both supercapacitor-like rate performance and battery-like capacity with a long lifetime are highly demanded in producing microsensors, smart medicine, small power sources, and so on [1-5]. One of the main advantages of lithium-ion micro-batteries is its thickness on a micrometer range and safety. They also enjoy several economic advantages such as their environmentally-friendly components, durable rechargeability, and their ability to be prepared in any shape or size of different substrates, to name a few [6,7].

Nonetheless, common lithium-ion batteries suffer from sluggish ion transfer which result in low kinetics. To provide a fast Li-ion reaction and diminish sluggish ion transfer, intercalation compounds with robust structure with open channels and the intercalation pseudocapacitance materials are the best candidates [8,9]. Till now, numerous researches have demonstrated that metal oxides with both stable structures and multicharge careers can be a good choice for lithium-ion insertion and extraction in and from the anode and cathode material. These materials with high-rate capabilities and rational designs lead to the enhancement

* Corresponding Author Email Address: massoudi@merc.ac.ir (A. Massoudi) URL: https://www.acerp.ir/article_132234.html

Please cite this article as: Mohamadifar, M., Massoudi, A., Naderi, N., Eshraghi, M. J., "Pseudocapacitive Behavior of Nb_2O_5-TNTs Nanocomposite for Lithium-ion Micro-batteries", ***Advanced Ceramics Progress***, Vol. 7, No. 2, (2021), 1-9. https://doi.org/10.30501/ACP.2021.289093.1064

of the diffusion of Li-ions into the electrode depth and improvement of the kinetics to achieve the maximum ion/electron transfer rate [10-15]. Indeed, the high-rate capability of lithium-ion batteries is limited due to random ion movement resulting from the low kinetics of redox reactions. Therefore, capacitive and pseudocapacitive materials can improve kinetics because the corresponding reduction and oxidation are surface-controlled [16,17].

As a new type of capacitance, pseudocapacitance is equal to derivation $d(\Delta q)/d(\Delta E)$ which is faradaic in nature. An important difference between pseudocapacitance and battery-like behavior is a change in the chemical reactant resulting from the faradaic charge transfer of the surface. There are three different types of capacitive charge storage mechanisms: adsorption, redox, and intercalation. Adsorption capacitance contains adsorption and desorption on metallic atom surfaces. Unlike adsorption pseudocapacitance, redox pseudocapacitance contains faradaic redox reactions on the electrode surface. While the charge is stored through surface coverage in adsorption, it is stored through chemical conversion between oxidation and reduction species on the surface in redox. This behavior is pseudocapacitive in nature because lithium ions are accommodated faradically in quasi two-dimensional planes in van der waals gap of the layer structure of the host material [18-21].

In this regard, one of the materials that can be applied in high-energy lithium-ion micro-batteries is Titania (TiO_2) which is a promised 3D intercalative material with the prior mechanical and chemical stability in the electrolyte window potential. Insertion and extraction of Li-ions in and from the TiO_2 structure mainly occur at 1.5 V versus Li/Li^+, while the $LiPF_6$ electrolyte compound reduces at 0.6-1 V versus Li/Li^+. Consequently, this phenomenon causes electrochemical stability of TiO_2 [22, 23]. Until now, many nanostructures of TiO_2 are used in lithium-ion batteries such as 3D microstructures, nanowires, nanotubes, nanorods, and nanoparticles. Among them, nanotube is the best structure due to the highest surface areas among other nanostructures [24,25]. In addition, the outer and inner walls of the tube make more active sites intercalate Li-ions into the TiO_2 lattice structure to form Li_xTiO_2 ($0<x<1$) [26]. Titania introduces the theoretical surface capacity of 125 mAh/cm^2. In 2009, F. Ortiz et al. prepared self-organized TiO_2 nanotubes with a maximum charge and discharge areal capacity of 77 $\mu Ah/cm^2$ with retention up to 90% over 50 cycles [27]. In 2011, Wei Wang et al. synthesized three-dimensional Ni/TiO_2 nanowire on the Ni foil with 0.016 mAh/cm^2 at 12 C with 20 cycles stability [28].

Furthermore, titanium niobium binary metal oxides, such as $TiNb_2O_7$ and $Ti_2Nb_{10}O_{29}$, seem to be interesting candidates for high-rate performances. Since T-Nb_2O_5 offers 2D transport pathways and little change in the lattice volume after lithium-ion intercalation, it guarantees original crystal structure maintenance [29-31]. Moreover, it enjoys the advantage of a pseudocapacitive charging mechanism. Recently, Lubke et al. illustrated that Nb dopant in TiO_2 nanofiber could improve the rate capability due to its high electrical conductivity and low lithium-ion diffusion paths resulting from a decrease in the crystallite size. The average capacities after 20 cycles in 5 C rate for doped and non-doped TiO_2 were 23 and 10 mAh/cm^2, respectively [32]. The present study considered decorating TNTs by T-Nb_2O_5 nanoparticles in order to prepare an innovative Nb_2O_5-TNT composite for the first time to construct a pseudocapacitive lithium-ion battery.

In this study, TNTs as an intercalative anode was synthesized through fluorinated electrolyte anodization**.** Moreover, Nb_2O_5 nanoparticles were synthesized through the surfactant-free sonochemical method and were decorated on TNTs through the hydrothermal method. The rate capability of samples was confirmed. Moreover, the pseudocapacitive behavior of the prepared electrode was investigated using the ratio of diffusion-controlled to surface-controlled contributions in cyclic voltammograms.

2. MATERIALS AND METHODS

2.1. Anodization of TiO_2 Nanotubes

First, Titanium sheets (99.7% purity) were mechanically polished and cleaned with ethanol (99%, Merck) and deionized water. For setting up, Titanium sheet was used as an anode and pure platinum (Pt) mesh as a cathode. Electrolyte solution was prepared using 1 wt% hydrofluoric acid (HF, 28%, Merck). Anodization was performed in a constant voltage condition of 20 V for 20 min. Finally, the samples were rinsed with deionized water and dried with N_2. To crystallize titanium nanotubes (TNTs), the samples were calcinated at 300 °C for 1 h.

2.2. Sonochemical Synthesis of Nb_2O_5 Nanoparticle

Synthesis of Nb_2O_5 nanoparticles using ultrasonic bath has been previously reported in the literature [33]. To be specific, commercial Nb_2O_5 powder was dissolved in HF and stirred at 100 °C for 1 h. The solution was diluted to the concentration of 2 g/L. After one hour of ultrasonication, the pH of the solution was adjusted to 9 using ammonia. Then, the final product was leached with EtOH and DI water and dried at 85 °C for 6 h to obtain amorphous Nb_2O_5. Finally, the white powder was calcined at 880 °C for 30 min at a heating rate of 10 °C/min.

2.3. Nb_2O_5-TNTs Composite Preparation

Nb_2O_5 nanoparticles were decorated on TNTs by hydrothermal treatment. The Nb_2O_5 decoration solution

served in a Teflon-lined stainless steel autoclave with different concentrations of Nb_2O_5 nanoparticles dispersed into the deionized water. The TNT sheet is supported as a substrate. The samples were hydrothermally treated at 85 °C for 9 h. Then, after washing them with deionized water and annealing at 400 °C for 2 h at a heating rate of 10 °C/min, the Nb_2O_5-TNTs was formed.

2.4. Material Characterization

X-Ray Diffraction (XRD) analysis of the samples was carried out using Philips (PW 3710) X-ray diffractometer with graphite monochromatized Co kα radiation (λ= 1.78901 Å) in the angle range of 5 to 85 degrees with a step of 0.02 degrees per minute. In addition, Field Emission Scanning Electron Microscopy (FESEM) equipped with energy-dispersive X-ray spectroscopy was carried out using Mira 3-XMU. The FT-IR spectra were measured by Pekin-Elmer (spectrum 400).

2.5. Electrode Fabrication and Electrochemical Measurement

The electrochemical performance of the synthesized TNTs and Nb_2O_5-TNTs was evaluated by the half-cell design in a coin cell. Two electrodes of electrochemical cells were constructed in an Ar-filled glovebox. The TNTs on Ti sheet and Nb_2O_5-TNTs composite (binder-free and carbon-free) were used as the working electrode with the lithium metal foil used as both reference and counter electrodes. The electrolyte utilized 1M $LiPF_6$ in EC: DMC in 1:1 vol.%. Charge-discharge tests and cyclic voltammetry were carried out through galvanostat/potentiostat (PGS 2065). The current densities from 0.019 mA/cm^2 to 0.565 mA/cm^2 with the cutoff voltage of 3.5 V vs. Li/Li$^+$ are selected for charge-discharge. The scan rates of 0.5, 1, 3, 5, 7, 10, and 20 mV/s were applied for the cyclic voltammetry test. Electrochemical Impedance Spectroscopy (EIS) was applied over the frequency range of 1 MHz to 1 mHz with 2 V amplitude AC voltage by EG & G (parstat 2273, USA).

In order to calculate the size of a specific surface area of an anode, TNTs were assumed as a perfect cylinder according to the Ortiz approach [27]. Following the approximation of a number of nanotubes, the measured area of every nanotube through the 2π(R-r)*h formula is multiplied by the number of nanotubes. In this method, R is the outer radius, r the inner radius, and h the height of each cylinder (nanotube).

3. RESULTS AND DISCUSSION

3.1. Structural Characterization

Fig. 1a shows the XRD pattern of TNTs with the main high-intensity peak of (101) observed at 25°. The crystal structure of TNTs is tetragonal with l41/amd space group, lattice parameters of a=3.78 Å and c=9.5 Å, and cell volume of 136.25 Å^3. The average crystallite size for (101) direction of TNTs is calculated through the Sherrer formula [32] as 27 nm with 0.62% lattice strain. The six other peaks of Ti are related to the substrate of TNTs in the anodizing method. The crystal structure of titanium is hexagonal with the P63/mmc space group and cell volume of 35.30 Å^3. Fig. 1b shows the XRD pattern of Nb_2O_5 nanoparticles at 880 °C, corresponding to the orthorhombic crystallite phase (T-Nb_2O_5). The average crystallite size is calculated by 80 nm with a strain lattice of 0.14%. In addition, the large ratio of c/a and huge volume lattice are the main parameters for easy movement of Li^+ into lattice through open channels, which are measured as 0.64 Å and 711.6 Å^3, respectively, for T-Nb_2O_5.

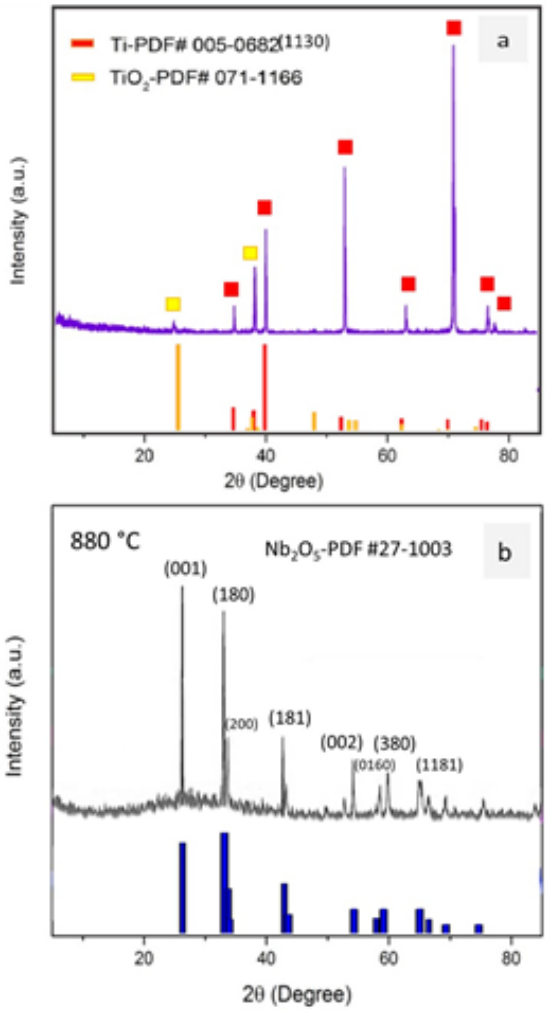

Figure 1. X-ray diffraction analysis of a) TNTs via anodizing method and b) Nb_2O_5 at 880 °C

Fig. 2a shows the homogeneity morphology of the synthesized titania nanotubes using the electrochemical anodization at 20 V. In the anodization process, first, an oxidant layer is formed on the titanium substrate. Then,

some pores and pits are formed on the oxidant layer, thus leading to the formation of nanotubes [34]. As seen in Fig. 2b, TNTs with the average inner and outer diameters of 70 and 88 nm, respectively, are well-oriented without any breakage. The synthesized Nb_2O_5 nanoparticles possess an average diameter of 41±10 nm which was already reported in the literature [33]. To the best of the author's knowledge, ultrasonic energy forms pressure cycles and increases pressure locally whether the temperature remains constant or not; consequently, liquid water is transformed to steam and cavitation happens. Then, cavitation produces a strong shear force called jet liquid. Therefore, nucleation follows a different route, and nuclei are broken into smaller ones [35,36]. Fig. 2d demonstrates the TNTs decorated by Nb_2O_5 nanoparticles (NPs) which are decorated among the walls. In addition, there are some NP clusters on the top surface of the TNTs. A wide dispersion of all Ti, Nb, and O elements on the TNT surface, as shown in Fig. 2e, illustrates an interesting decoration among walls. Moreover, weight percentages of 0.36, 70.88, and 28.75 for Ti, Nb, and O, respectively, confirm the presence of Nb_2O_5 decorated on TNTs with no sign of impurity and contaminant.

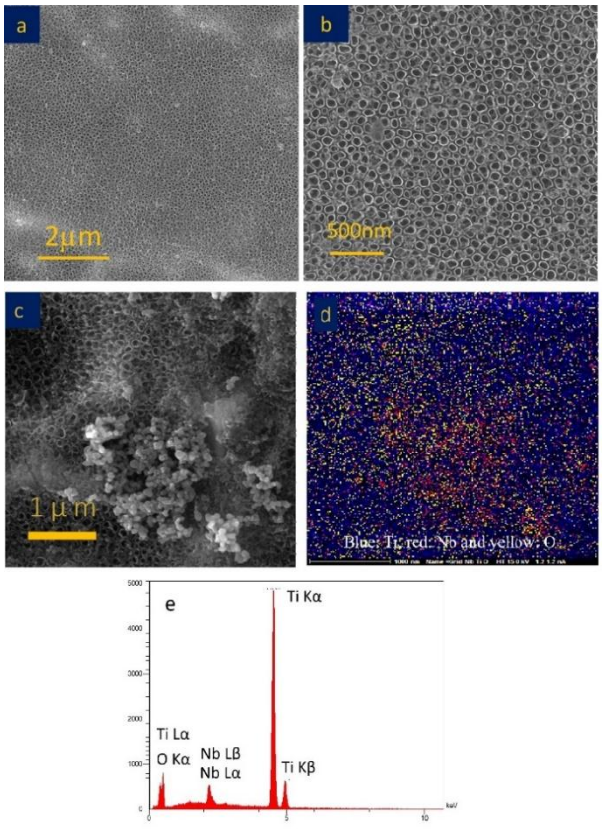

Figure 2. The FESEM images of a, b) TNTs in two different magnifications, c) Nb_2O_5-TNTs composite synthesized through hydrothermal and calcined at 400 °C, d) EDS map of the Nb_2O_5-TNTs composite, and e) EDS spectra of the Nb_2O_5-TNTs composite

3.2. Electrochemical Performance

Figs. 3a and 3c show the cyclic voltammetry of TNTs at the scan rate of 1 mV/s. According to Equation 1, an anodic peak at 2.16 V corresponds to the oxidation of Li^+ from the lattice of TNTs, and the reduction peak at 1.66 V is observed during the lithiation process.

$$xLi^+ + xe^- + TiO_2 \leftrightarrow Li_xTiO_2 \quad (1)$$

Moreover, the electrochemical behavior of Nb_2O_5-TNT anode was investigated through the cyclic voltammetry at the same scan rate. As observed in Figs. 3b and 3d, the electrochemical activity of $Nb^{+5} \leftrightarrow Nb^{+3}$ during oxidation and reduction of Li^+ ion into the Nb_2O_5 structure, according to Equation 2, occurs between 1.25 and 2.25 V.

$$xLi^+ + xe^- + Nb_2O_5 \leftrightarrow Li_xNb_2O_5 \quad (2)$$

This peak is not sharp, thus indicating the intercalation and surface energy storage. It is also indicative of the amorphous shape, low crystallinity, and low electrolyte conduction.

3.2.1. Investigation of Pseudocapacitive Behavior of TNTs and Nb_2O_5-TNTs Anodes

To investigate the pseudocapacitive behavior, separating diffusion-controlled and surface-controlled contributions of lithium storage in TNTs and Nb_2O_5-TNTs, cyclic voltammograms are taken at different scan rates. The relation between current (i) and scan rate (ν) is elaborated through Equation 3, where a and b are the constant coefficients. The value of b varies from 0.5 to 1. In case b is 0.5, the lithium storage is completely diffusion-controlled and if it is 1, the lithium storage is totally capacitive-controlled. In the middle values between 0.5 and 1, both contributions of diffusion and surface storage are implied [37].

$$i = a\nu^b \quad (3)$$

The b value is derived from the slope of the plot of ln i-ln ν, derived from CV curves in Figs. 3a and 3b, according to Equation 4.

$$\ln i = b \ln \nu + \ln a \quad (4)$$

Figs. 4a and 4b depict the slope of ln i-ln ν by cyclic voltammetry in both oxidation and reduction states for TNTs, respectively. The slope parameters for oxidation and reduction are calculated as 0.66 and 0.63, respectively. Since this value is between 0.5 and 1, it has both diffusion-controlled and surface-controlled contributions.

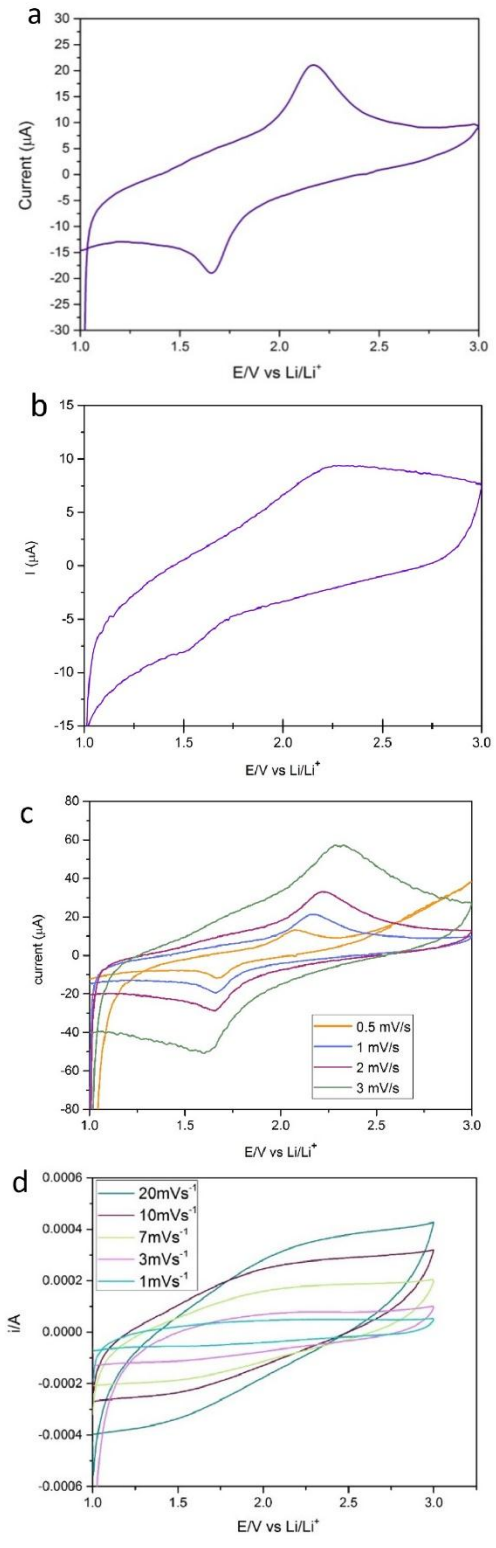

Figure 3. Cyclic voltammetry of a) TNTs in 1 mV/s, b) Nb_2O_5 in 1 mV/s, c) cyclic voltammetry of TNTs in 0.5, 1, 2 and, 3 mV/s, and d) cyclic voltammetry for Nb_2O_5-TNTs electrode in 1, 3, 7, 10, and 20 mV/s

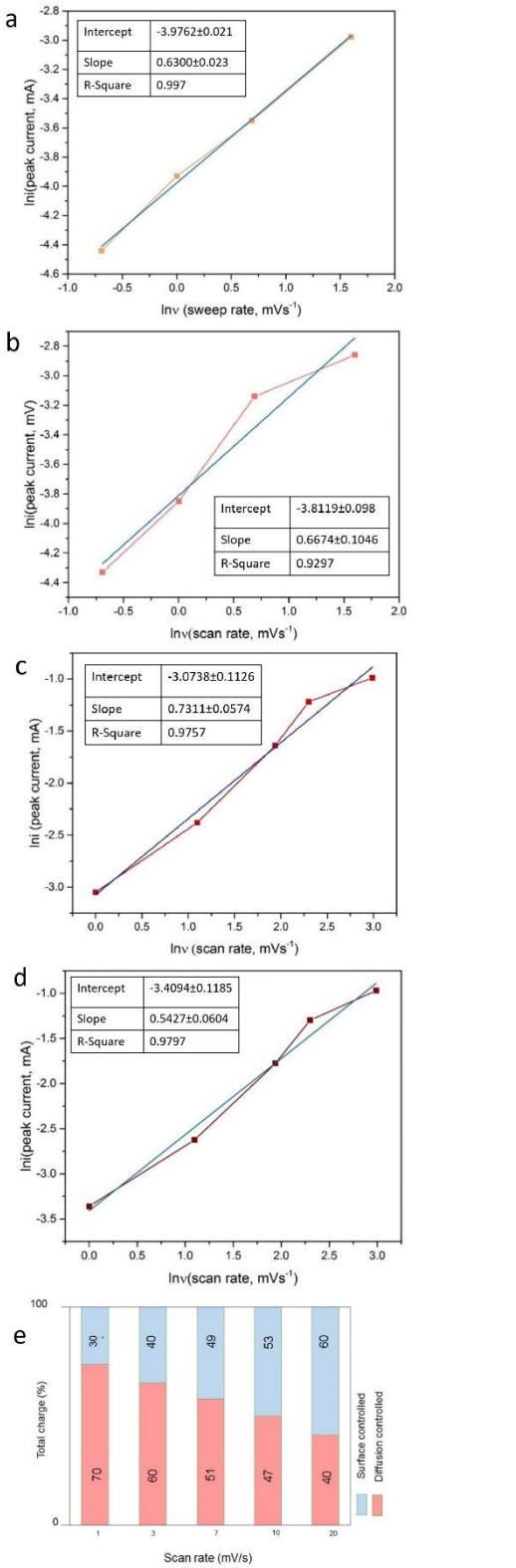

Figure 4. a) lni-lnν in TNTs oxidation, b) lni-lnν in TNTs reduction, C) lni-lnν in Nb_2O_5-TNTs oxidation, d) lni-lnν in Nb_2O_5-TNTs reduction, and e) surface to diffusion contribution in lithium-ion storage in Nb_2O_5-TNTs composites

Moreover, Figs. 4c and 4d show the slopes of ln i-ln ν for Nb_2O_5-TNTs anode in terms of defining capacitive and diffusive control contributions in oxidation and reduction procedures. The slope values for oxidation and reduction are 0.84 and 0.73, respectively, between 0.5 (diffusion-controlled) and 1 (surface-controlled). Therefore, they have both capacitive and diffusion-controlled contributions [38]. A comparison of these values in TNTs and Nb_2O_5-TNTs shows that $b_{Nb\text{-}Ti} > b_{TNTs}$. This inequality is true in oxidation and reduction procedures. Therefore, capacitive contribution in Nb_2O_5-TNTs anode is more than that in TNTs anode since as expected, Nb_2O_5-TNTs anode has better pseudocapacitive storage than TNTs anode.

The restricted area by CV is indicative of the surface charge storage contribution (pseudocapacitance and double layer) and diffusion-controlled process (lithium intercalation). Upon increasing the scan rate, cyclic voltammetry area would increase due to more lithium-ion storage, hence higher charge storage at higher rates. The Nb_2O_5-TNTs electrode can store energy in surface reaction. In order to separate capacitive and diffusion-controlled contributions, the peak current in CV is plotted versus ν and $\nu^{1/2}$, according to Equation 5, where $k_1\nu$ denotes capacitive storage due to fast kinetics and $k_2\nu^{1/2}$ presents the diffusion-controlled terms due to sluggish kinetics [8,11,32].

$$i_g = k_1\nu + k_2\nu^{1/2} \quad (5)$$

As shown in Fig. 4e, the ratio of surface to diffusion contribution increases upon increasing the scan rate from 1 mV/s to 20 mV/s in the Nb_2O_5-TNTs composite anode. As a result, the surface storage increases from 30% to 60% of the total charge storage at high sweep rates that mean more pseudocapacitive behavior and less intercalative behavior.

3.2.2. Charge and Discharge Performance

Fig. 5a shows the areal capacity of TNTs at 0.019 mA/cm^2. The initial charge and discharge capacities are 0.045 mAh/cm^2 and 0.018 mAh/cm^2, respectively. The second charge and discharge capacities are reduced to 0.026 mAh/cm^2 and 0.028 mAh/cm^2, respectively, due to the SEI layer formation on the electrode-electrolyte interface. The lithiation and de-lithiation plateaus at around 1.5-2 and 2-2.5 V are in agreement with the cyclic voltammogram of TNTs. The initial, second, and third charge capacities at 0.097 mA/cm^2, as can be seen in Fig 5b, are 0.009 mAh/cm^2, 0.015 mAh/cm^2, and 0.0137 mAh/cm^2, respectively, and the initial, second, and third discharge capacities are 0.0125 mAh/cm^2, 0.0138 mAh/cm^2, and 0.0195 mAh/cm^2, respectively.

Fig. 5c shows the areal capacity of Nb_2O_5-TNTs at 0.113 mA/cm^2. The first charge and discharge capacities are 0.412 mAh/cm^2 and 0.209 mAh/cm^2, respectively.

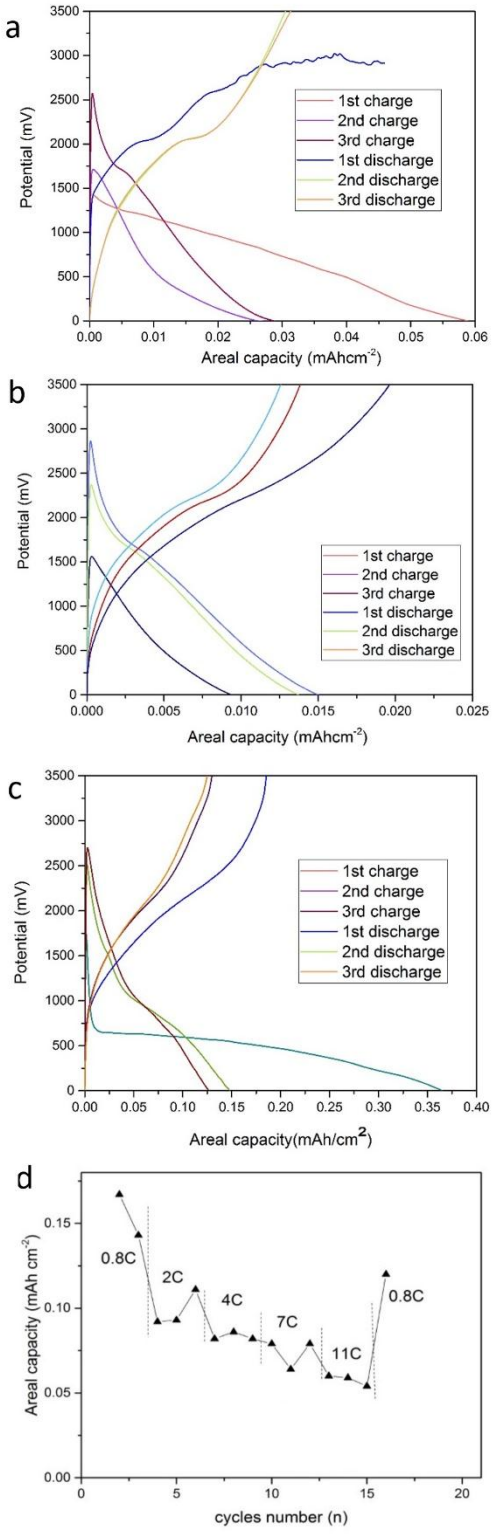

Figure 5. a) Initial, second, and third charges and discharges of TNTs anode at 0.019 mA/cm^2, b) Initial, second, and third charges and discharges of TNTs anode at 0.097 mA/cm^2, c) Initial, second, and third charges and discharges of Nb_2O_5-TNTs anode at 0.113 mA/cm^2, and d) Rate capability of Nb_2O_5-TNTs anode at different rates of 0.8 C, 2 C, 4 C, 7 C, and 11 C

The second charge and discharge capacities are reduced by 0.167 mAh/cm^2 and 0.146 mAh/cm^2, respectively, owing to the formation of a stable SEI. Like the TNTs anode, the plateaus of lithiation and de-lithiation are 0.5-1.5 V and 2-2.5 V being in line with cyclic voltammetry for Nb_2O_5-TNTs composite.

Fig. 5d shows the rate capability of Nb_2O_5-TNTs anode for 16 cycles at different rates. As can be seen, the areal capacity is reduced from 0.16 mAh/cm^2 at 0.8 C to 0.09 mAh/cm^2 at 2C, to 0.08 mAh/cm^2 at 4 C, and to approximately 0.06 mAh/cm^2 at 11 C. Of note, 1 C is equal to full-lithiation of a bulk material during one hour. Nonetheless, when the applied current turns back to 0.8 C, the areal capacity of 0.12 mAh/cm^2 is recovered. Furthermore, coulombic efficiency in the 16th cycle is measured around 86% which is an indicator of structural stability of Nb_2O_5-TNTs electrode at high current rates.

3.2.3. Electrochemical Impedance Spectroscopy

The EIS experiments are evaluated after 20 cycles at the state discharge of 50 %. The Nyquist curves of TNTs and Nb_2O_5-TNTs and corresponding equivalent circuits are plotted in Fig. 6. The equivalent circuit for both TNTs and Nb_2O_5-TNTs consists of electrolyte resistance (Rs), constant phase element, charge transfer resistance (Rp), and Warburg impedance. Rs is measured to be 21 Ω for TNTs and 24 Ω for Nb_2O_5-TNTs. Differences in ohmic resistances are caused by separator and series connections. Moreover, Rp is calculated to be 680 Ω for Nb_2O_5-TNTs and 750 Ω for TNTs. Decrement of charge transfer resistance in Nb_2O_5-TNTs anode is due to pseudocapacitance charge storage. Furthermore, Warburg impedance is equal to 470 Ω for Nb_2O_5-TNT and 3400 Ω for TNTs. Increment of Warburg impedance in TNTs is followed by intercalation diffusion of lithium-ion in lattice structure, whereas in Nb_2O_5-TNTs, the mechanism is surface-controlled.

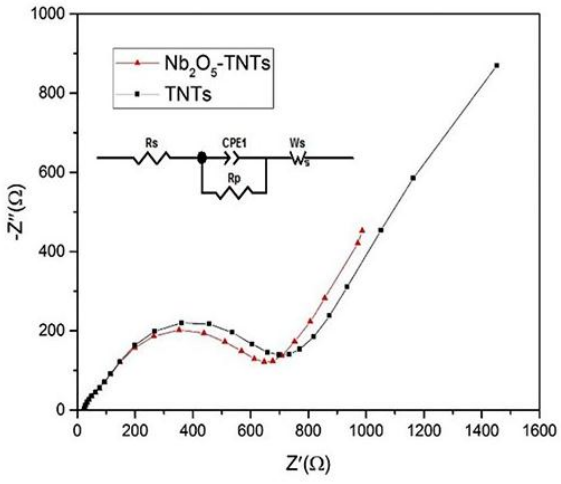

Figure 6. The Nyquist spectra with an equivalent circuit of TNTs and Nb_2O_5

Fig 7. shows the surface of the Nb_2O_5-TNT composite after cycling. As can be seen, the surface of the electrode is covered by Solid-Electrolyte Interface (SEI). Moreover, the Nb_2O_5 nanoparticles are swelled due to surface capacitance. In addition, core of each TNT is filled by lithium compounds during Li^+-ion intercalation.

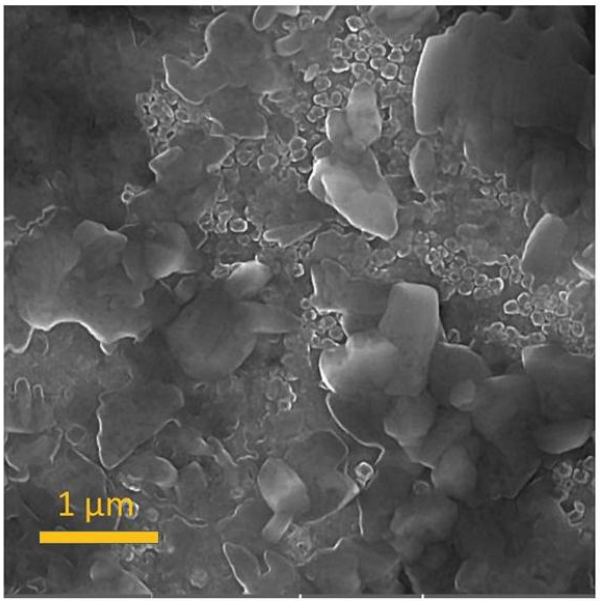

Figure 7. The surface characterization of the Nb_2O_5-TNT anode after cycling.

4. CONCLUSION

In summary, Nb_2O_5 nanoparticles were synthesized by sonochemical method and the average diameter of 41 nm to obtain desirable pseudocapacitive characteristics. Titania nanotubes with an external radius of 88 nm were successfully synthesized using the anodization process at 20 V. The Nb_2O_5 nanoparticles were decorated on titania nanotubes via hydrothermal method. The electrochemical characteristics of Nb_2O_5-TNTs and TNTs were analyzed by cyclic voltammetry, galvanostatic charge/discharge tests, and EIS. The CV curve of titania nanotubes showed oxidation and reduction peaks at 2.16 and 1.66 V, respectively, being inconsistent with titania nanotubes studies. The CV curve of Nb_2O_5-TNTs anode revealed pseudocapacitive behavior with 60% capacitive storage at 20 mV/s. The initial charge and discharge areal capacities of TNTs at 0.019 mA/cm^2 were reported 0.045 mAh/cm^2 and 0.018 mAh/cm^2, while the Nb_2O_5-TNTs composite showed the areal charge and discharge capacities of 0.167 mAh/cm^2 and 0.146 mAh/cm^2 at 0.113 mA/cm^2. Moreover, the charge transfer resistance in TNTs declined from 750 Ω to 680 Ω upon decoration by Nb_2O_5.

ACKNOWLEDGEMENT

This research project was funded by the Materials and Energy Research Institute with grant number 471394051.

REFERENCES

1. Nitta, N., Wu, F., Lee, J. T., Yushin, G., "Li-ion battery materials: present and future", ***Materials Today***, Vol. 18, No. 5, (2015), 252-264. https://doi.org/10.1016/j.mattod.2014.10.040
2. Ning, H., Pikul, J. H., Zhang, R., Li, X., Xu, S., Wang, J., Rogers, J. A., King, W. P., Braun, P. V., "Holographic patterning of high-performance on-chip 3D lithium-ion microbatteries", ***Proceedings of the National Academy of Sciences***, Vol. 112, No. 21, (2015), 6573-6578. https://doi.org/10.1073/pnas.1423889112
3. Goriparti, S., Miele, E., De Angelis, F., Di Fabrizio, E., Zaccaria, R. P., Capiglia, C., "Review on recent progress of nanostructured anode materials for Li-ion batteries", ***Journal of Power Sources***, Vol. 257, (2014), 421-443. https://doi.org/10.1016/j.jpowsour.2013.11.103
4. Oudenhoven, J. F., Baggetto, L., Notten, P. H., "All-solid-state lithium-ion microbatteries: a review of various three-dimensional concepts", ***Advanced Energy Materials***, Vol. 1, No. 1, (2011), 10-33. https://doi.org/10.1002/aenm.201000002
5. Feng, X., Li, Q., Wang, K., "Waste Plastic Triboelectric Nanogenerators Using Recycled Plastic Bags for Power Generation", ***ACS Applied Materials and Interfaces***, Vol. 13, No. 1, (2021), 400-410. https://doi.org/10.1021/acsami.0c16489
6. Tang, Y., Zhang, Y., Li, W., Ma, B., Chen, X., "Rational material design for ultrafast rechargeable lithium-ion batteries", ***Chemical Society Reviews***, Vol. 44, No. 17, (2015), 5926-5940. https://doi.org/10.1039/c4cs00442f
7. Kai, W., Xiao, F., Jinbo, P., Jun, R., Chongxiong, D., Liwei, L., "State of charge (SOC) estimation of lithium-ion battery based on adaptive square root unscented kalman filter", ***International Journal of Electrochemical Science***, Vol. 15, No. 9, (2020), 9499-9516. https://doi.org/10.20964/2020.09.84
8. Augustyn, V., Simon, P., Dunn, B., "Pseudocapacitive oxide materials for high-rate electrochemical energy storage", ***Energy and Environmental Science***, Vol. 7, No. 5, (2014), 1597-614. https://doi.org/10.1039/c3ee44164d
9. Griffith, K. J., Forse, A. C., Griffin, J. M., Grey, C. P., "High-Rate Intercalation without Nanostructuring in Metastable Nb_2O_5 Bronze Phases", ***Journal of the American Chemical Society***, Vol. 138, No. 28, (2016), 8888-8899. https://doi.org/10.1021/jacs.6b04345
10. Augustyn, V., Come, J., Lowe, M. A., Kim, J. W., Taberna, P. L., Tolbert S. H, Abruña, H. D., Simon, P., Dunn, B., "High-rate electrochemical energy storage through Li+ intercalation pseudocapacitance", ***Nature Materials***, Vol. 12, No. 6, (2013), 518-522. https://doi.org/10.1038/nmat3601
11. Brezesinski, K., Wang, J., Haetge, J., Reitz, C., Steinmueller, S. O., Tolbert, S. H., Smarsly, B. M., Dunn, B., Brezesinski, T., "Pseudocapacitive Contributions to Charge Storage in Highly Ordered Mesoporous Group V Transition Metal Oxides with Iso-Oriented Layered Nanocrystalline Domains", ***Journal of the American Chemical Society***, Vol. 132, No. 20, (2010), 6982-6990. https://doi.org/10.1021/ja9106385
12. Zhao, Y., Gao, X., Gao, H., Jin, H., Goodenough, J. B., "Three Electron Reversible Redox Reaction in Sodium Vanadium Chromium Phosphate as a High-Energy-Density Cathode for Sodium-Ion Batteries", ***Advanced Functional Materials***, Vol. 30, No. 10, (2020), 1908680. https://doi.org/10.1002/adfm.201908680
13. Zhao, Y., Gao, X., Gao, H., Dolocan, A., Goodenough, J. B., "Elevating Energy Density for Sodium-Ion Batteries through Multielectron Reactions", ***Nano Letters***, Vol. 21, No. 5, (2021), 2281-2287. https://doi.org/10.1021/acs.nanolett.1c00100
14. Zhao, Y., Ding, C., Hao, Y., Zhai, X., Wang, C., Li, Y., Li, J., Jin, H., "Neat Design for the Structure of Electrode To Optimize the Lithium-Ion Battery Performance", ***ACS Applied Materials and Interfaces***, Vol. 10, No. 32, (2018), 27106-27115. https://doi.org/10.1021/acsami.8b00873
15. Wang, C., Zhao, Y., Su, D., Ding, C., Wang, L., Yan, D., Li, J., Jin, H., "Synthesis of NiO Nano Octahedron Aggregates as High-Performance Anode Materials for Lithium Ion Batteries", ***Electrochimica Acta***, Vol. 231, (2017), 272-278. https://doi.org/10.1016/j.electacta.2017.02.061
16. Guan, L., Yu, L., Chen, G. Z., "Capacitive and non-capacitive faradaic charge storage", ***Electrochimica Acta***, Vol. 206, (2016), 464-478. https://doi.org/10.1016/j.electacta.2016.01.213
17. Wang, K., Liu, C., Sun, J., Zhao, K., Wang, L., Song, J., Duan, C., Li, L., "State of charge estimation of composite energy storage systems with supercapacitors and lithium batteries", ***Complexity***, (2021), 2021. https://doi.org/10.1155/2021/8816250
18. Gogotsi, Y., Penner, R. M., "Energy storage in nanomaterials–capacitive, pseudocapacitive, or battery-like?", ***ACS Nano***, Vol. 12, No. 3, (2018), 2081-2083. https://doi.org/10.1021/acsnano.8b01914
19. Conway, B. E., ***Electrochemical Supercapacitors: Scientific Fundamentals and Technological Applications***, Springer Science & Business Media, (1999), 698. https://doi.org/10.1007/978-1-4757-3058-6
20. Wang, C., Zhao, Y., Zhai, X., Ding, C., Zhao, X., Li, J., Jin, H., "Graphene boosted pseudocapacitive lithium storage: A case of G-Fe_2O_3", ***Electrochimica Acta***, Vol. 282, (2018), 955-963. https://doi.org/10.1016/j.electacta.2018.07.022
21. Wang, K., Li, L., Zhang, T., Liu, Z., "Nitrogen-doped graphene for supercapacitor with long-term electrochemical stability", ***Energy***, Vol. 70, (2014), 612-617. https://doi.org/10.1016/j.energy.2014.04.034
22. Wei, W., Ihrfors, C., Björefors, F., Nyholm, L., "Capacity Limiting Effects for Freestanding, Monolithic TiO_2 Nanotube Electrodes with High Mass Loadings", ***ACS Applied Energy Materials***, Vol. 3, No. 5, (2020), 4638-4649. https://doi.org/10.1021/acsaem.0c00298
23. Liu, Z., Andreev, Y. G., Armstrong, A. R., Brutti, S., Ren, Y., Bruce, P. G., "Nanostructured TiO_2 (B): the effect of size and shape on anode properties for Li-ion batteries", ***Progress in Natural Science: Materials International***, Vol. 23, No. 3, (2013), 235-344. https://doi.org/10.1016/j.pnsc.2013.05.001
24. Zhang, H., Li, G. R., An, L. P., Yan, T. Y., Gao, X. P., Zhu, H. Y., "Electrochemical lithium storage of titanate and titania nanotubes and nanorods", ***The Journal of Physical Chemistry C***, Vol. 111, No. 16, (2007), 6143-6148. https://doi.org/10.1021/jp0702595
25. Wang, W., Li, Y., Li, L., Wang, L., Wang, K., "SnO_2/TiO_2 Nanocomposite Prepared by Pulsed Laser Deposition as Anode Material for Flexible Quasi-solid-state Lithium-Ion Batteries", ***International Journal of Electrochemical Science***, Vol. 15, No. 12, (2020), 11709-11722. https://doi.org/10.20964/2020.12.49
26. Wei, J., Liu, J. X., Wu, Z. Y., Zhan, Z. L., Shi, J., Xu, K., "Research on the Electrochemical Performance of Rutile and Anatase Composite TiO_2 Nanotube Arrays in Lithium-Ion Batteries", ***Journal of Nanoscience and Nanotechnology***, Vol. 15, No. 7, (2015), 5013-5019. https://doi.org/10.1166/jnn.2015.9847
27. Ortiz, G. F., Hanzu, I., Djenizian, T., Lavela, P., Tirado, J. L., Knauth, P., "Alternative Li-Ion Battery Electrode Based on Self-Organized Titania Nanotubes", ***Chemistry of Materials***, Vol. 21, No. 1, (2009), 63-67. https://doi.org/10.1021/cm801670u

28. Wang, W., Tian, M., Abdulagatov, A., George, S. M., Lee, Y. C., Yang, R., "Three-dimensional Ni/TiO_2 nanowire network for high areal capacity lithium ion microbattery applications", ***Nano Letters***, Vol. 12, No. 2, (2012), 655-660. https://doi.org/10.1021/nl203434g
29. Lou, S., Cheng, X., Gao, J., Li, Q., Wang, L., Cao, Y., Ma, Y., Zuo, P., Gao, Y., Du, C., Huo, H., "Pseudocapacitive Li+ intercalation in porous $Ti_2Nb_{10}O_{29}$ nanospheres enables ultra-fast lithium storage", ***Energy Storage Materials***, Vol. 11, (2018), 57-66. https://doi.org/10.1016/j.ensm.2017.09.012
30. Liu, G., Zhao, L., Sun, R., Chen, W., Hu, M., Liu, M., Duan, X., Zhang, T., "Mesoporous $TiNb_2O_7$ microspheres as high performance anode materials for lithium-ion batteries with high-rate capability and long cycle-life", ***Electrochimica Acta***, Vol. 259, (2018), 20-27. https://doi.org/10.1016/j.electacta.2017.10.138
31. Liu, S., Zhou, J., Cai, Z., Fang, G., Pan, A., Liang, S., "Nb_2O_5 microstructures: a high-performance anode for lithium ion batteries", ***Nanotechnology***, Vol. 27, No. 46, (2016), 46LT01. https://doi.org/10.1088/0957-4484/27/46/46lt01
32. Lübke, M., Shin, J., Marchand, P., Brett, D., Shearing, P., Liu, Z., Darr, J. A., "Highly pseudocapacitive Nb-doped TiO_2 high power anodes for lithium-ion batteries", ***Journal of Materials Chemistry A***, Vol. 3, No. 45, (2015), 22908-22914. https://doi.org/10.1039/c5ta07554h
33. Mohammadifar, M., Massoudi, A., Naderi, N., Eshraghi, M. J., "Nb_2O_5 Nanoparticles Synthesis by Chemical Surfactant-Free Methods: ltrasonic Assisted Approach", ***Advanced Ceramics Progress***, Vol. 2, No. 4, (2016), 13-17. https://doi.org/10.30501/ACP.2016.90836
34. Regonini, D., Bowen, C. R., Jaroenworaluck, A., Stevens, R., "A review of growth mechanism, structure and crystallinity of anodized TiO_2 nanotubes", ***Materials Science and Engineering: R: Reports***, Vol. 74, No. 12, (2013), 377-406. https://doi.org/10.1016/j.mser.2013.10.001
35. Kim, H. Y., Han, J. A., Kweon, D. K., Park, J. D., Lim, S. T., "Effect of ultrasonic treatments on nanoparticle preparation of acid-hydrolyzed waxy maize starch", ***Carbohydrate Polymers***, Vol. 93, No. 2, (2013), 582-588. https://doi.org/10.1016/j.carbpol.2012.12.050
36. Sun, L., Li, J., Wang, C., Li, S., Lai, Y., Chen, H., Lin, C., "Ultrasound aided photochemical synthesis of Ag loaded TiO_2 nanotube arrays to enhance photocatalytic activity", ***Journal of Hazardous Materials***, Vol. 171, No. 1-3, (2009), 1045-1050. https://doi.org/10.1016/j.jhazmat.2009.06.115
37. Lindström, H., Södergren, S., Solbrand, A., Rensmo, H., Hjelm, J., Hagfeldt, A., Lindquist, S. E., "Li+ Ion Insertion in TiO_2 (Anatase). 2. Voltammetry on Nanoporous Films", ***The Journal of Physical Chemistry B***, Vol. 101, No. 39, (1997), 7717-7722. https://doi.org/10.1021/jp970490q
38. Venkatachalam, P., Kesavan, T., Maduraiveeran, G., Kundu, M., Sasidharan, M., "Self-assembled mesoporous Nb_2O_5 as a high performance anode material for rechargeable lithium ion batteries", ***Materials Research Express***, Vol. 6, No. 3, (2018), 035502. https://doi.org/10.1088/2053-1591/aaf350

Advanced Ceramics Progress: Vol. 7, No. 2, (Spring 2021) 10-15

Materials and Energy Research Center
MERC

Contents lists available at ACERP

Advanced Ceramics Progress

Journal Homepage: www.acerp.ir

Original Research Article

Role of Etching Process of SiC Particles on the Microstructure and Mechanical Properties of Stir Casted Al357−SiC Metal matrix Composite

A. Talezari [a], A. R. Souri [b]*, A. Shanaghi [c]*

[a] *MS, Department of Materials Engineering, Faculty of Engineering, Malayer University, Malayer, Hamedan, Iran*
[b] *Assistant Professor, Department of Materials Engineering, Faculty of Engineering, Malayer University, Malayer, Hamedan, Iran*
[c] *Associate Professor, Department of Materials Engineering, Faculty of Engineering, Malayer University, Malayer, Hamedan, Iran*

ARTICLE INFO

Article History:

Received 15 June 2021
Received in revised form 07 July 2021
Accepted 14 July 2021

Keywords:

Electromagnetic Stir Casting
Etching
Aluminum Matrix Composites
Micron-Sized SiC
Mechanical Properties

ABSTRACT

Owing to their high strength-to-weight ratio, aluminum-ceramic composites, are widely used in various industries. In this study, aluminum matrix composite was fabricated with only 2 wt% micron-sized SiC particles as the reinforcing phase using electromagnetic stir casting. Prior to mixing, the surface of SiC particles were chemically etched by HF, NaOH, and KOH at two heat treatment temperatures of 460 and 510 °C for 30 min. The obtained results indicated better wettability and interaction between the etched SiC particles and Al matrix. In addition, etched SiC particle as a ceramic phase at 460 °C enhanced the mechanical properties of Al as a metal matrix, such as enhancing hardness and E about of 6.6 and 26.6%, respectively, mainly due to the increasing inhibition against movement of dislocation confirmed by the observed brittle behavior of fracture surface.

https://doi.org/10.30501/ACP.2021.289601.1066

1. INTRODUCTION

In the past few decades, numerous studies have investigated the production of low-cost, lightweight metal matrix composites. To this end, aluminum and its low-density alloys were used as matrix materials with several carbon and ceramic particles as the reinforcing materials [1-5]. Among metal matrix composites, Aluminum Metal Matrix Composites (AMMCs) have received significant attention in recent years. They are used in the aerospace (e.g., aircraft parts), automobiles and electronics industries, mainly due to their lightweight, low coefficient of Thermal Expansion (CTE), good machinability and enhanced mechanical properties including 0.2% Yield Stress (YS), Ultimate Tensile Stress (UTS) and stiffness [6-13]. Metal Matrix Composites (MMCs) are the combinations of both metals (ductility and toughness) and ceramic properties (strength and high module). Among famous metal matrix composites, aluminum matrix composites along with reinforcing materials such as Al_2O_3, B_4C, SiC and TiC improved their mechanical properties, and increased the strength-to- weight ratio. Development of SiC reinforced aluminum matrix composites has drawn considerable attention due to their lightweight, toughness, suitable elastic module, high erosion resistance, low thermal

* Corresponding Author Email: arsouri@gmail.com (A. R. Souri), alishanaghi@gmail.com, a.shanaghi@malayeru.ac.ir (A. Shanaghi)
URL: https://www.acerp.ir/article_135650.html

Please cite this article as: Talezari, A., Souri, A. R., Shanaghi, A., "Role of Etching Process of SiC Particles on the Microstructure and Mechanical Properties of Stir Casted Al357−SiC Metal matrix Composite", ***Advanced Ceramics Progress***, Vol. 7, No. 2, (2021), 10-15. https://doi.org/10.30501/ACP.2021.289601.1066

expansion coefficient and variety of fabrication methods [14,15].

There are various composite processing methods, which can be used to make the composite such as die-casting, stirrer casting, semi-solid formation, spray formation and powder metallurgy [10,16,17]. Among these methods, stirrer casting (vortex method) is commercially considered as a low-cost method for making AMMC, owing to its simplicity, flexibility, and application in high volume production. Among all available AMMC production routes, stirrer casting is the most cost-effective one that and allows industries to produce huge components. Generally, in order to obtain AMMC through casting, the following criteria should be taken into consideration: good chemical reaction between reinforcement and matrix alloy, low porosity in the found AMMCs, high wettability between reinforcement and matrix alloy, and uniform distribution of the reinforcement particles. Wettability and reactivity between the metal matrix and ceramic particles determine the quality of the bonding materials [18-25]. Two parameters, namely volume fraction and particle size of the reinforcing particles, can singinficantly affect the performance of reinforcing particles. Upon increasing the volume fraction particles, the strength increases due to more dislocation barriers; however, the ductility decreases, because the deformation is localized on a smaller volume of the plastic matrix, thus leading to its failure to deform [26].

In the stir casting process, the resulting vortex pulls reinforcing particles into the matrix, which the particles may cluster before entering the melt on the surface of the vortex and may be transferred to a relatively stagnant area and appear as a cluster in the casting structure [27]. Sharma et al. [28] used the optimization method to analyze the distribution index of ceramic particles in aluminum and the stirring casting parameters such as stirring speed, furnace temperature and preheating temperature were also examined using surface response method optimization. Suthar et al. [29] mentioned some cases such as porosity, wettability, chemical reactions and particle distribution. These problems were solved by optimizing the stirrer casting parameters. In addition, Sahu et al. [30] used gray relationship analysis to study processing parameters such as friction factors, load and aspect ratio in cold disturbance. Dutta et al. [31] evaluated the parameters of the agitator casting process to achieve effective reinforcing particles. It was observed that stirring time and processing temperature have important effects on mechanical properties (elastic modulus and inhibition) and microstructure of composites, and Kumar et al. [32] analyzed the mechanical behavior of metal matrix composites by changing the composition of the reinforcements.

In this study, the metal matrix composite of Al A357 alloy and micro-sized SiC particles was fabricated using magnetic stir casting. The main novelty of this article is related to improve wettability between the matrix and reinforcement particles, which the SiC powder was etched by NaOH-HF and KOH solutions for better wettability and distribution, thus enhancing uniform microstructure and mechanical properties of Al-SiC composite. To meet all of the mentioned criteria, the reaction between the metal matrix and ceramic phases is critical. In this regard, just 2 wt% SiC powder is used as the reinforcement phase because the machine cannot stir heavier weight well. However, obtaining uniform microstructure, low volume of defects and agglomerated ceramic particles, and high mechanical properties gains significance in fabricating metal matrix composites, evaluated systemically using XRD, SEM, and hardness and tensile tests.

2. MATERIALS AND METHODS

Table 1 presents the chemical composition of Al357, according to magnesium conatnied in this aluminum alloy contributes to the wettability and distribution of reinforcing particles. The SiC powder as a ceramic part with the particle size of 37-100 µm, was used for fabrication of metal matrix composite. To improve the wettability and proper distribution of SiC particles in the Al matrix in this study, chemical etching of SiC powder was conducted using HF, NaOH solution, and KOH powder based on the following instructions [23-25]: first, HF chemical etching was carried out using 10 g SiC powder in 10 mL HF for 2h at 40 °C; then the powder was filtered and placed in an oven at 100 °C for 2h. Second, the obtained powder was added to the stirred NaOH solution and dried at 100 °C for 2h. Third, SiC powder and KOH with the ratio of 70:30% were placed in an electric furnace (Azar furnace) at two different temperatures of 460 and 510 °C for 30 min. Then, the powders were taken out of the furnace, rinsed with distilled water until the pH reached the value of 7, and dried at room temperature (25 °C).

TABLE 1. Chemical composition of Al 357 alloy (wt%)

Al	Si	Fe	Cu	Mn	Mg	Zn	Ti
Bal.	6.5-7.2	0.15	0.05	0.03	0.45-0.6	0.05	0.2

Firstly, the SiC particles were preheated to 80 °C to completely remove the moisture content, and then the SiC reinforcement particles were gradually added to molten alloy. In the casting stage, 2 wt% etched SiC powder and A357 alloy were placed in a fireclay crucible, in an electromagnetic furnace at a temperature of 780 °C, mixer current of 60 mA, and pressure of 8 mtorr (Figure 1). The melting and mixing times were 45 and 30 minutes, respectively, and the casting temperature was 690 °C; then, the molten was poured into the mold to make the sample for analysis.

The phase, structure, chemical composition, and microstructure of the coatings were determined by X-Ray Diffraction (XRD; Philips PW-1800 X-ray diffractometer; Cu Kα λ = 0.154056 nm), Scanning Electron Microscopy (VEGA\\TESCAN-XMU), and Energy-Dispersive X-ray Spectroscopy (EDS). In addition, hardness test was carried out using D1A InstronWol Pert under 62.5 lb in the 20s, and tensile test was done using STM-20, where the samples were fabricated according to ASTM E8.

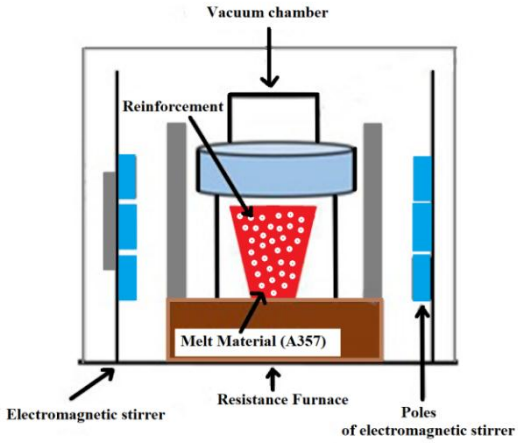

Figure 1. A schematic of the electromagnetic stir casting

3. RESULTS AND DISCUSSION

According to the XRD patterns of green SiC powder, and etched SiC powder to two temperatures of 460 °C and 510 °C in Figure 2, according to the JCPDS card No. 29-1129, all the major peaks belong to SiC with silicon carbide and moissanite structure. Here, the XRD of etched SiC powders indicate some peaks of SiC were disappeared, and changed into SiO_2 with a quartz structure at 66.47° and 76.38°, and confirm the etching process led to change the phase surface properties of SiC powders, for enhancing wettability and interaction between ceramics powder and metal matrix [33,34].

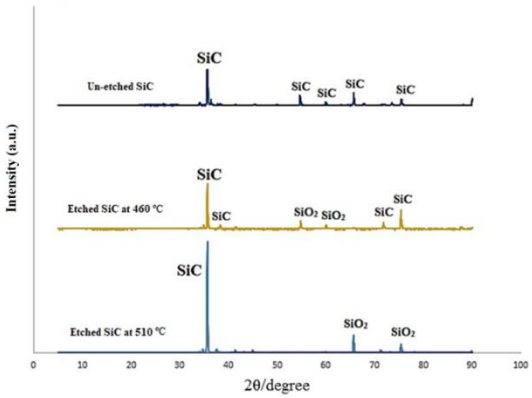

Figure 2. XRD patterns of unetched SiC, etched SiC at 460 and 510 °C

Figure 3 depicts the Back-Scattered Electrons (BSE) images of Al357, Al- un-etched SiC metal matrix composite (AS), and Al-etched SiC metal matrix composite at two different heat treatment temperatures in the etching process. The BSE images indicate that the wettability between the un-etched SiC powder and Al melting is not suitable and the particles still exist on the sample surface (Figure 3c and d). However, the etching of SiC powder causes accumulation of SiC particles in some parts of the Al- etched SiC composite, hence good distribution of SiC particles on the samples, etched at 460 °C rather than 510 °C. These microstructural properties of Al-etched SiC composite are in agreement with the results of obtained by Amirkhanlou et al. [33], Song [16] and El-Sabbagh et al. [17]. Figure 4 presents the secondary electron image of the sample etched at 460 °C to provide a better understanding of the surface of Al-etched SiC composite, demonstaring the proper reaction and relation interface between SiC particle and Al matrix, that includs more than 90% Al with silicon, magnesium and iron, respectively for particle B, which was placed next to the particle A. Part C, which is marked in white, presents the Al-Fe-Si phase.

Table 2 summarizes the mechanical properties of the samples, determined by tensile tests. The obtianed results indicated that some defects such as pores and holes could be eliminated through Ultimate Tensile Strength (UTS). The ultimate strength of thesamples etched for 30 min at 460 °C was higher than that of other samples, which heat treated at 510 °C. However, all the strength values were lower than those of the Al- unetched SiC composite. Such a low strength value would cause defects such as cavities and pores on the surface of the samples; this finding is in agreemnet with the results obtained by Lioyd et al. [15] and Balaji et al. [34]. Actually, understanding of the mam sources of the porosity could be helpful in avoiding or decreasing porosity and defect of casting. In general porosity arises from three causes, firstly, gas entrapment during stirring, secondly, hydrogen evolution, and finally, shrinkage during solidification. However, the better interface reaction between the Al matrix and etched SiC at 460 °C, could cause more shrinkage during solidification and hydrogen evolution [35], which need more detailed research about this phenomenon. In addition, the hardness of Al- unetched SiC composite is 56.8 BHN, which is similar to Al 357. However, the etching process can enhance the hardness of Al- etched SiC composite, which can be related to much wettability and the interaction between SiC particle and Al matrix. This result indicates a 12% increase in hardness by adding the SiC particles from 0 to 5%. Of note the maximum E belongs to Al- etched SiC composite heat-treated at 460 °C. Totally, the obtanied results confirmed that the etching SiC particle at 460 °C exhibits better mechanical properties than other samples.

TABLE 2. Mechanical properties such as Ultimate Tensile Strength, Brinell Hardness and Young's Modulus values of Al 357, Al- unetched SiC composite (AS), and heat treated Al-etched SiC composite at 460 °C and 510 °C

Mechanical test	Al 357	AS	460 °C	510 °C
Ultimate Tensile Strength (MPa)	181.4	201.37	191.35	181.06
Brinell Hardness (BHN)	56.8	56.8	60.54	61.1
Young's modules (MPa)	14.907	12.570	15.912	13.064

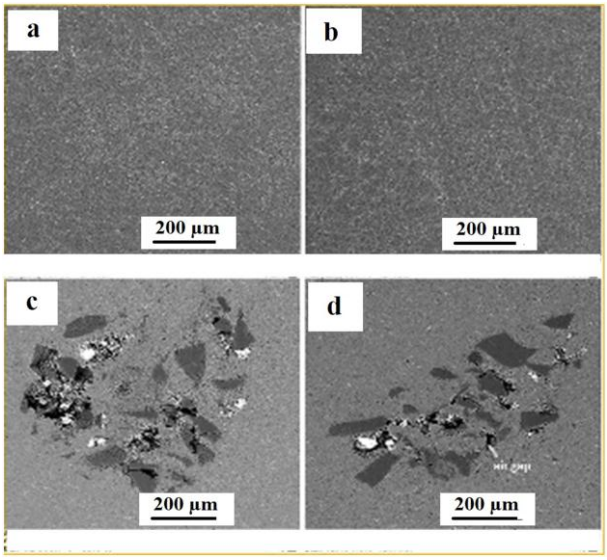

Figure 3. BSE image of, a) Al 357 b) Al-un-etched SiC composite, and heat treated Al- etched SiC composite at c) 460 °C, and d) 510 °C

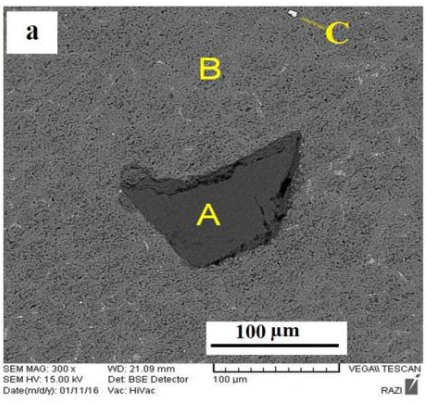

b

Element (Wt%)	series	A	B	C
Aluminum	K		**94.80**	**71.32**
Silicon	K	**76.95**	**4.81**	**7.35**
Carbon	K	**23.05**		
Iron	K		**0.33**	**21.33**
Magnesium	K		**0.06**	

Figure 4. SEM image and EDX results of heat treated Al- etched SiC composite at 460 °C

In order to better study the mechanical behavior of Al-SiC composite, the fracture surface of samples after tensile test were observed through the SEM image (Figure 5). Obviously, the Al- etched SiC composite, heat-treated at 460 °C, exhibits brittle behavior compared to other samples, mainly due to more distribution of etched SiC particles in the Al matrix. In fact, SiC as a ceramic phase enhances the mechanical properties of Al as a metal matrix due to increased inhibition against the movement of dislocation. This finding is consistent with the results of such researches as Dong et al. [26], Cioffi et al. [36] and Li et al. [37].

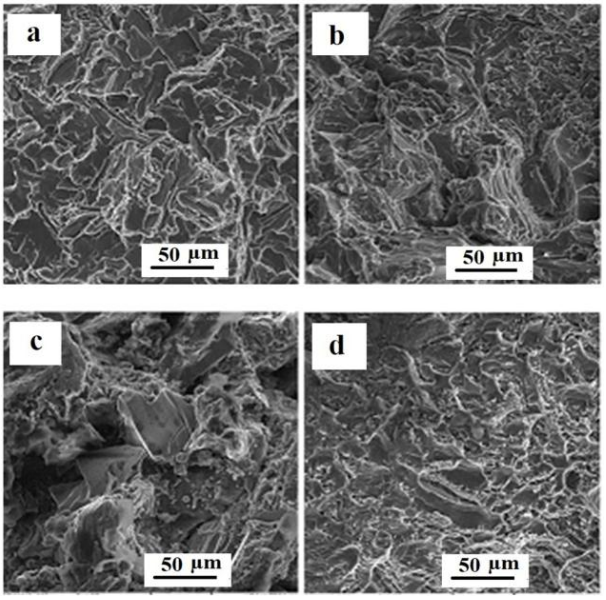

Figure 5. SEM images from the fracture surfaces of, a) Al 357 b) Al-unetched SiC composite, and heat treated Al-etched SiC composite at c) 460 °C, and d) 510 °C

4. CONCLUSION

In this study, micron-sized SiC particles were incorporated into a melt of pure aluminum using etching particles in HF, NaOH Solution and KOH powder to improve the wettability and interaction between SiC and Al matrices and fabricate aluminum matrix composite due to changes in the phase surface properties of SiC powders to SiO_2 phase, as well as good distribution of SiC particles at heat treatment temperature of 460 °C. According to the finding, the ultimate strength of samples etched for 30 min at 460 °C is higher compared to other samples, heat treated at 510 °C, and etched SiC particle as a ceramic phase at 460 °C enhanced the mechanical properties of Al as a metal matrix (enhancing hardness and E about 6.6 and 26.6%, respectively), due to increased inhibition against movement of dislocation. The fracture surface of the Al- etched SiC composite is heat treated at 460 °C, exhibits brittle behavior rather

than other samples, that can be related to more distribution etched SiC particles in the Al matrix.

ACKNOWLEDGEMENTS

This work was financially supported by Malayer University Research Grant No. 1397.

REFERENCES

1. Surappa, M. K., "Aluminum matrix composites: challenges and opportunities", ***Sadhana***, Vol. 28, No. 1-2, (2003), 319-334. https://doi.org/10.1007/BF02717141
2. Kumar, G. S. P., Koppad, P. G., Keshavamurthy, R., Alipour, M., "Microstructure and mechanical behavior of in situ fabricated AA6061-TiC metal matrix composites", ***Archives of Civil and Mechanical Engineering***, Vol. 17, No. 3, (2017), 535-544. https://doi.org/10.1016/j.acme.2016.12.006
3. Murthy, K. S., Girish, D. P., Keshavamurthy, R., Varol, T., Koppad, P. G., "Mechanical and thermal properties of AA7075/TiO_2/Fly ash hybrid composites obtained by hot forging", ***Progress in Natural Science: Materials International***, Vol. 27, No. 4, (2017), 474-481. https://doi.org/10.1016/j.pnsc.2017.08.005
4. Ram, H. A., Koppad, P. G., Kashyap, K. T., "Influence of multiwalled carbon nanotubes on the aging behavior of AA 6061 alloy matrix nanocomposites", ***Transactions of the Indian Institute of Metals***, Vol. 67, No. 3, (2014), 325-329. https://doi.org/10.1007/s12666-013-0350-y
5. Ebrahimi, M., Zarei-Hanzaki, A., Abedi, H. R., Azimi, M., Mirjavadi, S. S., "Correlating the microstructure to mechanical properties and wear behavior of an accumulative back extruded Al-Mg2Si in-situ composite", ***Tribology International***, Vol. 115, (2017), 199-211. https://doi.org/10.1016/j.triboint.2017.05.034
6. Roshan, M. R., Mousavian, T. R., Ebrahimkhani, H., Mosleh, A., "Fabrication of Al-based composites reinforced with Al_2O_3–TiB_2 ceramic composite particulates using vortex-casting method", ***Journal of Mining and Metallurgy, Section B: Metallurgy***, Vol. 49, No. 3, (2013), 299-305. https://doi.org/10.2298/JMMB120701032R
7. Valibeygloo, N., Khosroshahi, R. A., Mousavian, R. T., "Microstructural and mechanical properties of Al-4.5 wt% Cu reinforced with alumina nanoparticles by stir casting method", ***International Journal of Minerals, Metallurgy, and Materials***, Vol. 20, No. 10, (2013), 978-985. https://doi.org/10.1007/s12613-013-0824-2
8. Mohammadpour, M., Khosroshahi, R. A., Mousavian, R. T., Brabazon, D., "Effect of interfacial-active elements addition on the incorporation of micron-sized SiC particles in molten pure aluminum", ***Ceramics International***, Vol. 40, No. 6, (2014), 8323-8332. https://doi.org/10.1016/j.ceramint.2014.01.038
9. Mohammadpour, M., Khosroshahi, R. A., Mousavian, R. T., Brabazon, D., "A novel method for incorporation of micron-sized SiC particles into molten pure aluminum utilizing a Co coating", ***Metallurgical and Materials Transactions B***, Vol. 46, No. 1, (2015), 12-19. https://doi.org/10.1007/s11663-014-0186-9
10. Naher, S., Brabazon, D., Looney, L., "Development and assessment of a new quick quench stir caster design for the production of metal matrix composites", ***Journal of Materials Processing Technology***, Vol. 166, No. 3, (2005), 430-439. https://doi.org/10.1016/j.jmatprotec.2004.09.043
11. Naher, S., Brabazon, D., Looney, L., "Computational and experimental analysis of particulate distribution during Al–SiC MMC fabrication", ***Composites Part A: Applied Science and Manufacturing***, Vo. 38, No. 3, (2007), 719-729. https://doi.org/10.1016/j.compositesa.2006.09.009
12. Mousavian, R. T., Damadi, S. R., Khosroshahi, R. A., Brabazon, D., Mohammadpour, M., "A comparison study of applying metallic coating on SiC particles for manufacturing of cast aluminum matrix composites", ***The International Journal of Advanced Manufacturing Technology***, Vol. 81, No. 1, (2015), 433-444. https://doi.org/10.1007/s00170-015-7246-4
13. Boostani, A. F., Tahamtan, S., Jiang, Z. Y., Wei, D., Yazdani, S., Khosroshahi, R. A., Mousavian, R. T., Xu, J., Zhang, X., Gong, D., "Enhanced tensile properties of aluminum matrix composites reinforced with graphene encapsulated SiC nanoparticles", ***Composites Part A: Applied Science and Manufacturing***, Vol. 68, (2015), 155-163. https://doi.org/10.1016/j.compositesa.2014.10.010
14. Ray, S., "Synthesis of cast metal matrix particulate composites", ***Journal of Materials Science***, Vol. 28, No. 20, (1993), 5397−5413. https://doi.org/10.1007/BF00367809
15. Lloyd, D. J., "Particle reinforced aluminium and magnesium matrix composites", ***International Materials Reviews***, Vol. 39, No. 1, (1994), 1−23. https://doi.org/10.1179/imr.1994.39.1.1
16. Song, M., "Effects of volume fraction of SiC particles on mechanical properties of SiC/Al composites", ***Transactions of Nonferrous Metals Society of China***, Vol. 19, No. 6, (2009), 1400-1404. https://doi.org/10.1016/S1003-6326(09)60040-6
17. El-Sabbagh, A. M., Soliman, M., Taha, M. A., Palkowski, H., "Effect of rolling and heat treatment on tensile behaviour of wrought Al-SiCp composites prepared by stir-casting", ***Journal of Materials Processing Technology***, Vol. 213, No. 10, (2013), 1669-1681. https://doi.org/10.1016/j.jmatprotec.2013.04.013
18. Seo, Y. H., Kang, C. G., "Effects of hot extrusion through a curved die on the mechanical properties of SiCp/Al composites fabricated by melt-stirring", ***Composites Science and Technology***, Vol. 59, No. 5, (1999), 643-654. https://doi.org/10.1016/S0266-3538(98)00123-7
19. Xu, Y., Chung, D. D. L., "Low-volume-fraction particulate preforms for making metal-matrix composites by liquid metal infiltration", ***Journal of Materials Science***, Vol. 33, No. 19, (1998), 4707-4709. https://doi.org/10.1023/a:1004480819365
20. Naher, S., Brabazon, D., Looney, L., "Simulation of the stir casting process", ***Journal of Materials Processing Technology***, Vol. 143-144, (2003), 567-571. https://doi.org/10.1016/S0924-0136(03)00368-6
21. Seo, Y. H., Kang, C. G., "The effect of applied pressure on particle-dispersion characteristics and mechanical properties in melt-stirring squeeze-cast SiCp/Al composites", ***Journal of Materials Processing Technology***, Vol. 55, No. 3-4, (1995), 370-379. https://doi.org/10.1016/0924-0136(95)02033-0
22. Skibo, M., Morris, P. L., Lloyd, D. J., "Structure and properties of liquid metal processed SiC reinforced aluminium", In ***Cast Reinforced Metal Composites: Proceedings of the International Symposium on Advances in Cast Reinforced Metal Composites Held in Conjunction with the 1988 World Materials Congress,*** Fishman, S. G. and Dhingra, A. K. (eds.), Chicago, Illinois, 24-30 September 1988, USA: ASM International, (1988), 257-261. http://citeseerx.ist.psu.edu/viewdoc/download?doi=10.1.1.997.7513&rep=rep1&type=pdf#page=253
23. Arima, K., Hara, H., Murata, J., Ishida, T., Okamoto, R., Yagi, K., Sano, Y., Mimura, H., Yamauchi, K., "Atomic-scale flattening of SiC surfaces by electroless chemical etching in HF solution with Pt catalyst", ***Applied Physics Letters***, Vol. 90, No. 20, (2007), 202106. https://doi.org/10.1063/1.2739084
24. Weyher, J. L., "Characterization of wide-band-gap semiconductors (GaN, SiC) by defect-selective etching and complementary methods", ***Superlattices and Microstructures***, Vol. 40, No. 4-6, (2006), 279-288. https://doi.org/10.1016/j.spmi.2006.06.011

25. Van Dorp, D. H., Weyher, J. L., Kelly, J. J., "Anodic etching of SiC in alkaline solutions", ***Journal of Micromechanics and Microengineering***, Vol. 17, No. 4, (2007), S50. https://doi.org/10.1088/0960-1317/17/4/S04
26. Dong. P. Y., Zhao, H. D., Chen, F. F., Li, J. W., "Microstructures and properties of A356–10% SiC particle composite castings at different solidification pressures", ***Transactions of Nonferrous Metals Society of China***, Vol. 23, No. 8, (2013), 2222-2238. https://doi.org/10.1016/S1003-6326(13)62721-1
27. Kumar, M. S., Begum, S. R., Pruncu, C. I., Asl, M. S., "Role of homogeneous distribution of SiC reinforcement on the characteristics of stir casted Al–SiC composites", ***Journal of Alloys and Compounds***, Vol. 869, (2021), 159250. https://doi.org/10.1016/j.jallcom.2021.159250
28. Sharma, A., Rastogi, V., Agrawal, A. K., "Multi-parametric optimisation by quantitative assessment of distribution index and area fraction of composite", ***Practical Metallography***, Vol. 57, No. 9, (2020), 588–613. https://doi.org/10.3139/147.110636
29. Zhang, W. Y., Du, Y. H., Zhang, P., "Vortex-free stir casting of Al-1.5 wt% Si–SiC composite", Journal of Alloys and Compounds, Vol. 787, (2019), 206–215. https://doi.org/10.1016/j.jallcom.2019.02.099
30. Sahu, M. K., Valarmathi, A., Baskaran, S., Anandakrishnan, V., Pandey, R. K., "Multi- objective optimization of upsetting parameters of Al–TiC metal matrix composites: A grey Taguchi approach", ***Proceedings of the Institution of Mechanical Engineers, Part B: Journal of Engineering Manufacture***, Vol. 228, No. 11, (2014), 1501–1507. https://doi.org/10.1177/0954405413519434
31. Dutta, S., Narala, S. K. R., "Experimental investigation to study the effects of processing parameters on developed novel AM (Al–Mn) series alloy", ***Materials and Manufacturing Processes***, Vol. 35, No. 16, (2020), 1842-1851. https://doi.org/10.1080/10426914.2020.1813889
32. Kumar, A., Kumar, P., Singh, R. C., "The effect of alumina on mechanical behavior of Al 6064 alloy", In ***IOP Conference Series: Materials Science and Engineering***, Vol. 802, No. 1, (2020), 012004. https://doi.org/10.1088/1757-899X/802/1/012004
33. Amirkhanlou, S., Niroumand, B., "Effects of reinforcement distribution on low and high temperature tensile properties of Al356/SiCp cast composites produced by a novel reinforcement dispersion technique", ***Materials Science and Engineering: A***, Vol. 528, No. 24, (2011), 7186-7195. https://doi.org/10.1016/j.msea.2011.06.013
34. Balaji, V., Sateesh, N., Hussain, M. M., "Manufacture of aluminium metal matrix Composite (Al7075-SiC) by Stir Casting Technique", ***Materials Today: Proceedings***, Vol. 2, No. 4-5, (2015), 3403-3408. https://doi.org/10.1016/j.matpr.2015.07.315
35. Orlowicz, W., Tupaj, M., Mróz, M., Betlej, J., Ploszaj, F., "Effect of refining process on porosity and mechanical properties of high pressure Al-Si alloy die casting", ***Iranian Journal of Materials Science and Engineering***, Vol. 9, No.1, (2012), 1-10. http://ijmse.iust.ac.ir/article-1-409-en.html
36. Cioffi, F., Ibáñez, J., Fernández, R., González-Doncel, G., "The effect of lateral off-set on the tensile strength and fracture of dissimilar friction stir welds, 2024Al alloy and 17% SiC/2124Al composite", ***Materials & Design (1980-2015)***, Vol. 65, (2015), 438-446. https://doi.org/10.1016/j.matdes.2014.09.042
37. Li, X. P., Liu, C. Y., Ma, M. Z., Liu, R. P., "Microstructures and mechanical properties of AA6061–SiC composites prepared through spark plasma sintering and hot rolling", ***Materials Science and Engineering: A***, Vol. 650, (2016), 139-144. https://doi.org/10.1016/j.msea.2015.10.015

Advanced Ceramics Progress: Vol. 7, No. 2, (Spring 2021) 16-22

Materials and Energy Research Center
MERC

Contents lists available at ACERP

Advanced Ceramics Progress

Journal Homepage: www.acerp.ir

Original Research Article

Effect of Cristobalite Content on Physical, Dielectric Constant, and Bending Strength of Fused Silica Ceramics Formed by Slip Casting Method

P. Dehghani [a], F. Soleimani [b] *

[a] *Instructor, Department of Materials Engineering, Faculty of Engineering, University of Malayer, Malayer, Hamedan, Iran*
[b] *Assistant Professor, Department of Materials Engineering, Faculty of Engineering, University of Malayer, Malayer, Hamedan, Iran*

ARTICLE INFO

Article History:

Received 18 May 2021
Received in revised form 02 July 2021
Accepted 14 July 2021

Keywords:

Fused Silica
Sintering
Cristobalite
Dielectric

ABSTRACT

Fused silica ceramics are widely used in electronics and aerospace industries. In the present study, 70 µm of fused silica powder was milled to 10 µm through fast milling. The appropriate slurry was prepared for slip casting with the powder-to-water ratio of 80:20. After drying the specimens, the samples were sintered at different temperatures of 1100 °C to 1400 °C. The density increased upon increasing the temperature from 1.79 to 1.98 g/cm^3. The phase transformation of the samples was investigated using XRD. The structure of the samples was analyzed using FTIR, and their microstructure was examined using a Field Emission Scanning Electron Microscope (FESEM). The bending strength of the samples was measured using the three-point method. According to the results, the cristobalite phase increased upon increasing the sintering temperature. The best flexural strength value (48.7 MPa) was obtained for the sample sintered at 1300 °C. The dielectric constants of the fused silica ceramics were about 3-3.8 in the frequency range of 8 to 12 GHz.

https://doi.org/10.30501/ACP.2021.286931.1060

1. INTRODUCTION

Fused silica ceramics are among the most widely used materials in aerospace [1], laser interferometric [2], anti-reflective coating [3], investment casting [4], and capillary sensors [5]. Fused silica, also known as fused quartz, is a silica glass in an amorphous or non-crystalline form with no other additional components. Its main characteristics are low thermal expansion coefficient (0.54×10^{-6} /°C, 0-800 °C) [6], good corrosion resistance, and low dielectric constant (3-4 at 25-1000 °C), making it an attractive material [7–9].

One of the conventional methods for shaping fused silica ceramics is slip casting. Slip-cast fused silica is used to make radomes and heat shield for space rockets [10].

A key point about obtaining homogeneous and dense green bodies with uniform pore size distribution through the slip casting method is achieving a well-dispersed slurry with an appropriate particle size. Particles of 5 µm in diameter are commonly used to achieve a good mechanical strength [11]. The medium is usually water [12]; however, alcohol or methanol can also be used [13].

One of the main drawbacks of fused silica ceramics is their low flexural strength. As observed, the existence

* Corresponding Author Email: f-soleimani@merc.ac.ir (F. Soleimani)

https://www.acerp.ir/article_135651.html

Please cite this article as: Dehghani, P., Soleimani, F., "Effect of Cristobalite Content on Physical, Dielectric Constant, and Bending Strength of Fused Silica Ceramics Formed by Slip Casting Method", ***Advanced Ceramics Progress***, Vol. 7, No. 2, (2021), 16-22. https://doi.org/10.30501/ACP.2021.286931.1060

and value of some Silica polymorph play a major role in the mechanical strength. The three main silica polymorphs are quartz, cristobalite, and tridymite [14,15]. Some phase transformations are diffusionless, such as β-cristobalite to α-cristobalite, meaning that the bonds do not break. Moreover, this transformation can destroy the structural integrity of the material due to volume change. The other phase transformations for fused silica, such as quartz to cristobalite, are reconstructive that tend to break bonds and reform during the transformation [16,17].

Researchers have found that conversion of amorphous fused silica to cristobalite is considered a disadvantage in their application. To be specific, based on the the literature, decrease in the bending strength during the transformation of fused silica to cristobalite is the main problem. The cubic beta crystallite is converted to alpha with a tetragonal structure. This phase change occurs at about 300 °C at a relative volume change value of 5%, which is the main reason for the formation of microcracks [18].

Some preliminary studies were conducted in early 2000 by which several researchers demonstrated the effect of incorporating small fused silica particles to the main powders while making fused silica ceramics [19]. They claimed that incorporation of some fine particles to the slurry increased the yield stress that seemed to be a reliable innovative approach to the enhancement of yield stress.

In 2016, Liu et al. [3] investigated the effect of sintering temperature on phases, microstructure, and properties of fused silica [8]. Duan et al. [7] added boron nitride to reinforced fused silica composites prepared by Hot Press (HP) at different sintering temperatures. The best dielectric results were obtained at a sintering temperature of 1350 °C, thus regarding fused silica as a high-temperature electromagnetic wave transparent material.

In the present study, the effects of sintering temperature on the density, flexural strength, and dielectric properties of fused silica ceramics were reported. Further, the amount of the cristobalite phase and its effects on the mechanical strength of the sintered fused ceramics were reported.

2. MATERIALS AND METHODS

The fused silica powder used in this experiment was purchased from the Lianyungang Hantian International Factory in China, with 99.9% purity. Table 1 presents the chemical composition of the raw material. Particle size analysis (PSA-FRITSCH) was carried out to measure the particle size. The fast mill at a speed of 120 rpm was employed to mill the fused silica powder. Alumina balls with 98% purity were also used for milling and mixing.

TABLE 1. The chemical composition of fused silica raw material

Composition	Purity%
SiO_2	99.9 %
Fe_2O_3	50 ppm
Al_2O_3	100 ppm
K_2O	42 ppm
TiO_2	17 ppm
MnO	15 ppm
P_2O_5	10 ppm

In order to prepare the sample, the weight percentage ratios of solid powders to water were claculated as 70:30, 80:20, and 90:10%. All the slurries were fast-milled for 40 h for more homogenization and mixing. After 40 h of milling, the prepared slurry passed through a 300 mesh sieve. Then, casting was conducted inside gypsum molds. The cast specimens were dried in an electric oven at 50 °C for 24 h.

After slip casting the specimens, micro cracks appeared in some cases. The sintering process was performed on the crack-free specimens. The sintering of the dried bodies was conducted at 1100, 1200, 1300, and 1400 °C. The holding time at sintering temperatures was 2 h and the heating rate was 5 °C/min.

The bulk density (ρ) and apparent porosity of the sintered samples were measured based on Archimedes method (ASTM F 417). The bending strength was measured under static, monotonic, three-point bending conditions at room temperature with the lower span of 20 mm and displacement rate of 0.5 mm/min. [20]. For this purpose, the specimens were cut in cubic segments with the dimensions of 20×28.6×1 mm and then, they were ground and polished by alumina abrasive powder.

The phase composition of the samples was determined by X-Ray Diffraction (XRD; Philips Xpert MPD Co., Ltd) using Cu Kα radiation (λ = 1.5406 Å), and their microstructures were observed through field Smission Dcanning Electron Microscopy (FE-SEM; TESCAN MIRA3). The dimensions of specimens were 10×10 mm with thickness of 5 mm. The samples were cut, polished, and etched in a 5% volumetric solution of hydrofluoric acid for 10 seconds.

The cristobalite content in the sintered samples was measured by the semi-quantitative method according to the XRD results [21] obtained from the X'Pert software. The crystalline phase values of cristobalite were calculated by measuring the intensity of the crystalline peaks relative to the 100% amorphous sample.

The structural analysis of the samples was carried out using the FTIR method. The samples were first powdered and then mixed with KBr at a ratio of 1:100; finally, the FTIR spectra were obtained.

The dielectric properties (dielectric permittivity and loss tangent) of the samples were determined by a VNA

(Keysight 5063A). The method of analysis was consistent with the waveguide method and performed in the range of the X-band [22].

3. RESULTS AND DISCUSSION

Figure 1 displays the particle size change after milling. Almost 90% of the particles were <8 microns after 40h of milling. Evidently, the milling process was good enough. In the batches, the 90:10 powder-to-water sample had very high viscosity and could not be slip cast. On the contrary, the slurry of 70:30 had very low viscosity and was not appropriate for slip casting. Therefore, the 80:20 sample was chosen for the rest of the experiments. After slip casting, it was dried and sintered at different temperatures. To assess the effectiveness of the sintering process, first, the sample densities were measured. According to the results obtained from the density measurement of the samples using the Archimedes method, upon increasing the temperature, the density of the specimens increased (Table 2). This process stopped in S28 sample and density reached its maximum value of 1.98 g/cm^3.

TABLE 2. Densities and apparent porosity of the samples

Sample Code	Density (g/cm^3)	Apparent Porosity (%)	Sintering Temperature (°C)
S22	1.79±0.05	26±0.1	1100
S24	1.96±0.05	22±0.2	1200
S26	1.98±0.05	18±0.1	1300
S28	1.98±0.05	17±0.1	1400

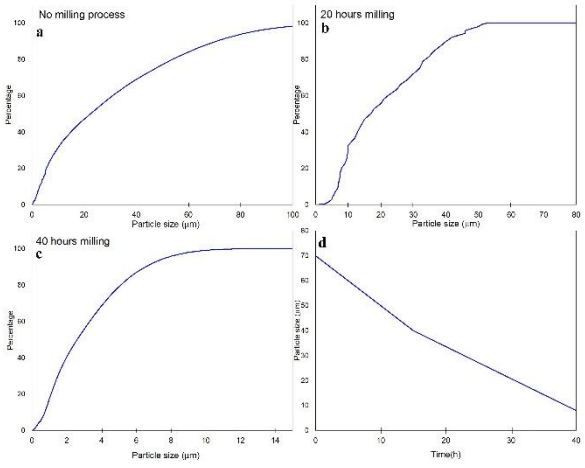

Figure 1. Particle size distribution of the primary powders before a) No milling, and after a different period of milling times: b) 20h milling, c) 40h milling, and d) Particle size change with milling time

Figure 2 depicts the diagram of porosity vs. bulk density. According to Figure 2, there is an inverse relationship between the temperature and apparent porosity. One of the reasons for the difference between the apparent porosity and bulk density is the phase transformation from amorphous SiO_2 to a cristobalite structure in the ceramic. To be specific, while the density of cristobalite is about 2.33 g/cm^3, it is about 2.2 g/cm^3 for silica glass. As a result, an increase in the density is due to not only porosity elimination but cristobalite crystallization, partly [23].

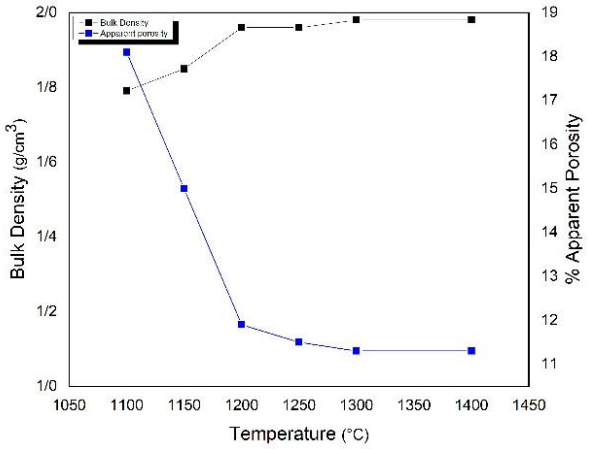

Figure 2. Relation between Bulk density, temperature, and apparent porosity in fused silica ceramics

Figure 3 depicts the images of the microstructures. According to the FESEM images in this figure, the interconnection between particles increases upon increasing the temperature. According to the FESEM images, upon increasing the sintering temperature, porosity decreases and grain sizes increase. Removing the porosity improves the dielectric constant if the cristobalite phase content is not too high. Figure 3 illustrates the formation of numerous cracks on the surface of grains in the S28 slip-cast fused silica ceramic sample. The cristobalite transformation phases usually begin from the surface of grains due to the higher heat absorption from their free surface. With an increase in the temperature from 1300 °C to 1400 °C, the grain size of particles increased and unreacted cristobalite rised. The volume changes in cristobalite after cooling at 300 °C form numerous cracks on the surface of grains, thus affecting the mechanical strength of the ceramics [24]. Whereas β-cristobalite has a cubic arrangement, α is tetragonal. The β-structure is transformed to the collapsed α structure at the ≈300 °C cooling temperature, hence occurrence of approximately a 3.2% volume reduction. The temperature of the $\propto \leftrightarrow \beta$ inversion in cristobalite is changeable which depends on the other components and crystal structure of the material.

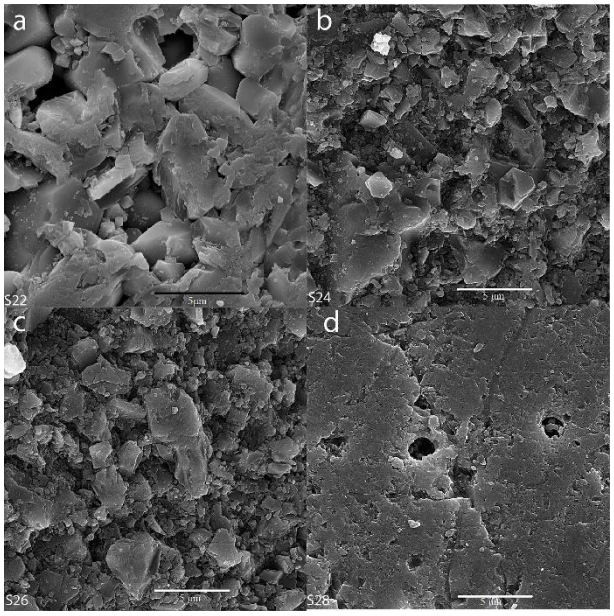

Figure 3. FESEM images of the sintered fused silica: a) S22, b) S24, c) S26, and d) S28 samples

Figure 4 shows the XRD diagram of fused silica ceramics. In this figure, the first peak with a higher intensity is observed at 21°, and the next two peaks with lower intensities were identified at 26° and 35°. The peaks at 21°, 26°, and 35° belong to the cristobalite phase. Cristobalite crystals are cubic in form with the chemical formula of Si8O16. Furthermore, upon increasing the temperature, the formation of the cristobalite phase begins. Evidently, no crystalline phases are observed in the samples (S22) and (S24) at 1100 °C and 1200 °C, repsectively. At 1300 °C (S26), those weak peaks belonging to the crystalline phase of cristobalite are observed. In the next sample, at 1400 °C (S28), the crystals grew more. At this temperature, the highest amount of cristobalite crystal growth is observed, as shown in Figure 4. The cristobalite crystals formed at the end of the sintering operation were converted from beta-cristobalite to alpha-cristobalite in the temperature range of 200 to 270 °C. In general, cristobalite can be divided into three categories in terms of weight: low (1-20%), medium (20-80%), and high (80-100%) [23]. Here, the sample (S28) with 38 wt% cristobalite phase content had the highest crystallization value among the sintered fused silica samples. Moreover, samples (S22) and (S26) with a crystalline phase value of < 5 wt% had the lowest value. The S24 sample contained 13 wt% of the cristobalite crystalline phase.

Figure 5 displays the FTIR diagrams. This analysis comprises a co MParison of the unsintered fused silica powder and sintered sample at 1400 °C. The sharp peaks in the diagrams are observed at 474, 796, 1100, 1400, 1634, 3130, and 3430. The peaks of 3000 and above belong to water and O-H bonds.

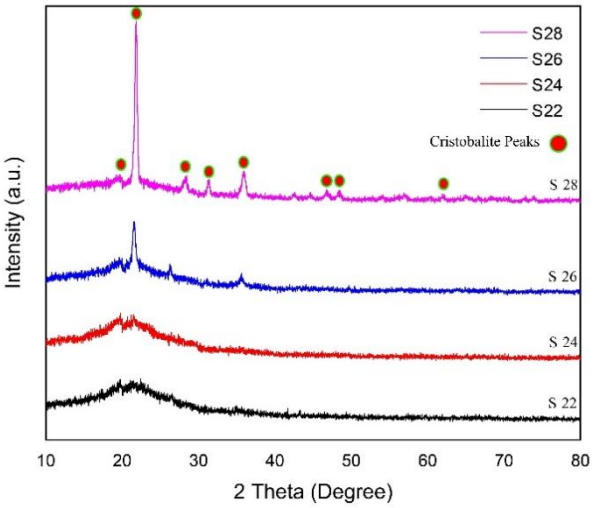

Figure 4. XRD analysis of fused silica samples, sintered at different temperatures

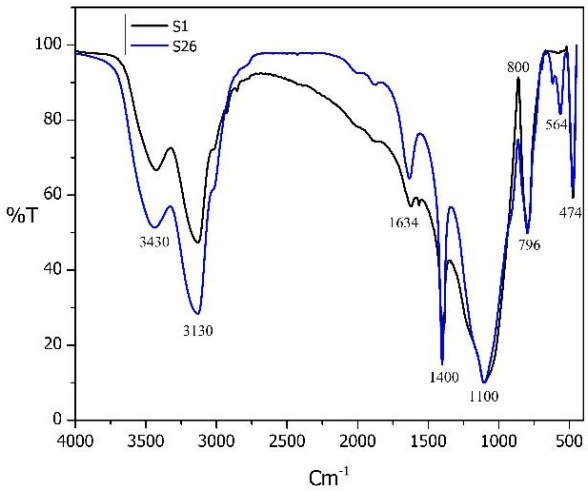

Figure 5. The FTIR analysis of fused silica powder and the sintered fused silica specimen at 1400 °C

Table 3 presents the results from the characterization of these peaks. The absorption peaks observed in the range of 800 cm^{-1} and 1080 cm^{-1} are related to Si-O vibrations in silica and those at 474 cm^{-1} to Si-O vibrations in cristobalite [14,25]. Vibrations at 1100cm^{-1} are the main structure of silica (Si-O-Si). In addition to these bond vibrations, impurities are observed in the spectroscopic diagram shown in Table 1, having smaller peaks than the original peaks. As shown in Figure 5, the peak of 564 cm^{-1} is not present in the original powder sample, and the intensity of the peaks is different in the diagrams.

The Si-O bond has a small bond length (0.162 nm) compared to the covalent radii of silicon and oxygen

(0.191 nm), which corresponds to the relatively high stability of the siloxane bond.

TABLE 3. Peaks and the type of the related bond in the FTIR analysis

Bond	Peak (cm^{-1})
Si-O bond in cristobalite	474
Si-O bond in cristobalite	621
Si-O	797
Si-OH	860
Si-O-Si	1100
(Cristobalite) Si-O	1400
OH Bond	3129, 3429

Figure 6 depicts the fracture strength diagrams of the specimens. All the specimens show brittle fracture [26]. The highest value of the fracture strength belongs to the sample (S26), which is about 49 MPa. As the sintering temperature increased to 1400 °C, the strength decreased. Due to the low sintering temperature, sample (S22) did not exhibit a good sintering behavior and, based on its density (1.79), it can be concluded that it has a high volume of porosities which reduced its mechanical strength. The maximum mechanical strength of this sample was 6.76 MPa. With an increase in the temperature to 1400 °C, the growth of the crystalline phase of cristobalite stopped, the volume change increased, and more microcracks appeared. Finally, due to the high sintering temperature and excessive growth of the cristobalite phase, the strength of fused silica ceramic after sintering at 1400 °C significantly decreased and reached 14.2 MPa.

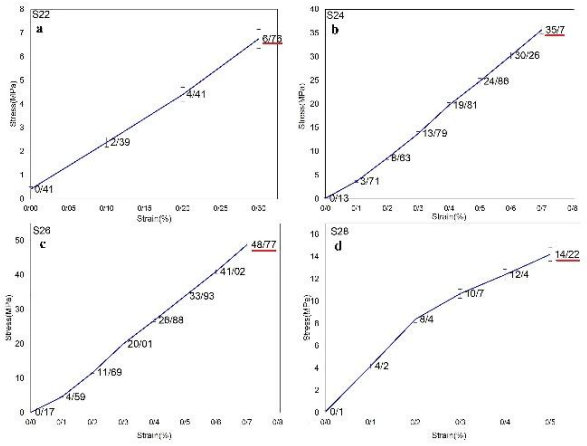

Figure 6. The bending strength of sintered fused silica specimens in the temperature range of a)1100 , b) 1200, c)1300, and d) 1400 °C

Figure 7 depicts the dielectric measurement results of the sintered samples. The dielectric constant of sample (S26) in the X-band range was 3.6, which was in agreement with the results of other studies. Evidently, samples (S24) and (S26) had the minimum noise dielectric changes. The presence of microcracks and porosities reduced the dielectric constant. Further, much noise was observed in sample (S22) due to the low density and high volume of porosities and voids. Furthermore, the low sintering temperature and less crystallized phase of cristobalite reduced the dielectric constant.

As the temperature increased, the density and porosity increased and decreased, respectively. Reduction of porosity improved the dielectric constant and eliminated noise; hence, the lowest noise was observed in samples (S24) and (S26). Upon increasing the temperature from 1200 °C to 1300 °C, the dielectric constant increased from 3.2 to 3.6.

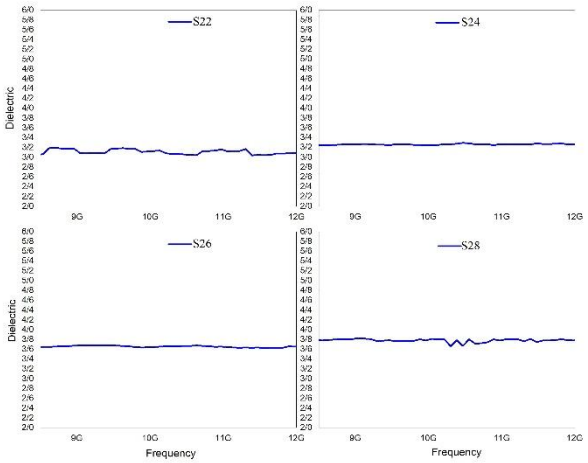

Figure 7. Dielectric constant of the samples in range of 8 to 12 GHz

Figure 8 shows the relationship between temperature and dielectric constant. With a rise in the temperature from 1100 to 1400 °C, the dielectric constant also increased. It seems that the formation of cristobalite caused an increase in the dielectric constant due to the formation of a more regular long-range structure than the amorphous phase of fused silica. The dielectric constant (ε_r) and dielectric loss increased upon increasing the grain size [27].

4. CONCLUSION

Fused silica ceramics with high density and good mechanical strength were prepared in this study. The

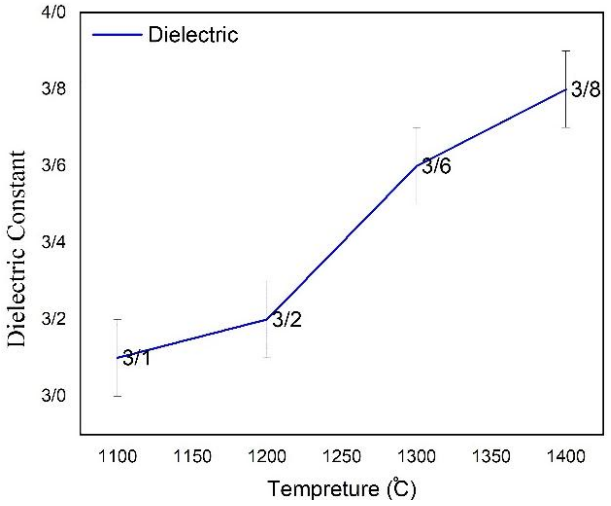

Figure 8. The relationship between dielectric and densities of the samples at the range of 1100-1400 °C

proper ratio of powder to water content in the slurry was 80:20 for good slip casing. The samples were sintered at the temperatures of 1100 to 1400 °C. It was found out that upon increasing the sintering temperature, the mechanical strength would decrease. The phase composition was studied, whose results revealed that cristobalite content would increase upon increasing the sintering temperature. The best mechanical strength and dielectric constant belonged to the sample of 1300 °C. The dielectric value of it was 3.6.

ACKNOWLEDGEMENTS

The authors tend to express their gratitudes to Malayer University for the financial support.

REFERENCES

1. Jeshrun Shalem, M., Devaraju, A., Karthik, K., "Synthesis and Characterization of Functionally Graded Ceramic Material for Aerospace Applications", In Reddy A., Marla D., Simic M., Favorskaya M., Satapathy S. (eds.), ***Intelligent Manufacturing and Energy Sustainability. Smart Innovation, Systems and Technologies***, vol 169, Springer, Singapore, (2020), 483-488. https://doi.org/10.1007/978-981-15-1616-0_47
2. Okaji, M., Yamada, N., Nara, K., Kato, H., "Laser interferometric dilatometer at low temperatures: application to fused silica SRM 739", ***Cryogenics***, Vol. 35, No. 12, (1995), 887-891. https://doi.org/10.1016/0011-2275(95)96887-R
3. Yoldas, B. E., Partlow, D. P., "Formation of broad band antireflective coatings on fused silica for high power laser applications", ***Thin Solid Films***, Vol. 129, No. 1-2, (1985), 1-14. https://doi.org/10.1016/0040-6090(85)90089-6
4. Chen, X., Liu, C., Zheng, W., Han, J., Zhang, L., Liu, C., "High strength silica-based ceramics material for investment casting applications: Effects of adding nanosized alumina coatings", ***Ceramics International***, Vol. 46, No. 1, (2020), 196-203. https://doi.org/10.1016/j.ceramint.2019.08.248
5. Cui, H., Zhong, R., Wang, X., Li, Z., Ling, Y., Yu, C., Chen, H., "Reassessment of the zircon Raman spectroscopic pressure sensor and application to pressure determination of fused silica capillary capsule", ***Ore Geology Reviews***, Vol. 122, (2020), 103540. https://doi.org/10.1016/j.oregeorev.2020.103540
6. Deng, B., Shi, Y., Yuan, F., "Investigation on the structural origin of low thermal expansion coefficient of fused silica", ***Materialia***, Vol. 12, (2020), 100752. https://doi.org/10.1016/j.mtla.2020.100752
7. Duan, W., Yang, Z., Cai, D., Zhang, J., Niu, B., Jia, D., Zhou, Y., "Effect of sintering temperature on microstructure and mechanical properties of boron nitride whisker reinforced fused silica composites", ***Ceramics International***, Vol. 46, No. 4, (2020), 5132-5140. https://doi.org/10.1016/j.ceramint.2019.10.257
8. Liu, S. H., Chen, P., Xu, D. H., Yuan, Q. D., "Effects of sintering temperature on phases, microstructures and properties of fused silica ceramics", In Bao Y., Jiang D., Gong J. (eds.), ***Key Engineering Materials, Vol. 726***, Trans Tech Publications Ltd., Switzerland, (2017), 399-403, https://doi.org/10.4028/www.scientific.net/kem.726.399
9. Romashin, A. G., Pivinskii, Y. E., "Properties of fused silica ceramics", ***Refractories***, Vol. 9, No. 9-10, (1968), 590-595. https://doi.org/10.1007/bf01283506
10. Ganesh, I., Mahajan, Y. R., "Slip-Cast Fused Silica Radomes for Hypervelocity Vehicles: Advantages, Challenges, and Fabrication Techniques", ***Handbook of Advanced Ceramics and Composites: Defense, Security, Aerospace and Energy Applications***, (2020), 251-317. https://doi.org/10.1007/978-3-319-73255-8_55-1
11. Richerson, D. W., Lee, W. E., ***Modern Ceramic Engineering: Properties, Processing, and Use in Design***, 4th ed., CRC press, Taylor & Francis Group: Boca Raton, FL, USA, (2018). https://doi.org/10.1201/9780429488245
12. Talimian, A., Galusek, D., "Aqueous slip casting of translucent magnesium aluminate spinel: Effects of dispersant concentration and solid loading", ***Ceramics International***, Vol. 45, No. 8, (2019), 10646-10653. https://doi.org/10.1016/j.ceramint.2019.02.134
13. Xu, Y., Mao, X., Fan, J., Li, X., Feng, M., Jiang, B., Lei, F., Zhang, L., "Fabrication of transparent yttria ceramics by alcoholic slip-casting", ***Ceramics International***, Vol. 43, No. 12, (2017), 8839-8844. https://doi.org/10.1016/j.ceramint.2017.04.017
14. Heaney, P. J., "Chapter 1. Structure and chemistry of the low-pressure silica polymorphs", ***Silica: Physical Behavior, Geochemistry, and Materials Applications***, Heaney, P. J., Prewitt, C. T., Gibbs, G. V. (eds.), Berlin, Boston: De Gruyter, (2018), 1-40. https://doi.org/10.1515/9781501509698-006
15. Carpenter, M. A., Salje, E. K., Graeme-Barber, A., Wruck, B., Dove, M. T., Knight, K. S., "Calibration of excess thermodynamic properties and elastic constant variations associated with the alpha ↔ beta phase transition in quartz", ***American Mineralogist***, Vol. 83, No. 1-2, (1998), 2-22. https://doi.org/10.2138/am-1998-1-201
16. Fanderlik, I. ed., ***Silica Glass and Its Application***, Elsevier, Amsterdam, The Netherlands, (2013).
17. Lakshtanov, D. L., Sinogeikin, S. V., Bass, J. D., "High-temperature phase transitions and elasticity of silica polymorphs", ***Physics and Chemistry of Minerals***, Vol. 34, No. 1, (2007), 11-22. https://doi.org/10.1007/s00269-006-0113-y
18. Dai, Y., Yin, Y., Xu, X., Jin, S., Li, Y., Harmuth, H., "Effect of the phase transformation on fracture behaviour of fused silica refractories", ***Journal of the European Ceramic Society***, Vol. 38, No. 16, (2018), 5601-5609. https://doi.org/10.1016/j.jeurceramsoc.2018.08.040
19. Niu, S. X., Cai, S., Tang, D. Z., Liu, X. G., Gu, G. H., Yao, J. S., Li, X., Wang, L. L., Fan, H. N., "Investigation on nano-fused silica in silica-based ceramic cores for investment casting", In Han, Y., Zhang, Q., Jiang, B. (eds.), ***Materials Science Forum***,

Vol. 816, Trans Tech Publications Ltd., Switzerland, (2015), 266-270. https://doi.org/10.4028/www.scientific.net/msf.816.266
20. ASTM F417-78(1996), ***Test Method for Flexural Strength (Modulus of Rupture) of Electronic-Grade Ceramics (Withdrawn 2001)***, ASTM International, West Conshohocken, PA, (1996). https://doi.org/10.1520/F0417-78R96
21. Cullity, B. D., ***Elements of X-ray Diffraction***, Addison-Wesley Publishing Company Inc., Boston, (1956). https://www.eng.uc.edu/~beaucag/Classes/XRD/elementsofxraydi030864mbp.pdf
22. Yuchang, Q., Qinlong, W., Fa, L., Wancheng, Z., "Temperature dependence of the electromagnetic properties of graphene nanosheet reinforced alumina ceramics in the X-band", ***Journal of Materials Chemistry C***, Vol. 4, No. 22, (2016), 4853-4862. https://doi.org/10.1039/C6TC01163B
23. Wan, W., Huang, C. E., Yang, J., Zeng, J., Qiu, T., "Effect of sintering temperature on the properties of fused silica ceramics prepared by gelcasting" ***Journal of Electronic Materials***, Vol. 43, No. 7, (2016), 2566-2572 (2014). https://doi.org/10.1007/s11664-014-3112-7
24. Provancher, W., Ghosh, A. K., "High Temperature Mechanical Behavior of Nb_5Si_3/Nb Laminates", ***MRS Online Proceedings Library***, Vol. 364, (1994), 1071-1076. https://doi.org/10.1557/proc-364-1071
25. Koike, C., Noguchi, R., Chihara, H., Suto, H., Ohtaka, O., Imai, Y., Matsumoto, T., Tsuchiyama, A., "Infrared spectra of silica polymorphs and the conditions of their formation", ***The Astrophysical Journal***, Vol. 778, No. 1, (2013), 60. https://doi.org/10.1088/0004-637x/778/1/60
26. Richerson, D. W., Lee, W. E., ***Modern Ceramic Engineering: Properties, Processing, and Use in Design***, 4th ed., CRC press, New York, USA, (2018). https://doi.org/10.1201/9780429488245
27. Garbarz-Glos, B., Bąk, W., Budziak, A., Dulian, P., Lisińka-Czekaj, A., Czekaj, D., "The Application of the Mechanochemical Synthesis for the Preparation of Advanced Ceramics Based on Barium Titanate", ***Archives of Metallurgy and Materials***, Vol. 65, No. 4, (2020) 1391-1396. https://doi.org/10.24425/amm.2020.133705

Advanced Ceramics Progress: Vol. 7, No. 2, (Spring 2021) 23-27

Materials and Energy Research Center
MERC

Contents lists available at ACERP

Advanced Ceramics Progress

Journal Homepage: www.acerp.ir

Technical Note Article

Preparation of High-Solid Filled Alumina Inks for Stereolithography 3D Printing Process

A. Khecho [a], S.A. Ghaffari [b] *, M. Behzadnasab [c], M. Rahmat [c]

[a] *MS, School of Metallurgy and Materials Engineering, Iran University of Science and Technology, Tehran, Tehran, Iran*
[b] *Assistant Professor, School of Metallurgy and Materials Engineering, Iran University of Science and Technology, Tehran, Tehran, Iran*
c Assistant Professor, Faculty of Polymer Processing, Iran Polymer and Petrochemical Institute, Tehran, Tehran, Iran

ARTICLE INFO

Article History:

Received 23 May 2021
Received in revised form 4 July 2021
Accepted 10 August 2021

Keywords:

Additive Manufacturing
3D Printing
DLP
Alumina
Rheology

ABSTRACT

In ceramic additive manufacturing, it is important to fabricate parts with high solid contents to guarantee defect-free sintered parts. In stereolithography, low viscosity and especially shear-thinning behavior of the ink are the key factors in producing ceramic-resin parts. Therefore, there should be a correlation between solid loading and viscosity. In this study, Alumina-glass inks were printed using bottom-up and top-down approaches, and the rheological properties were investigated. The main objective of this study was to print a highly filled ceramic-resin part with a viscosity suitable for DLP printing. While use of suspensions with low viscosity was recommended for top-down digital light processing (DLP) printing, a new setup was designed to study the feasibility of the top-down approach for pastes for the top-down approach. According to the findings, ceramic-resin pastes with the solid content of maximum 75 wt% and viscosity of 47.64 Pa.s at the shear rate of 30 s^{-1} were easily printable via our hand-made top-down DLP printer. However, it was not possible to print inks with solid contents more than 60 wt% using the bottom-up DLP, mainly because the detachment force grew dramatically with an increase in viscosity.

https://doi.org/10.30501/ACP.2021.287468.1062

1. INTRODUCTION

Additive manufacturing is best known as an alternate shaping method for ceramics that ovecomes several problems in conventional shaping methods. In additively manufactured ceramic parts, the design of molds for complex-shaped structures is rejected and often, there is no need for mechanical process for sintered ceramic parts. Moreover, additive manufacturing provides fabrication of complex geometrical shapes with high dimensional accuracy [1,2]. In stereolithography, functioning based on the photopolymerization of the resin, the ceramic parts are formed by solidifying the ceramic-resin suspension. In each layer, the suspension is exposed to UV light according to a 3D pattern and photocurbale resin is polymerized for making a solidified layer. Finally, solidified layers consistute the final ceramic-resin part. In stereolithography, there is another method for printing called digital light processing (DLP) in which the laser light source is replaced by a UV projector, and each layer is cured all at once [3–5].

Depending on the light source position, stereolithography process is categorized into two approaches. The light source can be positioned either on the top (top-down approach) or at the bottom (bottom-up approach) of the suspension vat [6]. The bottom-up

* Corresponding Author Email: amirghaffari@iust.ac.ir (S. A. Ghaffari)
URL: https://www.acerp.ir/article_136415.html

Please cite this article as: Khecho, A., Ghaffari, S. A., Behzadnasab, M., Rahmat, M., "Preparation of High-Solid Filled Alumina Inks for Stereolithography 3D Printing Process", ***Advanced Ceramics Progress***, Vol. 7, No. 2, (2021), 23-27. https://doi.org/10.30501/ACP.2021.287468.1062

approach is beneficial due to the higher resolution of the ceramic parts; however, the detachment force applied to each layer is its main disadvantage, which causes deformation and increases the possibility of removing the sample from the build plate. In top-down, there is no need for any detachment force, since the light is exposed from the top. On the contrary, the layer thickness control is one of the challenging issues in the top-down approach which highly affects the resolution of the printed parts. Therefore, for top-down DLP printers, low-viscosity suspensions are recommended [7,8]. Generally, in DLP printing, self-levelling property is of singinificance in fabricating ceramic parts with minimized defects. As reported previously, ceramic suspensions suitable for stereolithography should have viscosities about <5 Pa.s with a shear rate of 30 s^{-1} and a non-Newtonian shear-thinning behavior [9]. In sintering, however, high solid-filled parts are required to develop a part with the lowest shrinkage and deformation, simultaneously characterized by acceptable mechanical properties [10]. Generally, the minimum solid loading is recommended to be 50 vol% to avoid further problems in sintering [11–14]. High solid loadings increase the viscosities and intensify the light scattering effect, both making the stereolithography process difficult. Therefore, the rheological properties and printability should be optimized for ceramic printing. Printing pastes with high viscosities can also be a solution to the aforementioned problems [14–16].

The present study uses a simple top-down DLP printing setup and high-viscosity paste for 3D print alumina parts. The effect of alumina solid load on rheology and printability of samples is also evaluated. Moreover, the thickness of the printing layer and curing time are changed to obtain the best green strength and interlayer bonding.

2. MATERIALS AND METHODS

2.1. Ink Preparation And DLP Printing

As initial ceramic powder, Alumina-glass mixture was produced by fast-milling of 70 g α-Alumina powder (d_{90}=5 µm and 99.99% purity) and 30 g soda-lime glass frit for 10 minutes and then, sieving by 270 meshes. The printable inks were prepared by mixing Alumina-glass powder with methacrylate-based photocurbale resin (Maan Polymer), as illustrated in Table 1. In order to prepare the inks, mechanical homogenizer (10,000 rpm speed) was used for the suspensions (H50 and H60) and for the pastes (U70 and U75). The resin and ceramic powder were firstly mixed mechanically and then, they were put in ultrasonic bath for two minutes to ensure the homogeneous preparation of the paste.

The suspensions were printed using Parsa 3D bottom-up DLP Printer with Vivitek 4000 Lumen projector. To print the pastes, a hand-made top-down DLP setup was designed with a UV projector light source (365 nm wavelength), and the printing pattern was changed to a cylinder as a simple pattern so that the feasibility of the top-down approach to paste printing could be examined. The curing time and the layer thickness were considered constant for both approaches, as shown in Table 1. The schematic of DLP printer approaches is shown in Figure 1.

TABLE 1. Alumina-resin printable inks' properties

Label	Powder		Curing Time	Layer Thickness	Printing Approach
	wt%	vol%	(s)	(µm)	
H50	50	23	2.3	30	Bottom-up
H60	60	31	2.3	30	Bottom-up
U70	70	42	45	200	Top-down
U75	75	48	45	200	Top-down

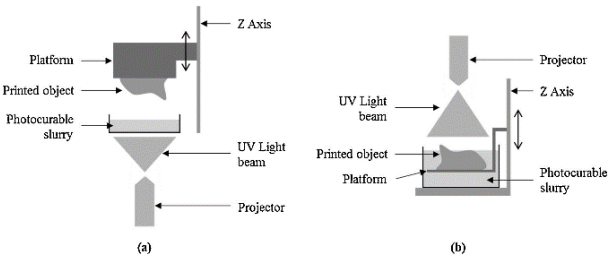

Figure 1. Schematic of DLP 3D printer approaches; a) bottom-up and b) top-down [7]

2.2. Characterization

The rheological properties of the inks were measured at room temperature using MCR301 and (Anton Parr, Austria) rheometer at shear rates of 0.1 to 1000 s^{-1}.

2.3. Sintering

Sintering was done in two steps. First, the ceramic-resin samples were heated to 400 °C at a rate of 5 °C/min and maintained for one hour for resin burn-out. Then, the samples were heated up to 1400 °C at a rate of 10 °C/min and sintered for 1.5 hours. The microstructure of the sintered samples was observed through scanning electron microscopy (Tescan, Czech Republic) images.

3. RESULTS AND DISCUSSION

3.1. Rheological Properties

Figure 2 shows the viscosity of the printable inks. Upon increasing the solid content from 50 wt% to 75 wt%, the

viscosity of the inks would significantly increase, varying from 0.52 to 47.64 Pa.s at a shear rate of 30 s^{-1}. In addion, upon increasing the solid content to 70 wt%, the pastes exhibited different behaviors at low and high shear rates. In H50 and H60, the viscosity of suspensions gradually decreased with an increase in the shear rate, exhibiting a shear-thinning behavior. Viscosity would also decrease due to the presence of agglomerates, broken down by the shear stress, thus allowing the suspension to flow. Further, as observed, the shear-thinning behavior was attentuated and the viscosity became more stable as the shear rate increased, indicating the reconstruction of the suspension structures damaged at lower shear rates. However, H60 as the more viscose suspension has a viscosity of 1.45 Pa.s at a shear rate of 30 s^{-1}, characterized by suitable rheological behavior and acceptable viscosity for DLP printing [9,17,18].

For pastes, U70 and U75 exhibit shear-thickening behavior at low shear rates due to high solid loading and steric repulsion of the Alumina particles. In other words, the particls formed a 3D structure in which the paste resisted flowing. Of note, the rheological behavior changes to shear-thinning beahavior as the shear rate increases. This can be attributed to the destruction of the 3D structures. In fact, the newly formed 2D structures increase the flowability as the shear rate increases [19].

As observed in both pastes, the viscosity dropped down drastically at a shear rate of 100 s^{-1}. In other words, the paste is formed at this shear rate, thus helping a paddle spread the viscose paste by applying an appropriate force easily to form new layer. When removing the force, an increase in viscosity makes the layer stand still during the photocuring [8,15,20].

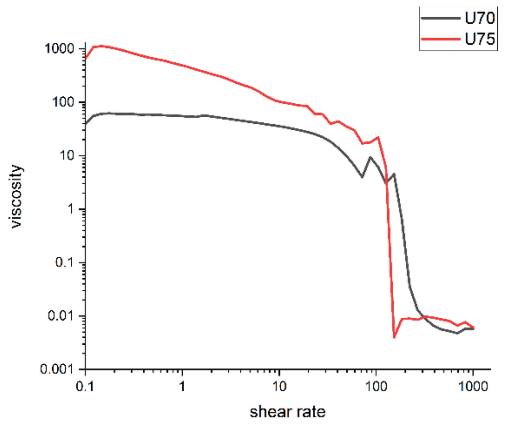

Figure 2. Viscosity variations of the inks; H50 and H60 exhibiting shear-thininng behavior, U70 and U75 showing shear-thickening and shear-thining behavior at low and high shear rates, respectively

3.2. DLP Printing

Figure 3a shows the H50 and H60 printed samples using the bottom-up DLP approach. In this approach, however, adhesion of the first layer was the main difficulty. As shown in Figure 3, H50 and H60 suspensions were printed with relatively high dimensional accuracy and layer thickness of 30 µm. It was not possible to print inks containing solid contents more than 60 wt% as the viscosity increased and exceeded the recommended viscosity range for DLP printing [21] (see Figure 2). Consequently, high viscosity and weakened self-flowing ability of the pastes made the bottom-up DLP process almost impossible due to the high detachment force required for each layer. The bottom-up DLP enjoys many advantages such as flexibility in layer thickness, high resolution, and surface quality, hence no detachment force is required. On the contrary, the top-down DLP is an interesting approach used in DLP printer [7,22]. In addition, in the top-down approach, the application of low viscosity suspension is recommended due to the difficulties in thickness control and spreading thin layers, hence making it a time-consuming process [8]. In the present study, printing of the pastes was made possible by applying the top-down DLP approach. In other words, the top-down setup designed in this study was totally appropriate for the printing pastes. Figure 3b shows the samples printed by the top-down approach. Accordingly, U70 and U75 Alumina-glass pastes were printed with an optimized layer thickness of 200 µm using this approach. By applying the top-down approach, the thickness of this layer increased up to 200 µm while maintaining acceptable dimensional accuracy. The thickness of this layer is significantly greater in value than that in studies that have previously targeted top-down approaches and printing pastes with high solid loadings [15,23,24].

In addition, the curing time reached 45 s since in the top-down approach, the photosensitive paste is directly in contact with oxygen which delays the photopolymerization [7]. In fact, besides the advantage of high solid print in the top-down approach, higher exposure time and lack of constant layer thickness are referred to as disadvantages, which reduce the printing accuracy and increase the printing duration, respectively. Moreover, it is mentioned that in the top-down approach, much more amount of ink is usually needed than that in the bottom-up approach [6,7]; however, the setup designed in this study requires a small amount of ink preparation. About five g of paste is printed on a cylinder with a diameter of about 1.4 mm and height of 5 mm, as shown in Figure 3. Hence, the material waste is minimized.

According to the findings, in case the powder amount increases to more than 75 wt%, the powder and resin do not mix well and the excess powder will remain unmixed and agglomerated, which indicates a saturation point in 75 wt% solid content for the methacrylate-based resin used in this work. This amount of solid content is equal to 48 vol%, which can be considered an acceptable solid load for sintering to obtain fully dense parts [4,25].

Therefore, the top-down approach to DLP printing can be employed as a method for developing high-filled ceramic-resin composites.

3.3. Sintering

The printed samples containing 70 and 75 wt% Alumina-resin, with the highest solid loadings, were sintered at 1400 °C. Figure 4 shows the microstructure of the 70 wt% sample. As expected, due to the existence of glass powder in the composition and high solid content, the sample with 75 wt% was fully densified at 1400 °C, resulting in 97% relative density, 2% open porosity, and 1.3% shrinkage.

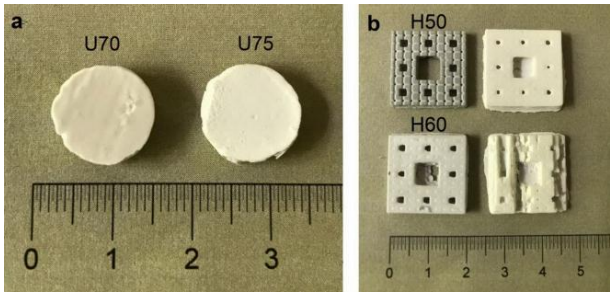

Figure 3. Printed samples via a) top-down and b) bottom-up approaches

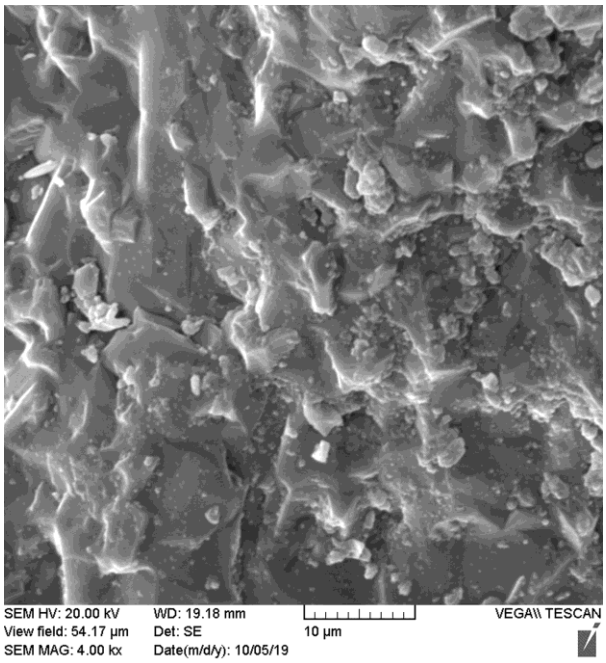

Figure 4. Cross-sectional SEM image of 70 wt% sample printed via top-down approach and sintered at 1400 °C

4. CONCLUSION

In this study, investigation of solid content and its effect on rheology indicated that the bottom-up DLP printer was suitable for the printing of the Alumina-glass suspensions containing maximum 60 wt% solid. As the solid content increased and the suspensions were converted to pastes, the bottom-up DLP printing was not doable since the detachment force highly increased. However, by employing our hand-made top-down DLP setup, the high-solid loading pastes were printable. Despite the recommendations about low viscosity in top-down approach, we were able to print highly-filled Alumina-glass samples with acceptable dimensional accuracy and high layer thickness and without any material waste.

ACKNOWLEDGEMENTS

The authors thank colleagues from Iran Polymer and Petrochemical Institute for their collaboration and their great assistance in this research.

REFERENCES

1. Wu, Z., Liu, W., Wu, H., Huang, R., He, R., Jiang, Q., Chen, Y., Ji, X., Tian, Z., Wu, S., "Research into the mechanical properties, sintering mechanism and microstructure evolution of Al_2O_3-ZrO_2 composites fabricated by a stereolithography-based 3D printing method", ***Materials Chemistry and Physics***, Vol. 207, (2018), 1–10. https://doi.org/10.1016/j.matchemphys.2017.12.021
2. He, R., Liu, W., Wu, Z., An, D., Huang, M., Wu, H., Jiang, Q., Ji, X., Wu, S. Xie, Z., "Fabrication of complex-shaped zirconia ceramic parts via a DLP-stereolithography-based 3D printing method", ***Ceramics International***, Vol. 44, No. 3, (2018), 3412–3416. https://doi.org/10.1016/j.ceramint.2017.11.135
3. Wu, H., Liu, W., He, R., Wu, Z., Jiang, Q., Song, X., Chen, Y., Cheng, L., Wu, S., "Fabrication of dense zirconia-toughened alumina ceramics through a stereolithography-based additive manufacturing", ***Ceramics International***, Vol. 43, No. 1, (2017), 968–972. https://doi.org/10.1016/j.ceramint.2016.10.027
4. Schmidt, J., Elsayed, H., Bernardo, E., Colombo, P., "Digital light processing of wollastonite-diopside glass-ceramic complex structures", ***Journal of the European Ceramic Society***, Vol. 38, No. 13, (2018), 4580–4584. https://doi.org/10.1016/j.jeurceramsoc.2018.06.004
5. Johansson, E., Lidström, O., Johansson, J., Lyckfeldt, O., Adolfsson, E., "Influence of resin composition on the defect formation in alumina manufactured by stereolithography", ***Materials***, Vol. 10, No. 2, (2017), 138. https://doi.org/10.3390/ma10020138
6. Zakeri, S., Vippola, M., Levänen, E., "A comprehensive review of the photopolymerization of ceramic resins used in stereolithography", ***Additive Manufacturing***, Vol. 35, (2020), 101177. https://doi.org/10.1016/j.addma.2020.101177
7. Santoliquido, O., Colombo, P., Ortona, A., "Additive Manufacturing of ceramic components by Digital Light Processing: A comparison between the "bottom-up" and the "top-down" approaches", ***Journal of the European Ceramic Society***, Vol. 39, No. 6, (2019), 2140–2148. https://doi.org/10.1016/j.jeurceramsoc.2019.01.044
8. Bártolo, P. J., Ed., ***Stereolithography: Materials, Processes and Applications***, Springer Science & Business Media, New York, (2011). https://doi.org/10.1007/978-0-387-92904-0

9. Zhang, S., Sha, N., Zhao, Z., "Surface modification of α-Al_2O_3 with dicarboxylic acids for the preparation of UV-curable ceramic suspensions", ***Journal of the European Ceramic Society***, Vol. 37, No. 4, (2017), 1607–1616. https://doi.org/10.1016/j.jeurceramsoc.2016.12.013
10. Li, H., Liu, Y., Liu, Y., Zeng, Q., Wang, J., Hu, K., Lu, Z., Liang, J., "Evolution of the microstructure and mechanical properties of stereolithography formed alumina cores sintered in vacuum", ***Journal of the European Ceramic Society***, Vol. 40, No. 14, (2020), 4825-4836. https://doi.org/10.1016/j.jeurceramsoc.2019.11.047
11. Gentry, S. P., Halloran, J. W., "Light scattering in absorbing ceramic suspensions: Effect on the width and depth of photopolymerized features", ***Journal of the European Ceramic Society***, Vol. 35, No. 6, (2015), 1895–1904. https://doi.org/10.1016/j.jeurceramsoc.2014.12.006
12. Hu, K., Wei, Y., Lu, Z., Wan, L., Li, P., "Design of a Shaping System for Stereolithography with High Solid Loading Ceramic Suspensions", ***3D Printing and Additive Manufacturing***, Vol. 5, No. 4, (2018), 311–318. https://doi.org/10.1089/3dp.2017.0065
13. Chartier, T., Dupas, C., Lasgorceix, M., Brie, J., Delhote, N., Chaput, C., "Additive manufacturing to produce complex 3D ceramic parts", ***Journal of Ceramic Science and Technology***, Vol. 6, No. 2, (2015), 95–104. https://doi.org/10.4416/JCST2014-00040
14. Dehurtevent, M., Robberecht, L., Hornez, J. C., Thuault, A., Deveaux, E., Béhin, P., "Stereolithography: A new method for processing dental ceramics by additive computer-aided manufacturing", ***Dental Material***, Vol. 33, No. 5, (2017), 477–485. https://doi.org/10.1016/J.DENTAL.2017.01.018
15. Liu, W., Li, M., Nie, J., Wang, C., Li, W., Xing, Z., "Synergy of solid loading and printability of ceramic paste for optimized properties of alumina via stereolithography-based 3D printing", ***Journal of Materials Research and Technology***, Vol. 9, No. 5, (2020), 11476–11483. https://doi.org/10.1016/j.jmrt.2020.08.038
16. Wu, H., Cheng, Y., Liu, W., He, R., Zhou, M., Wu, S., Song, X., Chen, Y., "Effect of the particle size and the debinding process on the density of alumina ceramics fabricated by 3D printing based on stereolithography", ***Ceramics International***, Vol. 42, No. 15, (2016), 17290–17294. https://doi.org/10.1016/j.ceramint.2016.08.024
17. Griffith, M. L., Halloran, J. W. H., "Freeform fabrication of ceramics via stereolithography", ***Journal of the American Ceramic Society***, Vol. 79, No. 10, (1996), 2601–2608. https://doi.org/10.1111/j.1151-2916.1996.tb09022.x
18. Nie, J., Li, M., Liu, W., Li, W., Xing, Z., "The role of plasticizer in optimizing the rheological behavior of ceramic pastes intended for stereolithography-based additive manufacturing", ***Journal of the European Ceramic Society***, Vol. 41, No. 1, (2021), 646–654. https://doi.org/10.1016/j.jeurceramsoc.2020.08.013
19. Zhang, K., Xie, C., Wang, G., He, R., Ding, G., Wang, M., Dai, D., Fang, D., "High solid loading, low viscosity photosensitive Al_2O_3 slurry for stereolithography based additive manufacturing", ***Ceramics International***, Vol. 45, No. 1, (2019), 203–208. https://doi.org/10.1016/j.ceramint.2018.09.152
20. de Camargo, I. L., Morais, M. M., Fortulan, C. A., Branciforti, M. C., "A review on the rheological behavior and formulations of ceramic suspensions for vat photopolymerization", ***Ceramics International***, Vol. 47, No. 9, (2021), 11906–11921. https://doi.org/10.1016/j.ceramint.2021.01.031
21. Chen, Z., Li, J., Liu, C., Liu, Y., Zhu, J., Lao, C., "Preparation of high solid loading and low viscosity ceramic slurries for photopolymerization-based 3D printing", ***Ceramics International***, Vol. 45, No. 9, (2019), 11549–11557. https://doi.org/10.1016/j.ceramint.2019.03.024
22. Taormina, G., Sciancalepore, C., Messori, M., Bondioli, F., "3D printing processes for photocurable polymeric materials: technologies, materials, and future trends", ***Journal of Applied Biomaterials & Functional Materials***, Vol. 16, No. 3, (2018), 151–160. https://doi.org/10.1177/2280800018764770
23. Hu, C., Chen, Y., Liu, H., Huang, X., Huo, Y., Jia, Z., Wang, H., Hu, L., Sun, H., Wang, C., "Effect of SiC powder on the properties of SiC Slurry for Stereolithography", ***Ceramics International***, Vol. 47, No. 9, (2021), 12442–12449. https://doi.org/10.1016/j.ceramint.2021.01.101
24. Liu, C., Qian, B., Liu, X., Tong, L., Qiu, J., "Additive manufacturing of silica glass using laser stereolithography with a top-down approach and fast debinding", ***RSC Advances***, Vol. 8, No. 29, (2018), 16344–16348. https://doi.org/10.1039/C8RA02428F
25. Li, K., Zhao, Z., "The effect of the surfactants on the formulation of UV-curable SLA alumina suspension", ***Ceramics International***, Vol. 43, No. 6, (2017), 4761–4767. https://doi.org/10.1016/j.ceramint.2016.11.143

Advanced Ceramics Progress: Vol. 7, No. 2, (Spring 2021) 28-33

Materials and Energy Research Center
MERC

Contents lists available at ACERP

Advanced Ceramics Progress

Journal Homepage: www.acerp.ir

Original Research Article

Two-Dimensional Physical and Numerical Modelling of Copper (II)-Oxide/Silicon Hetero Junction Bipolar Transistor

M. Yousefizad [a], S. Hooshmand [a], M. M. Ghezel-Ayagh [a], F. Raissi [b] *

[a] *MS, Department of Electrical Engineering, K. N. Toosi University of Technology, Tehran, Tehran, Iran*
[b] *Professor, Department of Electrical Engineering, K. N. Toosi University of Technology, Tehran, Tehran, Iran*

ARTICLE INFO

Article History:

Received 7 July 2021
Received in revised form 30 August 2021
Accepted 5 September 2021

Keywords:

Flexible and Printed Electronics
Ion-Implantation
Double Heterojunction Bipolar Transistor
Simulation
low-Temperature Deposition
Copper Oxide
SILVACO

ABSTRACT

Flexible and printed electronics have been widely applied due to their low cost, scalability in manufacturing, and usability in biosensors as well as wearable electronics. However, there are some limitations on fabrication of these devices including thermal limitations. Thermal constraints are of significance since ion implantation at high temperatures is one of the most important stages of fabrication; therefore, despite these limitations, fabrication of flexible BJT is practically impossible through conventional methods. In this study, copper oxide was used for the collector and emitter area of Double Heterojunction Bipolar Transistor (DHBT) due to the low-temperature deposition of copper oxide through the printing method, and the ability to adjust the doping according to the deposition conditions. DC and high-frequency specifications of two transistors with PNP and NPN structures were simulated using two-dimensional semiconductor simulator atlas module of SILVACO software.

https://doi.org/10.30501/acp.2021.293952.1069

1. INTRODUCTION

Flexible and printed electronics are of great importance in manufacturing and development of wearable devices [1-6], large solar cells [7-11], touch screens [12-13], and implantable circuits [14-15]. Several characteristics of these electronics have led to their development and wide applicability such as their ability to bend, non-breakable features, manufacturable roll-to-roll, and a large area. In printed and flexible electronics, transistor fabrication methods mostly require some steps such as different dopant introduction as well as annealing steps; these steps are not compatible with flexible and organic substrates [16-17], which may damage the organic substrate and negatively affect the device performance. In this regard, semiconductor metal oxides were employed to remove the ion implantation step and combine it with the deposition step. Among semiconductor metal oxides, copper oxide can be a good candidate for transistor fabrication. Copper oxide has some features such as low price, abundance in nature, easy deposition, and relatively large bandgap [18-23]. Among all of these features, the most important ones, which are also the main focus of this study, are the tunability of the bandgap and doping of impurities due to deposition condition [24,25]; these two factors can be

* Corresponding Author Email: raissi@eetd.kntu.ac.ir (F. Raissi)
URL: https://www.acerp.ir/article_136417.html

Please cite this article as: Yousefizad, M., Hooshmand, S., Ghezel-Ayagh, M. M., Raissi, F., "Two-Dimensional Physical and Numerical Modelling of Copper (II)-Oxide/Silicon Hetero Junction Bipolar Transistor", ***Advanced Ceramics Progress***, Vol. 7, No. 2, (2021) 28-33. https://doi.org/10.30501/acp.2021.293952.1069

adjusted during the deposition of copper oxide. So far, many copper oxide-based flexible transistors have been introduced that were of TFT type with a copper oxide channel [26-32]. Through the incorporation of copper oxide-based HBTs to flexible electronic circuits, the resultant material can be widely applied in wearable electronics, medical implants, and medical diagnostics.

The main objective of the present study was to investigate two different PNP and NPN structures based on CuO/Si heterojunction, simulate them based on the reported properties, and evaluate and compare the results of high-frequency and DC analysis of these two HBTs.

2. DEVICE STRUCTURES

In p-CuO/n-Si/p-CuO Heterojunction Bipolar Transistor (HBT), labeled as Device A, the structure layers consist of three layers including 0.1 µm, $p^+ = 10^{19}$ cm^{-3} CuO emitter layer; 0.1 µm, $n^+ = 10^{19}$ cm^{-3} Si base layer; and 0.8 µm, $p^+ = 10^{19}$ cm^{-3} CuO collector layer. Similar to the above structure, for NPN HBT, the structure layers consist of 0.1 µm, $n^+ = 10^{19}$ cm^{-3} CuO emitter layer; 0.1 µm, $p^+ = 10^{19}$ cm^{-3} Si base layer; 0.8 µm, $n^+ = 10^{19}$ cm^{-3} CuO collector layer, which is labeled as Device B. The dimensions of the areas of the emitter and collector areas are 0.1×0.8 and 2×0.8 μm^2, respectively. Also the semiconductor parameters were simulated based on the data detailed in Table 1.

TABLE 1. Parameters of CuO, Cu_2O and Si [25]

Parameter	CuO	Cu_2O	Si
Hole Mobility (cm^2/Vs)	5	80	≤450
Band Gap Energy (eV)	1.5	2.3	1.12
Electron Affinity (eV)	4.07	3.2	4.05
VB Effective Density of State (cm^{-3})	5×10^{18}	1.1×10^{19}	1.83×10^{19}
CB Effective Density of State (cm^{-3})	3×10^{19}	2.02×10^{17}	2.82×10^{19}
Carrier Lifetime (s)	212×10^{-12}	10^{-9}	10^{-7}
Dielectric Relative Permittivity	18.1	7.11	11.8

A two-dimensional semiconductor simulation package SILVACO was employed to analyze the energy band diagrams, carrier distributions, dc, and high-frequency performance. The simulated analysis takes into account Poisson's equation, continuity equation of electrons and holes, Shockley–Read–Hall (SRH) recombination, bandgap narrowing (BGN), Auger recombination, Concentration Dependent (CONMOB), Parallel Electric Field Dependence (FLDMOB), and Boltzmann statistics.

The schematic drawing of the device simulated is shown in Figure 1.

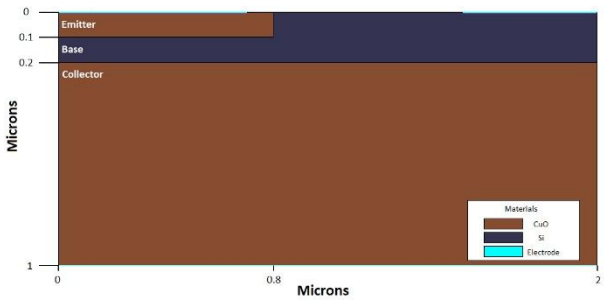

Figure 1. Schematic diagram of the simulated device

3. RESULTS AND DISCUSSION

3.1. Device A (PNP Structure)

The diagram of the energy band in the thermal equilibrium mode of device A is shown in Figure 2.

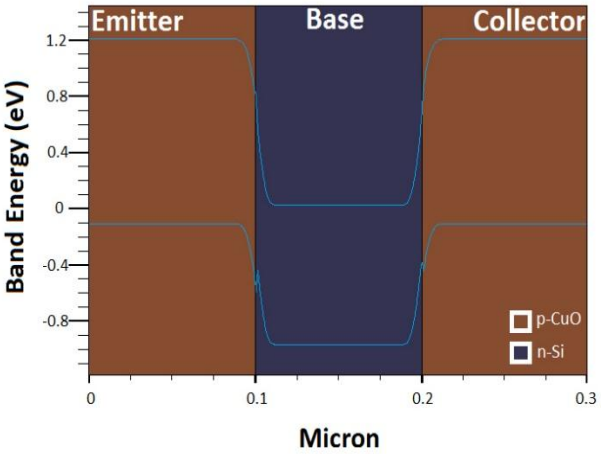

Figure 2. Energy band diagram of device A in the thermal equilibrium mode

The valence bands of the B-E and B-C junctions of the device A have spike potentials of 0.16 eV and 0.08 eV, respectively. One of the major problems with Heterojunction Bipolar Transistors (HBTs) is the presence of spike potential at the junctions and in their valence and conduction bands. Spike potential increases the turn-on voltage at the B-E and B-C junctions, resulting in offset voltage [33]. However, in DHBTs studied in this paper, due to the use of silicon copper-oxide bonds, compared to other HBTs, it has less spike potential.

$\alpha_0 = I_{CP}/I_E$

$$\alpha_0 = I_{Cp} / I_{Ep}+I_{En} = (I_{Ep} / (I_{Ep}+I_{En})) (I_{CP} / I_{Ep}) \quad (1)$$

The first part of the equation is called the efficiency of the emitter, which is actually the ratio of the injected holes to the total current of the emitter. For an ideal design, we want the efficiency of the emitter to be close to one; thus, I_{En} must be about zero.

The conduction band potential barrier prevents the injection of electrons from the base into the emitter. According to Equation (1), this is the main reason for the efficiency of the emitter and, as a result, the increase in current gain.

The collector current according to the collector voltage diagram of device A is shown in Figure 3. The turn-on voltage is 0.23 V.

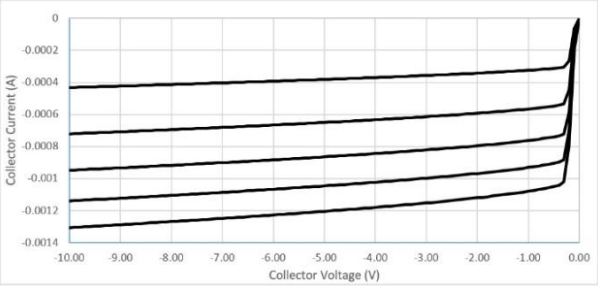

Figure 3. Current-voltage characteristic of the common bias emitter of device A with the base current step being 1 µA from zero

Figure 4 shows the zoomed image of the current-voltage characteristic in the common-emitter bias of the device A. The offset voltage is defined as the voltage that must be applied at the input to make the output zero. The offset voltage obtained for the base voltage of a microampere for this device is 9 mV. In general, the offset voltage in HBTs is due to the difference in the turn-on voltage between the B-E junction and the B-C junction. The higher the spike potential within the valance band of the device A, the higher the turn-on voltage will be. Using the quasi-symmetrical structure, the offset voltage problem in HBTs can be solved to some extent, the cause of which is discussed below. According to the diagram of the drawn energy band (Figure 2) for device A, there will be a spike potential in the valance band on both B-E and B-C junctions, thus increasing the turn-on voltage in both heterojunction bonds. However, the total offset voltage of the transistor which is the result of the potential difference between the B-E and B-C junctions is still small.

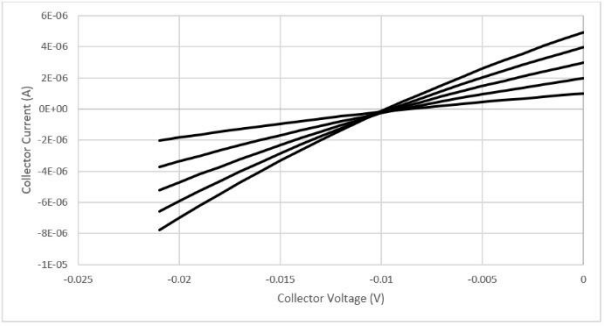

Figure 4. Zooming image of the current-voltage characteristic in the common bias emitter of device A, with the base current step being 1µA from zero

The electrical characteristics of the base current and the collector current as a function of forwarding bias are referred to as the Gummel plot, The Gummel plot of device A for collector currents and base currents is plotted according to Figure 5. The current amplification factor of device A is around 227 at base voltage of 0.7 V, and the ideality factor of diode according to base voltage of 0.7 V for collector current is 1.01 and for base current is 1.5, which indicates the predominance of diffusion and thermionic mechanisms of carrier motion. Also, according to the Gummel plot, when the base-emitter voltage is 0.7 V, the base recombination current does not prevail, thus reducing the ideal factor of diode of base current.

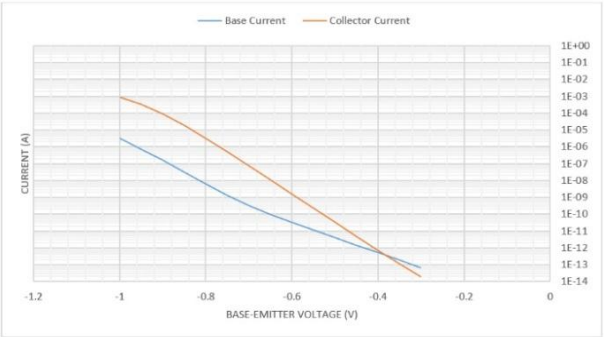

Figure 5. The Gummel plot for base and collector currents of device A while V_{CE} = -2 V

Figure 6 shows the relationship between current gain and operating frequency of device A. The unity gain cut-off frequency ft for this device is 10 GHz for VCE = 1 V. Figure 6 shows the AC gain of device A equal to 44 dB.

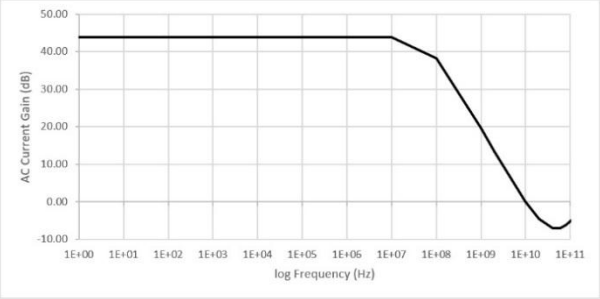

Figure 6. Current gain cut-off frequency (ft) of device A

3.2. Device B (NPN structure)

Now, in order to increase the gain of device A, device B is examined. In device B, the potential barrier of a majority of carriers in the base is greater and as a result, the gain is promoted.

The energy band diagram in thermal equilibrium is shown in Figure 7. Device B in its base-emitter junction conduction band has a spike potential of 0.04 eV, which is a very small value. Spike potential in the conduction band of the base-collector junction area is not given in Figure 7. Without the use of spike reduction techniques such as adding layers of different semiconductors between base-emitter and base-collector, these values are obtained which reduce the cost of manufacturing this transistor. Because the forbidden band of the emitter is larger than the base, a barrier is created in device B that prevents the entry of injection holes from the base to the emitter, thus increasing the current gain.

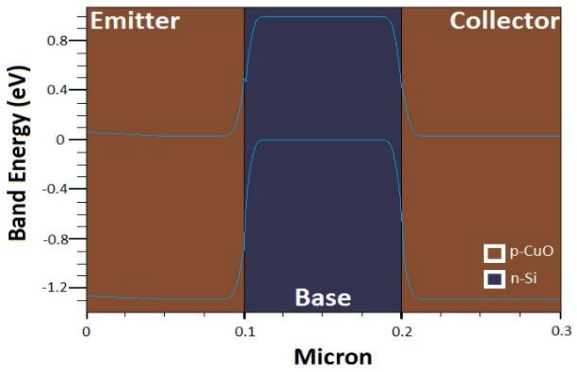

Figure 7. Energy band diagram of device B in thermal equilibrium.

The characteristic curve of the collector current according to the collector voltage of device B is shown in Figure 8. VBCEO = 5.8 V and the current base scale is one µA. The turn-on voltage for device B is 0.28 V according to Figure 8.

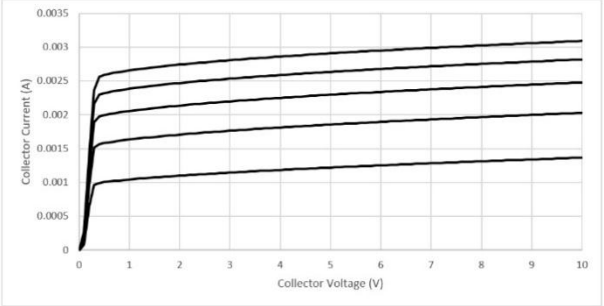

Figure 8. Voltage-current characteristic curve in the common bias emitter of device B, with the base current step being 1µA from zero

Figure 9 shows the zoomed image of the voltage-current characteristic curve of the common-emitter of the B device. The offset voltage obtained according to the base voltage of 1 µA for this device is 9 mV. In general, the offset voltage in HBTs is due to the difference in the turn-on voltage of B-E and B-C junctions.

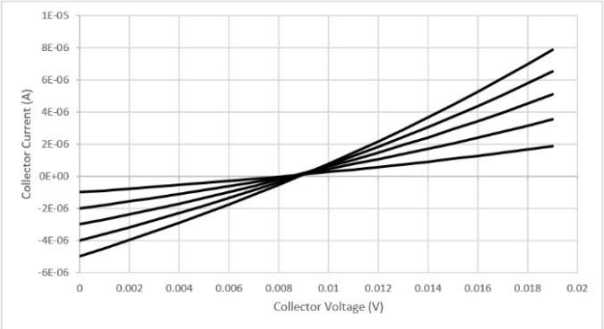

Figure 9. Zoomed image of Voltage-current characteristic curve in the common bias emitter of the device B, with the base current step being 1µA from zero.

The Gummel plot of device B for collector current and base current is plotted according to Figure 10. The current amplification factor of device B is around 578 at base voltage of 0.7 V, and the ideality factor of diode according to base voltage of 0.7 V for collector current is 1.01 and for base current is 1.33, which indicates the predominance of diffusion and Thermionic mechanisms of carrier motion. Also, according to the Gummel plot, when the base-emitter voltage is 0.7 V, the base recombination current does not prevail, thus reducing the ideality factor of base emitter diode.

Figure 11 shows the relationship between current gain and operating frequency of device B. The unity gain cut-off frequency ft for this device is 10 GHz for VCE = 1 V. Figure 11 shows the AC gain of device B, which is equal to 60.5 dB.

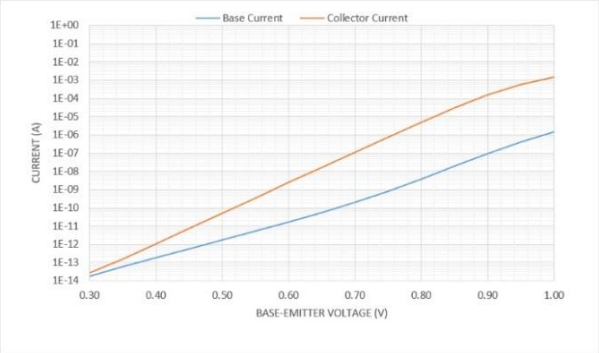

Figure 10. The Gummel plot for base and collector currents of device B while VCE=2V

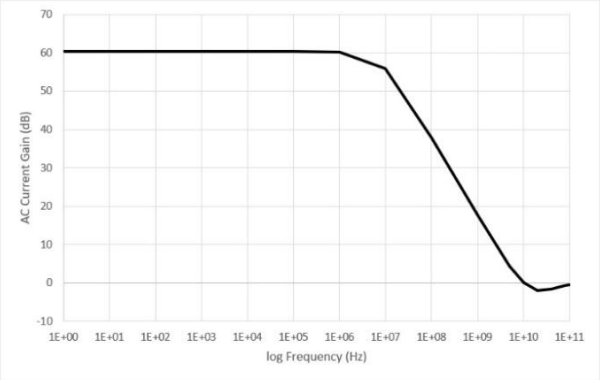

Figure 11. Current gain cut off frequency (ft) of device B

4. CONCLUSION

The physical model of two heterojunction bipolar transistors based on CuO/Si junction with PNP and NPN structures was investigated. Successful simulations of two HBTs using copper oxide semiconductors as emitter and collector regions and silicon for the base layer with excellent properties were presented and a high current gain factor was exhibited. The simulation results showed that there was a small spike potential in the base-emitter junction of both structures, which reduced the offset voltage of both transistors. The offset voltage obtained from these structures was acceptable even without the use of the emitter-base junction grading technique. This feature makes the use of this type of transistor in switching and driver circuits also applicable. In Device B, due to the presence of a potential barrier in the valance band, the base holes are prevented from entering the emitter, thus increasing the emitting efficiency and the DC and high-frequency current amplification. Given the existence of different methods of copper oxide deposition, there are different optical and electrical ranges such as energy band gap and density of carriers that can be researched to obtain the best electrical properties for different applications of bipolar transistors. Consequently, these structures can provide a wide range of applications in flexible circuits.

ACKNOWLEDGEMENTS

We would like to thank Dr. Negin Manavizadeh, our colleague who provided the insight and motivation that contributed to this research.

REFERENCES

1. Gupta, S., Navaraj, W. T., Lorenzelli, L., Dahiya, R., "Ultra-thin chips for high-performance flexible electronics", ***NPJ Flexible Electronics***, Vol. 2, No. 1, (2018), 1-17. https://doi.org/10.1038/s41528-018-0021-5
2. Kim, B. J., Kim, D. H., Lee, Y. Y., Shin, H. W., Han, G. S., Hong, J. S., Mahmood, K., Ahn, T. K., Joo, Y. C., Hong, K. S., Park, N. G., "Highly efficient and bending durable perovskite solar cells: toward a wearable power source", ***Energy & Environmental Science***, Vol. 8, No. 3, (2015), 916-921. https://doi.org/10.1039/C4EE02441A
3. Siddik, A., Haldar, P. K., Garu, P., Bhattacharjee, S., Das, U., Barman, A., Roy, A., Sarkar, P. K., "Enhancement of data storage capability in a bilayer oxide-based memristor for wearable electronic applications", ***Journal of Physics D: Applied Physics***, Vol. 53, No. 29, (2020), 295103. https://doi.org/10.1088/1361-6463/ab81d3
4. Matsuhisa, N., Kaltenbrunner, M., Yokota, T., Jinno, H., Kuribara, K., Sekitani, T., Someya, T., "Printable elastic conductors with a high conductivity for electronic textile applications", ***Nature Communications***, Vol. 6, No. 1, (2015), 1-11. https://doi.org/10.1038/ncomms8461
5. Lv, J., Thangavel, G., Li, Y., Xiong, J., Gao, D., Ciou, J., Tan, M. W. M., Aziz, I., Chen, S., Chen, J., Zhou, X., "Printable elastomeric electrodes with sweat-enhanced conductivity for wearables", ***Science Advances***, Vol. 7, No. 29, (2021), p.eabg8433. https://doi.org/10.1126/sciadv.abg8433
6. Na, J. W., Kim, H. J., Hong, S., Kim, H. J., "Plasma polymerization enabled polymer/metal–oxide hybrid semiconductors for wearable electronics", ***ACS Applied Materials & Interfaces***, Vol. 10, No. 43, (2018), 37207-37215. https://doi.org/10.1021/acsami.8b11094
7. Peng, C. Y., Dhakal, T. P., Garner, S., Cimo, P., Lu, S., Westgate, C. R., "Fabrication of Cu_2ZnSnS_4 solar cell on a flexible glass substrate", ***Thin Solid Films***, Vol. 562, (2014), 574-577. https://doi.org/10.1016/j.tsf.2014.03.054
8. Li, K., Zhen, H., Niu, L., Fang, X., Zhang, Y., Guo, R., Yu, Y., Yan, F., Li, H., Zheng, Z., "Full-solution processed flexible organic solar cells using low-cost printable copper electrodes", ***Advanced Materials***, Vol. 26, No. 42, (2014), 7271-7278. https://doi.org/10.1002/adma.201403494
9. Sultana, J., Paul, S., Saha, R., Sikdar, S., Karmakar, A., Chattopadhyay, S., "Optical and electronic properties of chemical bath deposited p-CuO and n-ZnO nanowires on silicon substrates: p-CuO/n-ZnO nanowires solar cells with high open-circuit voltage and short-circuit current", ***Thin Solid Films***, Vol. 699, (2020), 137861. https://doi.org/10.1016/j.tsf.2020.137861
10. Xu, Q., Wang, F., Tan, Z. A., Li, L., Li, S., Hou, X., Sun, G., Tu, X., Hou, J., Li, Y., "High-performance polymer solar cells with solution-processed and environmentally friendly CuO_x anode

buffer layer", ***ACS Applied Materials & Interfaces***, Vol. 5, No. 21, (2013), 10658-10664. https://doi.org/10.1021/am402745t

11. Yarmand, B., "Effects of particles size distribution and occupied area of CdS photosensitizer on photovoltaic performance", ***Advanced Ceramics Progress***, Vol. 2, No. 4, (2016), 7-12. https://dx.doi.org/10.30501/acp.2016.70037
12. Fan, W., Lok, B. K., Lai, F. K., Wei, J., "Evaluation of printed capacitive touch sensors for touch panel", In ***2017 IEEE 19th Electronics Packaging Technology Conference, (EPTC)***, (2017), 1-4. https://doi.org/10.1109/EPTC.2017.8277586
13. Anisimov, A. S., Brown, D. P., Mikladal, B. F., Súilleabháin, L. Ó., Parikh, K., Soininen, E., Sonninen, M., Tian, D., Varjos, I., Vuohelainen, R., "16.3: Printed Touch Sensors Using Carbon NanoBud® Material", In ***Sid Symposium Digest of Technical Papers***, Vol. 45, No. 1, (2014), 200-203. https://doi.org/10.1002/j.2168-0159.2014.tb00055.x
14. Núñez, C. G., Manjakkal, L., Dahiya, R., "Energy autonomous electronic skin", ***NPJ Flexible Electronics***, Vol. 3, No. 1, (2019), 1-24. https://doi.org/10.1038/s41528-018-0045-x
15. Han, W. B., Lee, J. H., Shin, J. W., Hwang, S. W., "Advanced materials and systems for biodegradable, transient electronics", ***Advanced Materials***, Vol. 32, No. 51, (2020), 2002211. https://doi.org/10.1002/adma.202002211
16. Yamauchi, N., Reif, R., "Polycrystalline silicon thin films processed with silicon ion implantation and subsequent solid-phase crystallization: Theory, experiments, and thin-film transistor applications", ***Journal of Applied Physics***, 75, No. 7, (1994), 3235-3257. https://doi.org/10.1063/1.356131
17. Williams, J. S., "Ion implantation of semiconductors", ***Materials Science and Engineering: A***, Vol. 253, No. 1-2, (1998), 8-15. https://doi.org/10.1016/S0921-5093(98)00705-9
18. Wang, Y., Ghanbaja, J., Soldera, F., Migot, S., Boulet, P., Horwat, D., Mücklich, F., Pierson, J. F., "Tuning the structure and preferred orientation in reactively sputtered copper oxide thin films", ***Applied Surface Science***, Vol. 335, (2015), 85-91. https://doi.org/10.1016/j.apsusc.2015.02.028
19. Asl, H. Z., Rozati, S. M., "Spray deposition of n-type cobalt-doped CuO thin films: influence of cobalt doping on structural, morphological, electrical, and optical properties", ***Journal of Electronic Materials***, Vol. 49, No. 2, (2020), 1534-1540. https://doi.org/10.1007/s11664-019-07858-4
20. Rahimi, N., Dalouji, V., Souri, A., "Studying the Optical Density, Topography, and Structural Properties of CZO and CAZO Thin Films at Different Annealing Temperatures", ***Advanced Ceramics Progress***, Vol. 6, No. 2, (2020), 17-23. https://doi.org/10.30501/ACP.2020.107466
21. Abramova, A. N., Dorogov, M. V., Vlassov, S., Kink, I., Dorogin, L. M., Lõhmus, R., Romanov, A. E., Vikarchuk, A. A., "Nanowhisker of copper oxide: fabrication technique, structural features and mechanical properties", ***Materials Physics and Mechanics***, Vol. 32, No. 1, (2014), 88-95. https://mpm.spbstu.ru/userfiles/files/MPM119_08_abramova.pdf
22. Zeng, X., Zhukova, M., Faniel, S., Proost, J., Flandre, D., "Structural and Opto-electronic characterization of CuO thin films prepared by DC reactive magnetron sputtering", ***Journal of Materials Science: Materials in Electronics***, Vol. 31, No. 6, (2020), 4563-4573. https://doi.org/10.1007/s10854-020-03007-4
23. Živković, A., de Leeuw, N. H., "Exploring the formation of intrinsic p-type and n-type defects in CuO", ***Physical Review Materials***, Vol. 4, No. 7, (2020), 074606. https://doi.org/10.1103/PhysRevMaterials.4.074606
24. Meyer, B. K., Polity, A., Reppin, D., Becker, M., Hering, P., Klar, P. J., Sander, T., Reindl, C., Benz, J., Eickhoff, M., Heiliger, C., "Binary copper oxide semiconductors: From materials towards devices", ***Physica Status Solidi (b)***, Vol. 249, No. 8, (2012), 1487-1509. https://doi.org/10.1002/pssb.201248128
25. Sawicka-Chudy, P., Sibiński, M., Rybak-Wilusz, E., Cholewa, M., Wisz, G., Yavorskyi, R., "Review of the development of copper oxides with titanium dioxide thin-film solar cells", ***AIP Advances***, Vol. 10, No. 1, (2020), 010701. https://doi.org/10.1063/1.5125433
26. Liu, A., Zhu, H., Noh, Y. Y., "Polyol reduction: a low-temperature eco-friendly solution process for p-channel copper oxide-based transistors and inverter circuits", ***ACS Applied Materials & Interfaces***, Vol. 11, No. 36, (2019) 33157-33164. https://doi.org/10.1021/acsami.9b11161
27. Zhu, H., Liu, A., Noh, Y. Y., "Impact of humidity on the performance and stability of solution-processed copper oxide transistors", ***IEEE Electron Device Letters***, Vol. 41, No. 7, (2020), 1033-1035. https://doi.org/10.1109/LED.2020.2993324
28. Liu, A., Zhu, H., Noh, Y. Y., "Molecule Charge Transfer Doping for p-Channel Solution-Processed Copper Oxide Transistors", ***Advanced Functional Materials***, Vol. 30, No. 24, (2020), 2002625. https://doi.org/10.1002/adfm.202002625
29. Baig, S., Kumar, P., Ngai, J., Li, Y., Ahmed, S., "Yttrium Doped Copper (II) Oxide Hole Transport Material as Efficient Thin Film Transistor", ***ChemPhysChem***, Vol. 21, No. 9, (2020), 895-907. https://doi.org/10.1002/cphc.202000005
30. Trinh, B. N. Q., Van Dung, N., Hoa, N. Q., Duc, N. H., Fujiwara, A., "Solution-processed cupric oxide p-type channel thin-film transistors", ***Thin Solid Films***, Vol. 704, (2020), 137991. https://doi.org/10.1016/j.tsf.2020.137991
31. Reker, J., Meyers, T., Vidor, F. F., Hilleringmann, U., "Inorganic p-channel thin-film transistors using CuO nanoparticles", In ***Proc. SPIE 11043, Fifth Conference on Sensors, MEMS, and Electro-Optic Systems***, Vol. 11043, (2019), 1104312. https://doi.org/10.1117/12.2500644
32. Shijeesh, M. R., Jayaraj, M. K., "Low temperature fabrication of CuxO thin-film transistors and investigation on the origin of low field effect mobility", ***Journal of Applied Physics***, Vol. 123, No. 16, (2018), 161538. https://doi.org/10.1063/1.4991812
33. Mazhari, B., Gao, G. B., Morkoc, H., "Collector-emitter offset voltage in heterojunction bipolar transistors", ***Solid-State Electronics***, Vol. 34, No. 3, (1991), 315-321. https://doi.org/10.1016/0038-1101(91)90190-A

Advanced Ceramics Progress: Vol. 7, No. 2, (Season 2021) 34-43

Materials and Energy Research Center
MERC

Contents lists available at ACERP

Advanced Ceramics Progress

Journal Homepage: www.acerp.ir

Original Research Article

Optical Properties and Crystallization Behavior of SiO_2-Al_2O_3-BaO-BaF_2 Glasses Containing Different Amounts of Bi_2O_3

A. Ahmadi Kordlar [a], M. Rezvani [b] *

[a] *MS, Department of Materials Engineering, Faculty of Mechanical Engineering, University of Tabriz, Tabriz, East Azerbaijan, Iran*
[b] *Professor, Department of Materials Engineering, Faculty of Mechanical Engineering, University of Tabriz, Tabriz, East Azerbaijan, Iran*

ARTICLE INFO

Article History:

Received 24 May 2021
Received in revised form 14 July 2021
Accepted 10 August 2021

Keywords:

Optical Glass
Oxy-Fluoride
BaF_2
Bi_2O_3

ABSTRACT

The present study aims to investigate the optical properties and crystallization behavior of oxy-fluoride glasses with different amounts of Bi_2O_3. Glasses with compositions of $45SiO_2$-$15Al_2O_3$-$25BaO$-$15BaF_2$-xBi_2O_3 (x=0, 1, 2.5, 4, and 6) (mole ratio) were prepared using melt-quenching method. Owing to the network modifying role of Bi_2O_3 and increasing number of Non-Bridging Oxygens (NBOs), the molar volume increased from 27.69 to 31.60 cm^3 and microhardness was reduced from 720.21 to 613.10 MPa. In order to study the structural changes, the FTIR spectra were recorded, and increment of NBOs by adding Bi_2O_3 as well as the presence of Bi° particles in the sample containing six mole ratios of Bi_2O_3 were proved. The UV-Vis transmittance spectra were employed to determine the optical properties including Fermi energy, direct and indirect optical band gaps, and Urbach energy. The Fermi energy and optical band gaps were reduced as the Bi_2O_3 content increased. The degree of structural disorderliness (Urbach energy) increased from 0.170 to 0.212 eV followed by creating more NBOs through Bi_2O_3 addition. On the basis of UV-Vis-IR transmittance results, the sample containing four mole ratios of Bi_2O_3 exhibited the highest transmittance in IR region and its IR cut-off shifted to longer wavelengths. Further, the sample with six mole ratios of Bi_2O_3 was characterized as the highest refractive index (1.7) among other glasses. Finally, evaluation of crystallization behavior of specimens revealed that it was impossible to prepare transparent glass ceramics containing BaF_2 nanocrystals due to the surface crystallization in these glasses.

https://doi.org/10.30501/ACP.2021.287637.1063

1. INTRODUCTION

Rare-earth-doped transparent glasses and glass ceramics are important materials with many applications in photonics such as optical fibers, laser host materials, up-conversion lasers, amplifiers, and three-dimensional displays [1-3]. Although oxide glasses and glass ceramics are characterized by thermal, chemical, and mechanical durability, their high phonon energies (~1100 cm^{-1}) and limited solubility of rare-earth ions have restricted their optical applications [4-8]. On the contrary, apart from the low phonon energies (~500 cm^{-1}) of fluoride glasses, they suffer high devitrification rate during preparation as well as low chemical, mechanical, and thermal stability [9,10]. Since acceptable optical properties are not enough for an optical material, special efforts have been devoted to produce novel glasses based on both oxides and fluorides. Introduction of oxygen to fluoride glasses or addition of fluorine to oxide glasses increases their crystallization rates; however, it is revealed that oxygen can stabilize the amorphous state when added as specific oxides to fluoride melts [11]. Accordingly, these types of

* Corresponding Author Email: m_rezvani@tabrizu.ac.ir (M. Revani)
URL: https://www.acerp.ir/article_136414.html

Please cite this article as: Ahmadi Kordlar, A., Rezvani, M., "Optical Properties and Crystallization Behavior of SiO_2-Al_2O_3-BaO-BaF_2 Glasses Containing Different Amounts of Bi_2O_3", ***Advanced Ceramics Progress***, Vol. 7, No. 2, (2021), 34-43. https://doi.org/10.30501/ACP.2021.287637.1063

glasses, called oxy-fluoride glasses, were introduced which received considerable attention since they benefited from advantages of both fluoride and oxide glasses [11,12]. These new materials were considered as excellent hosts for rare-earth ions; however, the structural defects caused by the amorphous structure can entrap electrons and holes, thus resulting in non-radiative processes [13]. In order to solve this problem, oxy-fluoride glass ceramics were introduced and prepared by Wang and Ohwaki [14] for the first time. The precipitated crystalline phase in these glass ceramics was $Pb_xCd_{1-x}F_2$ nanocrystals, and the doped ions (Yb^{3+} and Er^{3+}) were preferably segregated from the glassy matrix to the crystalline phase [14]. Due to the environmental problems of PbF_2 and CdF_2, other oxy-fluoride systems were proposed [15]. Among the several already existing systems, the species with MF_2 (M= Ba, Ca, and Sr) nanocrystals have become of interest owing to their economical and non-toxic raw materials [16]. Furthermore, trivalent rare-earth ions could be substituted for the divalent alkaline-earth cations and lead to suitable solubility of rare-earth ions in MF_2 nanocrystals [17].

BaF_2 in its crystalline form exhibits lower phonon energy (~346 cm^{-1}) than crystalline CaF_2 (~466 cm^{-1}), and its IR cutoff is placed at longer wavelengths. Consequently, the IR window provided by BaF_2 is wider than CaF_2 [18,19]. Nevertheless, contrary to the oxy-fluoride glasses and glass ceramics containing CaF_2, there are only a few studies on optical properties of the aluminosilicate oxy-fluoride systems based on BaF_2 [5,20-23]. Therefore, the present study aims to evaluate the optical properties of new oxy-fluoride glasses of SiO_2-Al_2O_3-BaO-BaF_2 system in the presence of different amounts of Bi_2O_3 additive. The main reason why this additive has been used is the important role of Bi_2O_3 in increasing the refractive index of the glasses [24,25]. To the best of the author's knowledge, no report on its effects of the optical properties of oxy-fluoride glasses and glass ceramics has been found. In this regard, oxy-fluoride glasses with different contents of Bi_2O_3 were prepared using the melt-quenching method. Then, changes in the density, molar volumes, and microhardness of samples were studied. Structural changes and optical properties including transparency in UV-Vis-IR region, Fermi energy, direct and indirect band gap energies, Urbach tailing, and refractive index of glasses were also examined.

2. EXPERIMENTAL PROCEDURE

2.1. Materials, Sample Preparation, and Analyses

Oxy-fluoride glasses with chemical compositions of $45SiO_2$-$15Al_2O_3$-25BaO-$15BaF_2$-xBi_2O_3 (x=0, 1, 2.5, 4, and 6) (mole ratio) were prepared through the conventional melt-quenching method and they were nominated as GBi0, GBi1, GBi2.5, GBi4, and GBi6, respectively. The samples were obtained using high-purity materials such as Al_2O_3 (101077 Merck) and BaF_2 (202746 Sigma-Aldrich). In order to reach high-purity SiO_2 (approximately 99.5%), Hamedan silica was leached by HCl and calcined at 800 °C for 2 hours. $BaCO_3$ (513779 Uni-Chem) was also used to supply BaO.

In this respect, 30 g of batches were melted in covered alumina crucibles in an electric furnace at 1500 °C for one hour. The obtained melts were poured on stainless steel plates and then, they were pressed by another plate to produce disc-shaped glasses with the thickness of 3-5 mm. To relieve internal stresses, the shaped glasses were annealed at 500 °C for one hour and cooled to room temperature with a controlled cooling rate.

To investigate the crystallization behavior and determine the crystallization temperature of samples, Differential Scanning Calorimetry (DSC) was performed (NETZSCH STA 449 F3) at the heating rate of 10 °C/min. In addition, X-Ray Diffraction (XRD) patterns of glasses and crystallized samples were recorded (Philips Xpert MMD system) to identify the amorphous nature of glasses and precipitated crystalline phases in glass ceramics. Vickers microhardness of the glasses was obtained using HV-1000Z Technologies PACE instruments under the load of 1 N for 15 s. The FTIR spectra were recorded by FTIR Tensor 27 Brucker to assess the structural changes. Optical transmittance spectra of bulk glasses in the UV-Vis-IR range of wavelengths were achieved using UV-Vis-NIR Shimadzu 3100 and FTIR Shimadzu 8400S.

2.2. Calculation of Density and Molar Volume

Density (d) of a glass is calculated using Equation (1) with considering its weights in air (W_1) and water (W_2):

$$d = \frac{W_1}{W1\text{-}W_2} \quad (1)$$

Obviously, the relationship between molar volume (V_m) and density is defined by Equation (2), as shown in the following:

$$V_m = \sum \left(\frac{Mi}{d}\right) \quad (2)$$

where M_i is the molar mass of component "i" in glass and is equal to that in Equation (3):

$$M_i = C_i A_i \quad (3)$$

where C_i and A_i are the molar concentration and molecular weight of component "i", respectively.

2.3. UV-VIS Spectra and Optical Constants Measurements

2.3.1. Fermi Energy, Band Gap, and Urbach Tailing

For transparent glasses, Fermi energy level (E_F) is determined using the Fermi-Dirac distribution function (Equation (4)):

$$K(\lambda) = \frac{1}{1 + \exp(\frac{E_F - E}{k_B T})} \quad (4)$$

In Equation (4), E_F and E stand for Fermi energy and energy of the probing photon, respectively. In addition, k_B and K(λ) are Boltzmann constant and extinction coefficient, respectively. This equation can be written as follows:

$$k_B T \, Ln\left(\frac{1}{K} - 1\right) = E_F - E \quad (5)$$

Moreover, K is calculated as follows:

$$K = \frac{\alpha\lambda}{4\pi} \quad (6)$$

where α is the absorption coefficient obtained from UV-Vis spectra. Therefore, plotting K(λ) vs. incident photon energy (hν) and linear fitting of Equation (5) to the linear part of these plots make the calculation of E_F possible [26,27].

According to the model proposed by Tauc and Davis-Mott, light absorption by an amorphous material depends on its optical band gap (E_g) and energy of incident photon (hν) [28,29]. This behavior is represented in Equation (7), as shown in the following:

$$(\alpha h\nu) = \beta^2 (h\nu - E_g)^n \quad (7)$$

where β is a constant and n is an index that exhibits the type of optical transition that takes the values of 2, 3, 1/2, and 1/3 for indirect allowed, indirect forbidden, direct allowed, and direct forbidden transitions, respectively [30-33]. Here, Tauc plots ($(\alpha h\nu)^{1/n}$ vs. hν plots) are employed, and the linear part of these curves is taken into account to compute the band gap energies. In other words, the band gap energy of a glassy material was calculated using the intercept of the linear part of Tau plot divided by its slope.

The disordered structure of amorphous materials is the tailing of electrons density of states into the band gap. The energy of these tails is known as Urbach energy (E_U). Equation (8) shows the relationship between the absorption coefficient and E_U:

$$\alpha = \beta \exp(\frac{h\nu}{E_U}) \quad (8)$$

On the basis of UV-Vis spectra, Ln(α) against hν diagrams can be drawn and E_U can be estimated by least square fitting of Equation (8) to these diagrams [34-37].

2.3.2. Calculation of Refractive Index

The refractive indices of the samples in the UV-Vis region of wavelengths were measured using Fresnel equations (Equations (9) and (10)), reflectance, and transmittance spectra:

$$R = (\frac{N_t - N_i}{N_t + N_i})^2 \quad (9)$$

$$T = (\frac{2N_t}{N_t + N_i})^2 \quad (10)$$

where N_t and N_i are the complex refractive indices of the glass and air, respectively. Moreover, N_t is defined as Equation (11):

$$N = n - iK \quad (11)$$

where K is the extinctions coefficient and n the refractive index. The Reflectance and transmittance spectra of a sample were considered, and a system of two equations and two unknowns was solved by Macleod media, hence the formation of a curve of refractive index vs. wavelength [38,39].

3. RESULTS AND DISCUSSION

3.1. Density, Molar Volume, and Microhardness

Table 1 presents the values of densities and molar volumes of glasses. Incorporation of one mole ratio of Bi_2O_3 decreased the density from 3.84 to 3.74 (g/cm^3); however, higher amounts of Bi_2O_3 increased the density again. In fact, changes in molar mass and molar volume generate variations in density values. As a result of the enhancement of molar mass caused by increasing the Bi_2O_3 content, an increase in the density is required. In contrast, in case Bi_2O_3 plays the role of network modifying, V_m must increase as a consequence of the emergence of more Non-Bridging Oxygens (NBOs) and the density decreases. The calculated value of V_m (Table 1) increase upon adding Bi_2O_3 and approving the network modifying role of this oxide. The effect of V_m outweighs the molar mass in the case of sample GBi1; for other samples, the opposite holds.

Table 1 lists the results from microhardness measurements. Hardness is usually influenced by the introduction of glass network modifiers, which is provoked with the creation of more NBOs and breakup

of the glass network [40]. The decreasing trend of the microhardness of the samples with higher mole ratios of Bi_2O_3 is in accordance with the above-mentioned statement that proves it to some extent.

TABLE 1. Some physical properties of glasses with different amounts of Bi_2O_3

Sample Code	d (g/cm^3)	V_m (cm^3)	Microhardness Hv (MPa)
GBi0	3.84	27.69	720.21
GBi1	3.74	28.41	695.00
GBi2.5	3.77	30.42	677.30
GBi4	3.86	31.05	642.50
GBi6	3.98	31.60	613.10

3.2. Structural Studies

As mentioned in the previous section, Bi_2O_3 acts as a network modifier and affects the glass structure by creating NBOs. To evaluate this claim, FTIR spectra should be studied (Figure 1). All of the samples exhibit three absorption bands at ~440, ~680, and ~970-980 cm^{-1} which are related to rocking, symmetric, and asymmetric stretching vibrations of Si-O-Si bonds, respectively [41]. The wide band with the highest intensity is composed of three over-lapped peaks corresponding to different vibrational modes of Si-O bonds in all silicate units, i.e., Q^n (n=1, 2, 3). The band at 1080-1100 cm^{-1} is generated by stretching vibrations of Si-O bonds with single NBOs (Q^3), and the other one placed at 970-980 cm^{-1} is attributed to the stretching vibration of bonds with two NBOs (Q^2). Finally, the peak at 900-930 cm^{-1}, which is not distinguishable, is created by the stretching vibrations in silicate units with three NBOs (Q^1). Further, Q^1 represents the stretching vibrations of Si-O-Al in aluminosilicate glasses [42,43]. As demonstrated in Figure 1, the position of this broad band shifts to lower wavenumbers from GBi0 to GBi6 and its maximum value is observed at wavenumbers near Q^2 and Q^1 species. Therefore, the number of silicate units with more NBOs grew with the addition of Bi_2O_3. The other band at ~587 cm^{-1} is also related to Si-O-Al asymmetric stretching vibrations [44], and the changes of this band confirm the increase in this type of bonds for samples with Bi_2O_3. Moreover, the broad peak of asymmetric vibrations of Si-O-Si is intensified more than the symmetric vibrations band. All these changes are indicative of the higher numbers of NBOs and disorderliness in the presence of Bi_2O_3 [40].

There are three weak peaks at 1460, 1640, and 1741 cm^{-1} resulting from the vibrations of Al-F bonds [45]. In oxy-fluoride glasses, it is preferred that F^- ions bond to Al^{3+} cations instead of Si^{4+} to decrease the fluorine loss as SiF_4 [46]. Of note, in the spectra of glasses with the exception of GBi6 sample, another weak peak is observed at 534 cm^{-1}, which is probably related to Bi-O bonds. Sample GBi6 lacks this bond mainly because the Bi introduced by six mole ratios of Bi_2O_3 forms Bi° particles (colloidal Bi) instead of Bi-O in this glass, which will be discussed in detail in the next section [47].

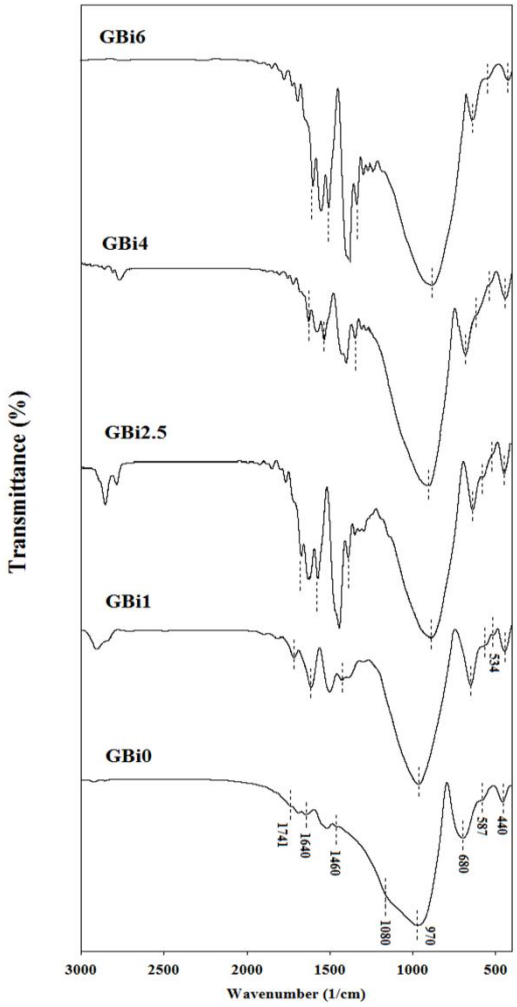

Figure 1. FTIR spectra of glasses containing different amounts of Bi_2O_3

3.3. UV-VIS-IR Transmittance Spectra and Evaluation of Optical Properties

UV-Vis transmittance spectra are plotted in Figure 2. Although there is not any significant difference between the transmittance of samples, their absorption edge has a red-shift to longer wavelengths. Moreover, absorption edges are not sharply defined due to the amorphous nature of the glasses. These absorption edges can be assumed as Urbach fundamental edges [48,49]. A broad absorption peak at ~400-600 nm emerged only for sample GBi6, and it is usually considered as evidence of Bi° particles in glass. In other words, the surface Plasmon resonance of Bi° particles is the reason for this absorption peak [47].

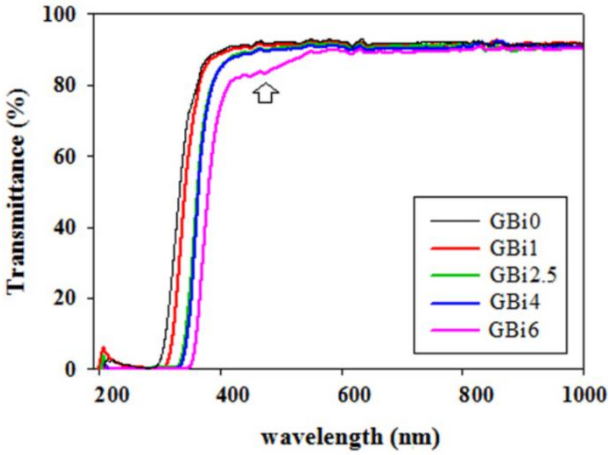

Figure 2. UV-Vis spectra of glasses containing different amounts of Bi_2O_3

Owing to the strong UV absorption rather than visible wavelengths, the extinction coefficient of samples follows Fermi-Dirac distribution function [36], and K(λ) vs. hν plots (Figure 3) are used to calculate Fermi energies, the results of which are demonstrated in Table 2. For this purpose, the linear part of these plots steeping to lower energies was taken into consideration and the formula of the best fitted line to this part was obtained through linear regression analysis. Then, this formula was substituted into Equation (5) and the Fermi energy at each wavelength was calculated. Higher E_F values of glasses compared to k_BT indicate that they are insulators and their insulating behavior varies very slightly to the semiconducting behavior upon adding Bi_2O_3.

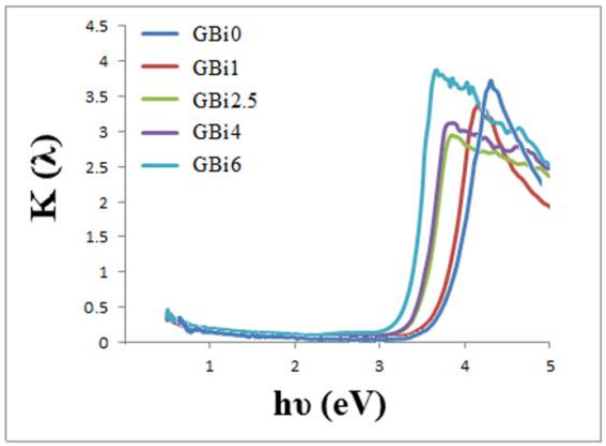

Figure 3. Extinction coefficient vs. energy plots of glasses containing different amounts of Bi_2O_3

Tauc plots of glasses are depicted in Figure 4. The direct and indirect optical band gap energies can be obtained by determining the extrapolation formula of the linear part of these plots and dividing the intercept of this line by its slope. Table 2 includes the values of optical band gaps obtained from these plots. Formation of dangling bonds like NBOs with higher Bi_2O_3 contents reduces the band gap energy by developing the localized states within the band gap and putting the valence and conduction bands closer [50,51].

TABLE 2. Optical properties of oxy-fluoride glasses containing different amounts of Bi_2O_3

Energy (eV) / Sample Code	E_F	$E_{g\ (indirect)}$	$E_{g\ (direct)}$	E_U
GBi0	4.307	3.481	3.950	0.170
GBi1	4.108	3.222	3.752	0.193
GBi2.5	3.805	3.007	3.495	0.204
GBi4	3.759	2.970	3.411	0.209
GBi6	3.649	2.958	3.380	0.212

As stated earlier, in amorphous materials, Urbach tails or the tails of the density of states in forbidden gap spark off the short-range order of these materials. This is the reason why Urbach energy is regarded as a degree of crystallinity and orderliness [50]. To calculate Urbach energies, the slope of the linear part of Ln(α) vs. hν plots (illustrated in Figure 5) is reverted, the results of which are listed in Table 2. In the case of adding Bi_2O_3, Urbach energy increases and this increment is associated with the higher degree of disorderliness caused by increasing the NBOs.

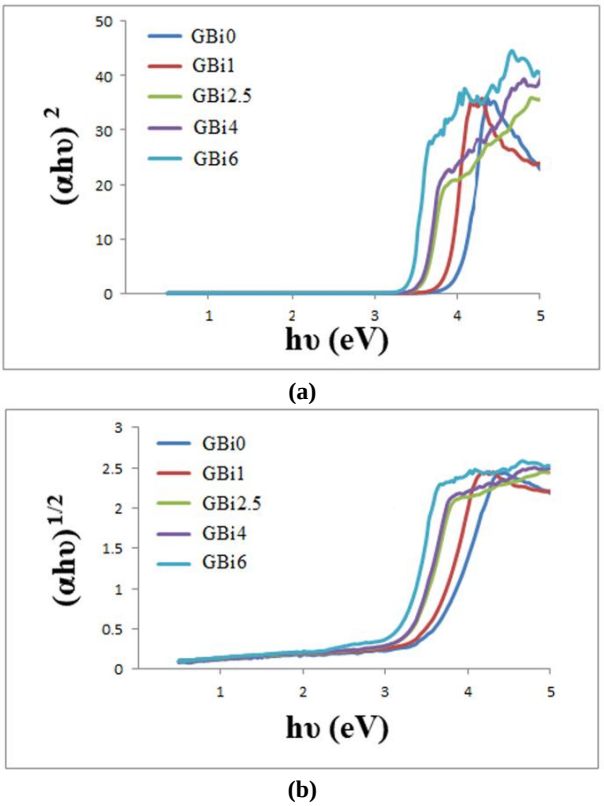

Figure 4. Tauc plots for calculation of (a) direct and (b) indirect band gaps

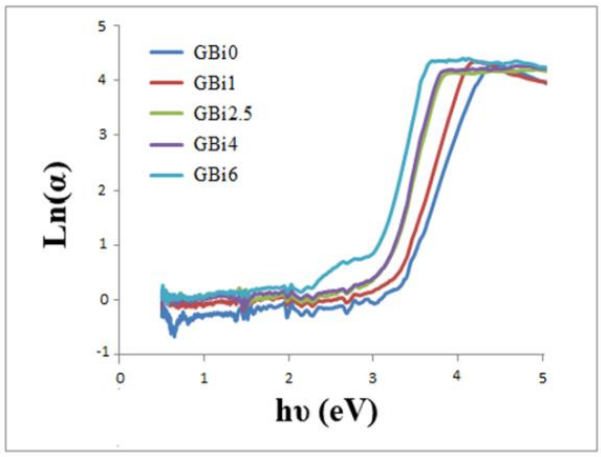

Figure 5. Ln(α) vs. energy diagrams for determination of Urbach energy

Figure 6 illustrates how Bi_2O_3 can affect the IR cut-off position and UV-Vis-IR transmitting window. All of these glasses are transparent in UV-Vis (300-1100 nm) region with transmittance of approximately 90%. In the IR region, the transparencies are acceptable and the IR cut-offs are placed at ~4.7-5 µm. Accordingly, from the IR transmittance point of view, the present glasses can compete with some commercial IR glasses like Schott IRG2 and Schott IR 11 [52].

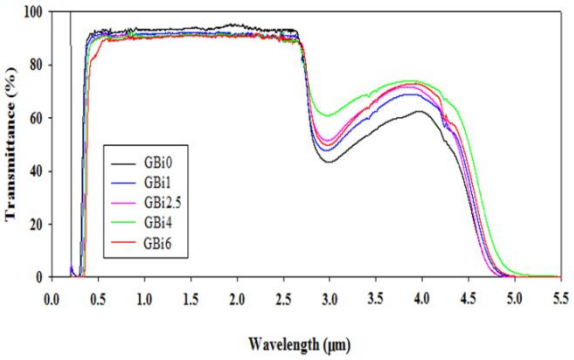

Figure 6. UV-Vis-IR transmittance spectra of glasses containing different amounts of Bi_2O_3

Generally, light absorption in the IR region is different from that in the UV-Vis region of spectrum. Most optical absorptions in the IR region in glasses result from vibrational transitions. The frequency (ν) of a vibrational absorption is given as follows:

$$\nu = (\frac{1}{2\pi})\sqrt{\frac{F}{\mu}} \quad (12)$$

where F is the force constant for bond energy and µ the effective mass [53,54]. According to Section 3.1., the molar mass and number of NBOs increase by introducing Bi_2O_3. Generation of NBOs indicates the F parameter and absorption in the IR region and shifts the IR cut-off to longer wavelengths [37]. However, in case the amount of Bi_2O_3 exceeds four mole ratios, transmittance descents and IR cut-off demonstrate a blue-shift again, mainly due to the light scattering by Bi° particles in GBi6.

The values of the refractive index of glasses as a function of wavelength are presented in Figure 7. In case the quantity of Bi_2O_3 increases, the higher refractive index ensues. In fact, the refractive index of a glass is determined by the interaction of light with electrons of constituent atoms of the glass. In addition, upon increasing the electron density or polarizability of ions, the refractive index would increase. Furthermore, NBOs are more polarizable than bridging oxygens with the ability to increase the refractive index. The polarizability of cations plays a significant role [53]. Of note, the main reasons for such increase in the refractive index include the high polarizability of Bi^{3+} cations and creation of more NBOs.

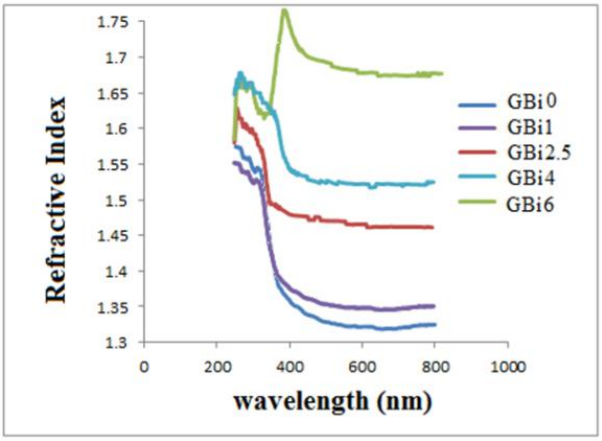

Figure 7. Refractive index curves of glasses containing different amounts of Bi_2O_3

3.4. Crystallization Behavior and Feasibility Study of Transparent Glass-Ceramic Preparation

As reported by other researchers, there are usually two exothermic peaks in the DSC thermo-grams of oxy-fluoride glasses based on BaF_2 [55-57].

In the DSC results of the present glasses (Figure 8), two exothermic peaks are observed. The first peak at lower temperatures is ascribed to the crystallization of BaF_2, and the second one at higher temperatures is related to the crystallization of glassy matrix [58]. According to this figure, the shape of the first peak changes with higher amounts of Bi_2O_3. The crystallization peak of BaF_2 moves to lower temperatures in the presence of Bi_2O_3,

followed by increase in its content since Bi_2O_3 increases the number of NBOs and enhances crystallization. Bocker and Russel [59] proposed a self-organizing model for nano-crystallization of BaF_2 from oxy-fluoride glasses where a highly viscous layer enriched by network former cations was formed that acted a diffusion barrier hindering the crystal growth.

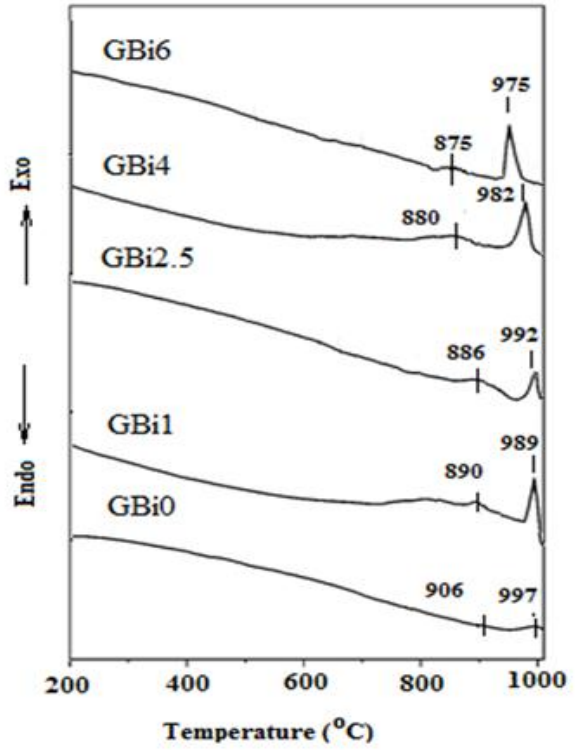

Figure 8. DSC curves of glasses containing various amounts of Bi_2O_3

In case the number of NBOs in oxy-fluoride glasses increased, the residual glassy matrix became less viscous and ions diffused the barrier easier. Therefore, NBOs facilitate the crystallization of BaF_2 and reduce its crystallization temperature [16].

In the XRD patterns of as-made glasses (Figure 9(a)), no diffraction peak is observed since samples are amorphous, hence no unwanted crystallization. Glasses were heat-treated at their first peak temperature for two hours, the XRD patterns of which are depicted in Figure 9(b). Despite the DSC results and our expectations, BaF_2 crystals were not precipitated in samples. Heat-treating at higher temperatures could not solve the problem and apparently, the heat-treated samples lost their transparency. Finally, in glasses crystallized at their second peak temperature, BaF_2 was obtained in company with $BaAl_2Si_2O_8$ (Figure 9(c)).

Hence, it is assumed that crystallization is a surface crystallization process. GBi4 was chosen to justify this possibility, and a fine sample of it was prepared to compare its DSC results with those of the coarse glass sample (Figure 10). The crystallization peak of BaF_2 for the fine sample moved to lower temperature and got sharper, which proved that the crystallization process began from the surface and made it impossible to prepare transparent glass ceramics from the glasses under study. Moreover, hanging the crystallization circumstances has not shown any positive effect on the crystallization of BaF_2 in these glasses and preparation of transparent oxy-fluoride glasses with BaF_2 nanocrystals [60].

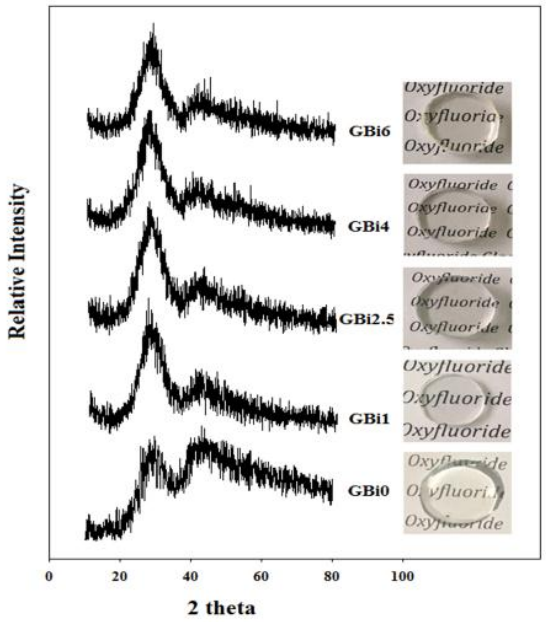

(a)

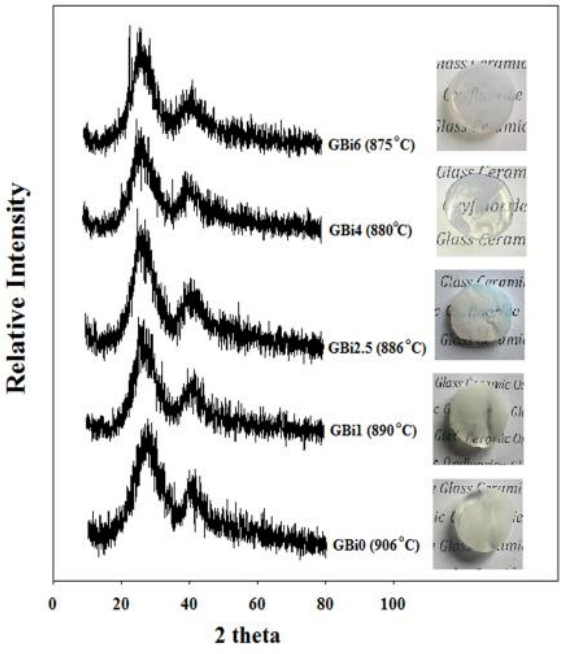

(b)

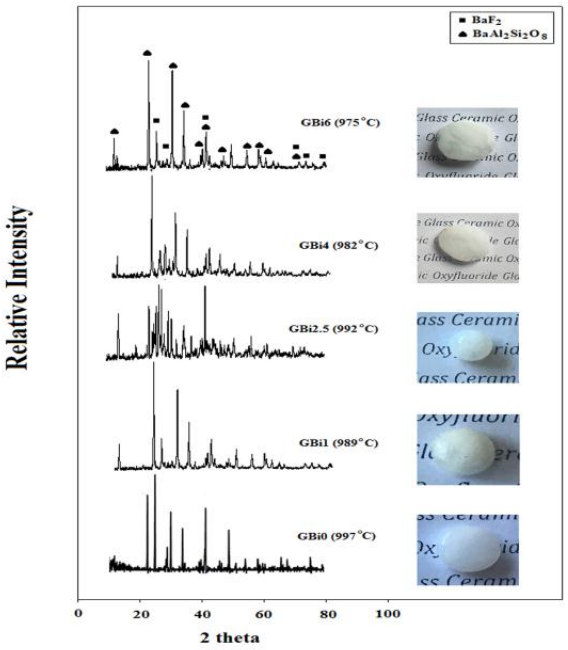

(c)

Figure 9. XRD patterns of (a) as-made glasses and glasses heat-treated at (b) first peak and (c) second peak temperature of DSC results

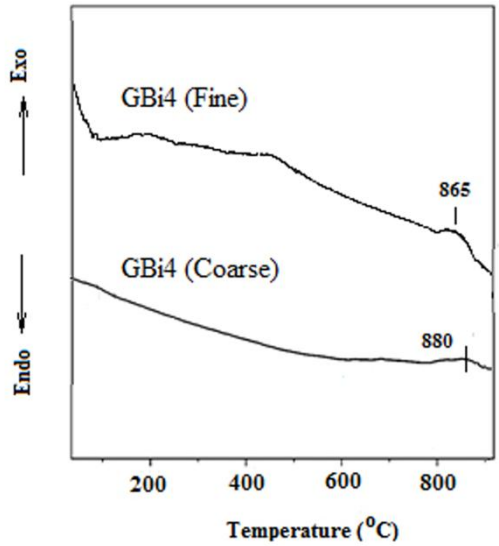

Figure 10. DSC curves of fine and coarse samples of GBi4 glass

4. CONCLUSIONS

- Oxy-fluoride glasses containing different amounts of Bi_2O_3 were prepared using the melt-quenching method. All of the samples were amorphous without any unwanted crystallization as demonstrated by XRD patterns.
- Bi_2O_3 played the role of network modifier, and the value of V_m increased from 27.69 to 31.60 cm^3 for samples GBi0 to GBi6.
- FTIR and UV-Vis spectra proved the presence of Bi° particles in the sample with six mole ratios of Bi_2O_3.
- By adding Bi_2O_3, Fermi energy level and band gap energies decreased and the insulating behavior of glasses was mitigated.
- Urbach energy of sample with more contents of Bi_2O_3 increased from 0.170 to 0.212 eV due to the formation of more NBOs and increment of disorderliness.
- Bi_2O_3 up to four mole ratios increased transmittance and shifted the cut-off to longer wavelengths in IR region.
- In the case of the glass GBi6, refractive index increased to 1.7 due to the higher polarizablility of Bi^{3+} ions and enhancement of NBOs.
- The first exothermic peak in DSC curves related to the crystallization of BaF_2 was moved to lower temperatures due to the creation of more NBOs in the presence of Bi_2O_3. Moreover, transparent glass ceramics were not obtained because of the surface crystallization process.

ACKNOWLEDGEMENTS

We would like to show our gratitude to Ali Rahimian and Laleh Farahinia, our colleagues who provided insight and experties that assisted this research.

REFERENCES

1. Miao, X., Bai, Z., Huo, X., Guo, M., Cheng, F., Zhang, M., "Controllable preparation of CaF_2 transparent glass ceramics: dependence of the light transmittance mechanism on the glass crystallization behaviour", ***Ceramics International***, Vol. 45, No. 7, (2019), 8510-8517. https://doi.org/10.1016/j.ceramint.2019.01.164
2. Gonçalves, M. C., Santos, L. F., Almeida, R. M., "Rare-earth-doped transparent glass ceramics", ***Comptes Rendus Chimie***, Vol. 5, No. 12, (2002), 845-854. https://doi.org/10.1016/S1631-0748(02)01457-1
3. Cai, J., Wei, X., Hu, F., Cao, Z., Zhao, L., Chen, Y., Duan, C., Yin, M., "Up-conversion luminescence and optical thermometry properties of transparent glass ceramics containing CaF_2:Yb^{3+}/Er^{3+} nanocrystals", ***Ceramics International***, Vol. 42, No. 12, (2016), 13990-13995. https://doi.org/10.1016/j.ceramint.2016.06.002
4. Caldiño, U., Bettinelli, M., Ferrari, M., Pasquini, E., Pelli, S., Speghini, A., Righini, G. C., "Rare earth doped glasses for displays and light generation", In Vincenzini, P. (ed.), ***Advances in Science and Technology***, Switzerland: Trans Tech Publications Ltd, Vol. 90, (2014), 174-178. https://doi.org/10.4028/www.scientific.net/AST.90.174
5. Jia, S., Huang, L., Ma, D., Tai, Z., Zhao, S., Deng, D., Wang, H., Jia, G., Hua, Y., Yang, Q., Xu, S., "Luminescence properties of Tb^{3+}-doped oxyfluoride scintillating glasses", ***Journal of***

Luminescence, Vol. 152, (2014), 241–243. https://doi.org/10.1016/j.jlumin.2013.12.036
6. Righini, G. C., Enrichi, F., Zur, L., Ferrari, M., "Rare-earth doped glasses and light Managing in Solar Cells", In ***Journal of Physics: Conference Series***, Mexico, 5–9 November 2018, IOP Publishing Ltd, Vol. 1221, No. 1, (2019), 012028. https://doi.org/10.1088/1742-6596/1221/1/012028
7. Righini, C. G., Ferrari, M., "Photoluminescence of rare-earth-doped glasses", ***La Rivista del Nuovo Cimento***, Vol. 28, No. 12, (2005), 1-53. https://doi.org/10.1393/ncr/i2006-10010-8
8. Kishi, Y., Tanabe, S., "Infrared-to-visible upconversion of rare-earth doped glass Ceramics Containing CaF_2 crystals", ***Journal of Alloys and Compounds***, Vol. 408–412, (2006), 842–844. https://doi.org/10.1016/j.jallcom.2005.01.096
9. Stevenson, A. J., Serier-Brault, H., Gredin, P., Mortier, M., "Fluoride materials for optical applications: single crystals, ceramics, glasses, and glass–ceramics", ***Journal of Fluorine Chemistry***, Vol. 132, No. 12, (2011), 1165–1173. https://doi.org/10.1016/j.jfluchem.2011.07.017
10. Poulain, M., Soufiane, A., Messaddeq, Y., Aegerter, M. A., "Fluoride glasses: synthesis and properties", ***Brazilian Journal of Physics***, Vol. 22, No. 3, (1992), 205-217. http://sbfisica.org.br/bjp/download/v22/v22a24.pdf
11. Polishchuk, S. A., Ignat'eva, L. N., Marchenko, Y. V., Bouznik, V. M., "Oxyfluoride glasses (a review)", ***Glass Physics and Chemistry***, Vol. 37, No. 1, (2011), 1–20. https://doi.org/10.1134/S108765961101010X
12. E1-Mallawany, R., Khafagy, A. H., Ewaida, M. A., Hager, I. Z., Poulain, M. A., Poulain, M. J., "Some physical properties of new oxyfluoride glasses", ***Journal of Non-Crystalline Solids***, Vol. 184, (1995), 141-146. https://doi.org/10.1016/0022-3093(94)00657-1
13. Zhu, L., Lu, A., Zuo, C., Shen, W., "Photoluminescence and energy transfer of Ce^{3+} and Tb^{3+} doped oxyfluoride Aluminosilicate glasses", ***Journal of Alloys and Compounds***, Vol. 509, No. 29, (2011), 7789-7793. https://doi.org/10.1016/j.jallcom.2011.04.154
14. Wang, Y., Ohwaki, J., "New transparent vitroceramics codoped with Er^{3+} and Yb^{3+} for efficient frequency upconversion", ***Applied Physics Letters***, Vol. 63, No. 24, (1993), 3268-3270. https://doi.org/10.1063/1.110170
15. Babu, P., Jang, K. H., Kim, E. S., Shi, L., Seo, H. J., Lopez, F. E., "Optical properties and white-light emission in Dy^{3+}-doped transparent oxyuoride glass and glass ceramics containing CaF_2 nanocrystals", ***Journal of the Korean Physical Society***, Vol. 54, No. 4, (2009), 1488-1491. https://doi.org/10.3938/jkps.54.1488
16. Imanieh, M. H., Eftekhari Yekta, B., Marghussian, V., Shakhesi, S., Martin, I. R.,"Crystallization of nano calcium fluoride in CaF_2-Al_2O_3-SiO_2 system", ***Solid State Sciences***, Vol. 17, (2013), 76-82. https://doi.org/10.1016/j.solidstatesciences.2012.11.008
17. Qiao, X., Fan, X., Wang, M., "Luminescence behavior of Er^{3+} in glass ceramics containing BaF_2 nanocrystals", ***Scripta Materialia***, Vol. 55, No. 3, (2006), 211-214. https://doi.org/10.1016/j.scriptamat.2006.04.023
18. Richman, I., "Longitudinal optical phonons in CaF_2, SrF_2, and BaF_2", ***The Journal of Chemical Physics***, Vol. 41, No. 9, (1964), 2836-2837. https://doi.org/10.1063/1.1726360
19. Zhao, Z., Liu, C., Xia, M., Yin, Q., Zhao, X., Han, J., "Intense ~1.2 μm emission from Ho^{3+}/Y^{3+} ions co-doped oxyfluoride glass-ceramics containing BaF_2 nanocrystals", ***Journal of Alloys and Compounds***, Vol. 701, (2017), 392-398. https://doi.org/10.1016/j.jallcom.2017.01.162
20. Yin, Q., Zhang, J., Liu, C., Xie, J., So, B. J., Heo, J., Zhao, X., "Dual-band photoluminescence of lead selenide quantum dots doped oxyfluoride class-ceramics containing BaF_2 nanocrystals", ***Journal of Non-Crystalline Solids***, Vol. 385, (2014), 136-141. https://doi.org/10.1016/j.jnoncrysol.2013.11.019
21. Chewpraditkul, W., Pattanaboonmee, N., Yawai, N., Chewpraditkul, W., Lertloypanyachai, P., Sreebunpeng, K., Yoshino, M., Liu, L., Chen, D., "Luminescence and scintillation properties of Ce^{3+}-doped SiO_2-Al_2O_3-BaF_2-Gd_2O_3 glasses", ***Optical Materials***, Vol. 98, (2019), 109468. https://doi.org/10.1016/j.optmat.2019.109468
22. Lakshminarayana, G., Qiu, J., "Photoluminescence of Pr^{3+}, Sm^{3+} and Dy^{3+}-doped SiO_2-Al_2O_3-BaF_2-GdF_3 glasses", ***Journal of Alloys and Compounds***, Vol. 476, No. 1-2, (2009), 470-476. https://doi.org/10.1016/j.jallcom.2008.09.015
23. Du, Y., Han, S., Zou, Y., Yuan, J., Shao, C., Jiang, X., Chen, D., "Luminescence properties of Ce^{3+}-doped oxyfluoride aluminosilicate glass and glass ceramics", ***Optical Materials***, Vol. 89, (2019), 243-249. https://doi.org/10.1016/j.optmat.2019.01.018
24. Oo, H. M., Mohamed-Kamari, H., Wan-Yusoff, W. M. D., "Optical properties of bismuth tellurite based glass", ***International Journal of Molecular Sciences***, Vol. 13, No. 4, (2012), 4623-4631. https://doi.org/10.3390/ijms13044623
25. Halimah, M. K., Sidek, H. A. A., Daud, W. M., Zainal, A. S., Mansor, H., Khamirul, A. M., "Physical properties of binary tellurite glass system", ***Solid State Science Technology***, Vol. 18, (2010), 364-370. https://doi.org/10.2109/jcersj1950.86.995_316
26. Khashan, M. A., El-Naggar, A. M., "A new method of finding the optical constants of a solid from the reflectance and transmittance spectrograms of its slab", ***Optics Communications***, Vol. 174, No. 5-6, (2000), 445–453. https://doi.org/10.1016/S0030-4018(99)00721-X
27. El-Kameesy, S. U., Eissa, H. M., Eman, S. A., El-Gamma, Y. A., "Fast neutron irradiation effect on some optical properties of lead borate glass doped with samarium oxide", ***Egyptian Journal of Pure and Applied Science***, Vol. 49, No. 1., (2011), 067-070. https://doi.org/10.21608/ejaps.2011.186253
28. Li, X., Zhu, H., Wei, J., Wang, K., Xu, E., Li, Z., Wu, D., "Determination of band gaps of self-sssembled carbon nanotube films using Tauc/Davis–Mott model", ***Applied Physics A***, Vol. 97, No., 2, (2009), 341–344. https://doi.org/10.1007/s00339-009-5330-z
29. Gautam, C. R., Das, S., Gautam, S. S., Madheshiya, A., Singh, A. K., "Processing and optical characterization of lead calcium titanate borosilicate glass doped with germanium", ***Journal of Physics and Chemistry of Solids***, Vol. 115, (2018), 180–186. https://doi.org/10.1016/j.jpcs.2017.12.038
30. Ghayebloo, M., Rezvani, M., Tavoosi, M., "The relationship between structural and optical properties of Se-Ge-As glasses", ***Infrared Physics and Technology***, Vol. 90, (2018), 40-47. https://doi.org/10.1016/j.infrared.2018.02.004
31. Bavafa, P., Rezvani, M., "Effect of Sn doping in optical properties of Se-Ge glass and glass-ceramics", ***Results in Physics***, Vol. 10, (2018), 777-783. https://doi.org/10.1016/j.rinp.2018.07.021
32. Ibrahim, A., Al-Ani, S K. J., "Models of optical absorption in amorphous semiconductors at the absorption edge-a review and re-evaluation", ***Czechoslovak Journal of Physics***, Vol. 44, No. 8, (1994), 785–797. https://doi.org/10.1007/BF01700645
33. Abdel-Baki, M., Abdel-Wahab, F. A., El-Diasty, F., "One-photon band gap engineering of borate glass doped with ZnO for photonics applications", ***Journal of Applied Physics***, Vol. 111, No. 7, (2012), 073506. https://doi.org/10.1063/1.3698623
34. Shakeri, M. S., Rezvani, M., "Optical properties and structural evaluation of Li_2O-Al_2O_3-SiO_2-TiO_2 glassy semiconductor containing passive agent CeO_2", ***Spectrochimica Acta Part A: Molecular and Biomolecular Spectroscopy***, Vol. 83, No. 1, (2011), 592–597. https://doi.org/10.1016/j.saa.2011.09.009
35. Sayyed, M. I., Rammah, Y. S., Laariedh, F., Abouhaswa, A. S., Badeche, T. B., "Lead borate glasses doped by lanthanum: synthesis, physical, optical, and gamma photon shielding properties", ***Journal of Non-Crystalline Solids***, Vol. 527, (2020), 119731. https://doi.org/10.1016/j.jnoncrysol.2019.119731
36. Khani, V., Alizadeh, P., Shakeri, M. S., "Optical properties of transparent glass-ceramics containing

lithium-mica nanocrystals: crystallization effect", ***Materials Research Bulletin***, Vol. 48, No. 9, (2013), 3579-3584. https://doi.org/10.1016/j.materresbull.2013.05.061

37. Farahinia, L., Rezvani, M., Rezazadeh, M., "Effect of CaF_2 substitution by CaO on spectroscopic properties of oxyfluoride glasses", ***Materials Research Bulletin***, Vol. 139, (2021), 111265. https://doi.org/10.1016/j.materresbull.2021.111265
38. Pedrotti, F. L., Pedrotti, L. M., Pedrotti, L. S., ***Introduction to Optics***, 3rd Ed., Prentice-Hall International, Inc., (1993). http://faculty.du.ac.ir/rajabi/wp-content/uploads/sites/197/2020/09/PEDROTTI-Introduction-to-Optics_3rd.pdf
39. Macleod, H. A., ***Thin-Film Optical Filters***, 4th Ed., Boca Raton, FL: CRC Press, (2010). https://doi.org/10.1201/9781420073034
40. Limbach, R., Karlsson, S., Scannell, G., Mathew, R., Edén, M., Wondraczek, L., "The effect of TiO_2 on the structure of Na_2O-CaO-SiO_2 glasses and its implications for thermal and mechanical properties", ***Journal of Non-Crystalline Solids***, Vol. 471, (2017), 6–18. https://doi.org/10.1016/j.jnoncrysol.2017.04.013
41. Kansal, I., Goel, A., Tulyaganov, D. U., Rajagopal, R. R., Ferreira, J. M., "Structural and thermal characterization of CaO-MgO-SiO_2-P_2O_5-CaF_2 glasses", ***Journal of European Ceramic Society***, Vol. 32, No. 11, (2012), 2739-2746. https://doi.org/10.1016/j.jeurceramsoc.2011.10.041
42. Środa, M., Paluszkiewicz, C., "The structural role of alkaline earth ions in oxyfluoride aluminosilicate glasses-infrared spectroscopy study", ***Vibrational Spectroscopy***, Vol. 48, No. 2, (2008), 246-250. https://doi.org/10.1016/j.vibspec.2008.02.017
43. Mukherjee, D. P., Kumar Das, S., "Effects of nano silica on synthesis and properties of glass ceramics in SiO_2-Al_2O_3-CaO-CaF_2 glass system: A comparison", ***Journal of Non-Crystalline Solids***, Vol. 368, (2013), 98-104. https://doi.org/10.1016/j.jnoncrysol.2013.03.012
44. Farahinia, L., Rezvani, M., Rezazadeh, M., "An investigation into the effects of composition and BaF_2 content on the structure and crystallization behavior of SiO_2-Al_2O_3-K_2O-BaF_2 oxyfluoride glasses", ***Advanced Ceramics Progress***, Vol. 6, No. 1, (2020), 16-21. https://doi.org/10.30501/ACP.2020.105927
45. Snelson, A., "Infrared spectrum of AlF_3, Al_2F_6, and AlF by matrix isolation", ***The Journal of Physical Chemistry***, Vol. 71, No. 10, (1967), 3202-3207. https://doi.org/10.1021/j100869a011
46. Fedorov, P. P., Luginina, A. A., Popov, A. I., "Transparent oxyfluoride glass ceramics", ***Journal of Fluorine Chemistry***, Vol. 172, (2015), 22–50. https://doi.org/10.1016/j.jfluchem.2015.01.009
47. Singh, S. P., Karmakar, B., ***Bismuth oxide and bismuth oxide doped glasses for optical and photonic applications***, (2012). http://cgcri.csircentral.net/1384/1/SPS-Book_Chapter_.pdf
48. Azlan, M. N., Halimah, M. K., Suriani, A. B., Azlina, Y., El-Mallawany, R., "Electronic polarizability and third-order nonlinearity of Nd^{3+} doped borotellurite glass for potential optical fiber", ***Materials Chemistry and Physics***, Vol. 236, (2019), 121812. https://doi.org/10.1016/j.matchemphys.2019.121812
49. Kitamura, N., Fukumi, K., Nakamura, J., Hidaka, T. Hashima, H., Mayumi, Y., Nishii, J., "Optical properties of zinc bismuth phosphate glass", ***Materials Science and Engineering: B***, Vol. 161, No. 1-3, (2009), 91-95. https://doi.org/10.1016/j.mseb.2008.12.023
50. Abdel-Baki, M., El-Diasty, F., Abdel Wahab, F. A. A., "Optical characterization of xTiO_2-(60-x)SiO_2-40Na_2O glasses: II. absorption edge, fermi level, electronic polarizability and optical basicity", ***Optics Communications***, Vol. 261, No, 1, (2006), 65-70. https://doi.org/10.1016/j.optcom.2005.11.056
51. Zhang, X. H., Bureau, B., Lucas, P., Boussard-Pledel, C., Lucas, J., "Glasses for seeing beyond visible", ***Chemistry-A European Journal***, Vol. 14, No. 2, (2008), 432-442. https://doi.org/10.1002/chem.200700993
52. Tang, B., Wu, C., Li, J., Fan, Y., Hu, H., Zhang, L., "Large-size oxyfluoride glasses used for vis-IR-transmitting", ***Journal of Non-Crystalline Solids***, Vol. 355, No. 37-42, (2009), 2006-2009. https://doi.org/10.1016/j.jnoncrysol.2009.01.060
53. Ghayebloo, M., Tavoosi, M., Rezvani, M., "Investigation of comparative effects of antimony and arsenic on the structural and optical behaviors of IR transparent $Ge_{40}Se_{60}$ glass", ***Infrared Physics & Technology***, Vol. 109, (2020), 103387. https://doi.org/10.1016/j.infrared.2020.103387
54. Shelby, J. E., ***Introduction to Glass Science and Technology***, 2nd Edition, Cambridge: Royal Society of Chemistry, (2005). https://doi.org/10.1039/9781847551160
55. Antuzevics, A., Kemere, M., Ignatans, R., "Local structure of gadolinium in oxyfluoride glass matrices containing SrF_2 and BaF_2 crystallites", ***Journal of Non-Crystalline Solids***, Vol. 449, (2016), 29-33. https://doi.org/10.1016/j.jnoncrysol.2016.07.015
56. Sung, Y. M., "Crystallization kinetics of fluoride nanocrystals in oxyfluoride glasses", ***Journal of Non- Crystalline Solids***, Vol. 358, No. 1, (2012), 36-39. https://doi.org/10.1016/j.jnoncrysol.2011.08.016
57. Bocker, C., Wiemert, J., Rüssel, C., "The formation of strontium fluoride nano crystals from a phase separated silicate glass", ***Journal of the European Ceramic Society***, Vol. 33, No. 10, (2013), 1737-1745. https://doi.org/10.1016/j.jeurceramsoc.2013.02.008
58. Huang, L., Jia, S., Li, Y., Zhao, S., Deng, D., Wang, H., Jia, G., Hua, Y., Xu, S., "Enhanced emissions in Tb^{3+}-doped oxyfluoride scintillating glass ceramics containing BaF_2 nanocrystals", ***Nuclear Instruments and Methods in Physics Research A: Accelerators, Spectrometers, Detectors and Associated Equipment***, Vol. 788, (2015), 111-115. https://doi.org/10.1016/j.nima.2015.03.084
59. Bocker, C., Rüssel, C., "Self-organized nano-crystallisation of BaF_2 from Na_2O/K_2O/BaF_2/Al_2O_3/SiO_2 glasses", ***Journal of the European Ceramic Society***, Vol. 29, No. 7, (2009), 1221-1225. https://doi.org/10.1016/j.jeurceramsoc.2008.08.005
60. Haddadi kahnamouei, R., Rezvani, M., "Investigation of Crystallization Behavior of SiO_2-Al_2O_3-BaO-BaF_2 Glass Ceramics", In ***The 12th Congress of Iranian Ceramic Society***, Tehran, 30th April and 1st May 2019, Iran: Iranian Ceramic Society, (2019), 171-179. https://www.dropbox.com/s/t9tbc7hxxxdgb1f/%D9%81%D8%A7%DB%8C%D9%84%20%D9%86%D9%87%D8%A7%DB%8C%DB%8C%20%D9%85%D8%AC%D9%85%D9%88%D8%B9%D9%87%20%D9%85%D9%82%D8%A7%D9%84%D8%A7%D8%AA1.pdf?dl=0

AIMS AND SCOPE

Advanced Ceramics Progress (ACERP) as an ISC international journal is devoted to elucidating the fundamental aspects of chemistry and physics occurring at a wide range of oxide and nonoxide ceramics and composite materials and their processing, microstructure, properties, and applications. The journal provides a unique venue for publishing new exciting research, focusing on dynamic growth areas in this field.

INSTRUCTIONS FOR AUTHORS

Submission of manuscript represents that it has neither been published nor submitted for publication elsewhere and is result of research carried out by author(s).
Authors are required to include a list describing all the symbols and abbreviations in the manuscript. Use of the international system of measurement units is mandatory.

- On-line submission of manuscripts results in faster publication process and is recommended. Instructions are given in the ACERP web site: www.acerp.ir
- References should be numbered in brackets and appear in sequence through the text. List of references should be given at the end of the manuscript.
- Figures' captions are to be indicated under the illustrations. They should sufficiently explain the figures.
- Illustrations should appear in their appropriate places in the text.
- Tables and diagrams should be submitted in a form suitable for reproduction.
- Photographs and figures should be of high quality saved as jpg files (resolution > 600 dpi).
- Tables, illustrations, figures and diagrams will be normally printed in single column width (8 cm). Exceptionally large ones may be printed across two columns (17 cm).

PAGE CHARGES AND REPRINTS

ACERP subscribers do not need to make any payment for publication and reprints.

AUTHORS CHECKLIST

- Author(s), bio-data including academic degree, affiliation(s), ORCiD(s), and e-mail addresses.
- Manuscript including title, abstract, key words, illustrations, tables with tables' captions, figures with figures' captions, acknowledgement, and list of references.
- MS Word files of the manuscript in the ACERP template and all figures (resolution > 600 dpi).
- Similarity check of the manuscript, copyright forms, and conflict of interest forms

Advanced **Cer**amics **P**rogress,
P.O. Box 31787-316, Meshkin Dasht, Alborz, I. R. Iran
Materials and Energy Research Center, Imam Khomeini Blvd, Meshkin Dasht, Alborz, I. R. of Iran
P.O. Box 14155-4777, Tehran, I. R. Iran
No. 5, Ahuramazda St., Alvand Ave., Argentine Sq., Tehran, Tehran, I. R. of Iran

www.merc.ac.ir - www.icers.ir

Advanced Ceramics Progress

Volume 7, Number 2, Spring 2021

CONTENTS

Journal Home Page: www.acerp.ir